Air Force Institute of Technology
AFIT Scholar

Theses and Dissertations | Student Graduate Works

6-14-2012

Design, Fabrication and Testing of Tunable RF Meta-atoms

Derrick Langley

Follow this and additional works at: https://scholar.afit.edu/etd

Part of the Engineering Science and Materials Commons

Recommended Citation

Langley, Derrick, "Design, Fabrication and Testing of Tunable RF Meta-atoms" (2012). *Theses and Dissertations*. 1128.
https://scholar.afit.edu/etd/1128

This Dissertation is brought to you for free and open access by the Student Graduate Works at AFIT Scholar. It has been accepted for inclusion in Theses and Dissertations by an authorized administrator of AFIT Scholar. For more information, please contact richard.mansfield@afit.edu.

المنارة للاستشارات

www.manaraa.com

DESIGN, FABRICATION AND TESTING OF TUNABLE RF META-ATOMS

DISSERTATION

Derrick Langley, Captain, USAF

AFIT/DEE/ENG/12-04

DEPARTMENT OF THE AIR FORCE
AIR UNIVERSITY

AIR FORCE INSTITUTE OF TECHNOLOGY

Wright-Patterson Air Force Base, Ohio

APPROVED FOR PUBLIC RELEASE; DISTRIBUTION UNLIMITED.

المنارة للاستشارات
www.manaraa.com

The views expressed in this dissertation are those of the author and do not reflect the official policy or position of the United States Air Force, Department of Defense, or the U.S. Government. This material is declared a work of the U.S. Government and is not subject to copyright protection in the United States.

المنارة للاستشارات

www.manaraa.com

AFIT/DEE/ENG/12-04

DESIGN, FABRICATION AND TESTING OF TUNABLE RF META-ATOMS

DISSERTATION

Presented to the Faculty

Graduate School of Engineering and Management

Air Force Institute of Technology

Air University

Air Education and Training Command

In Partial Fulfillment of the Requirements for the

Degree of Doctor of Philosophy

Derrick Langley, B.S.E.E., M.S.E.E.

Captain, USAF

June 2012

APPROVED FOR PUBLIC RELEASE; DISTRIBUTION UNLIMITED.

المنارة للاستشارات

www.manaraa.com

AFIT/DEE/ENG/12-04

DESIGN, FABRICATION AND TESTING OF TUNABLE RF META-ATOMS

Derrick Langley, B.S.E.E, M.S.E.E.

Captain, USAF

Approved:

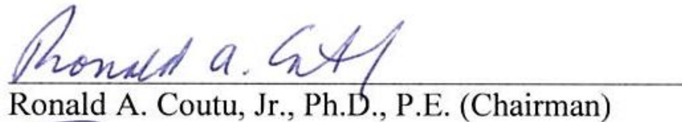

Ronald A. Coutu, Jr., Ph.D., P.E. (Chairman) — 18 May 2012 Date

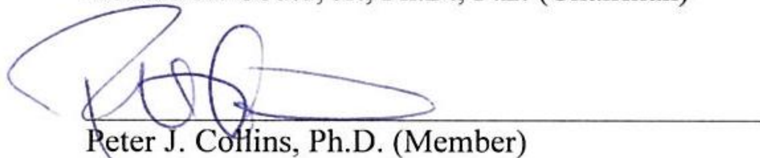

Peter J. Collins, Ph.D. (Member) — 18 MAY 2012 Date

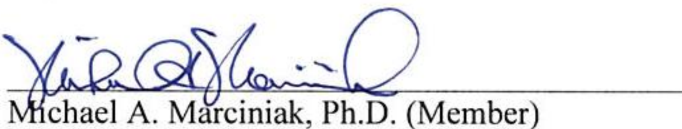

Michael A. Marciniak, Ph.D. (Member) — 18 May 12 Date

Accepted:

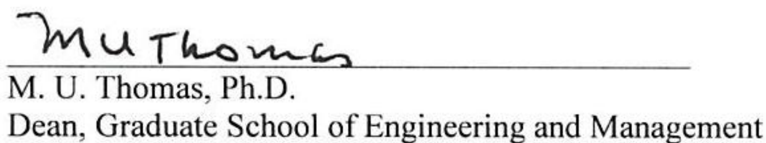

M. U. Thomas, Ph.D.
Dean, Graduate School of Engineering and Management — 1 Jun 2012 Date

للاستشارات المنارة

www.manaraa.com

AFIT/GDE/ENG/12-04

Abstract

Metamaterials are engineered structures designed to alter the propagation of electromagnetic waves incident upon the structure. The focus of this research was the effect of metamaterials on electromagnetic signals at radio frequencies. RF meta-atoms were investigated to further develop the theory, modeling, design and fabrication of metamaterials. Comparing the analytic modeling and experimental testing, the results provide a deeper understanding into metamaterials which could lead to applications for beam steering, invisibility cloaking, negative refraction, super lenses, and hyper lenses. RF meta-atoms integrated with microelectromechanical systems produce tunable meta-atoms in the 10 – 15 GHz and 1 – 4 GHz frequency ranges. RF meta-atoms with structural design changes are developed to show how inductance changes based on structural modifications. RF meta-atoms integrated with gain medium are investigated showing that loss due to material characteristics can be compensated using active elements such as a Low Noise Amplifier. Integrating the amplifier into the split ring resonator causes a deeper null at the resonant frequency.

The research results show that the resonant frequency can be tuned using microelectromechanical systems, or by induction with structural designs and reduce loss associated with the material conductivity by compensating with an active gain medium. Proposals that offer future research activities are discussed for inductance and active element meta-atoms. In addition, terahertz (THz), infrared (IR), and optical structures are briefly investigated.

www.manaraa.com

Acknowledgements

First, I must thank my wife and kids for their prayers and support during this endeavor. They were like a lighthouse beacon's light in the dark showing and providing me support during these three years. Dr. Ronald A. Coutu Jr., you have been a wonderful advisor who helped me stay focused while on the long path to completion. I must also extend a debt of gratitude to my committee members, Dr. Peter J. Collins and Dr. Michael A. Marciniak, whose mentoring advice, and keen insights were integral to the success of this research.

Special thanks to the Air Force Research Laboratory (AFRL), Materials and Manufacturing Directorate, Wright-Patterson AFB, Ohio for the financial support provided for this research. An additional thank you goes to the AFRL Sensors Directorate, Components Division, Devices for Sensing Branch who allowed me to spend lots of time utilizing their clean room facility to construct my research components. It was great to use the facility for building components and asking questions on problem areas. And Drs. Elizabeth A. Moore and Versalle "Verb" F. Washington, thanks for the editorial comments on my dissertation.

To my friends in the PhD-11 class, I could not have asked for any better classmates. You all made the stress level so low with our various family outings, soccer games, and overall wonderful camaraderie.

Derrick Langley

المنارة للاستشارات
www.manaraa.com

Table of Contents

Page

Abstract iv

Acknowledgements v

Table of Contents vi

List of Figures x

List of Tables xvi

List of Symbols xvii

List of Abbreviations xxii

I. Introduction 1

1.1. Long Term Problem 4
1.2. Contributions 5
1.3. Publications 6
1.4. Dissertation Organization 8

II. Background 10

2.1. Metamaterials 10
2.1.1. Metamaterials Effective Parameters 10
2.1.2. Meta-atom Equivalent Circuit Modeling 17
2.1.2.1. Lumped Elements 18
2.1.2.2. Equivalent Circuit Modeling 25
2.1.3. Retrieval Process for Effective Parameters 28
2.1.4. Compensating for loss at resonant frequency 30
2.2. Microelectromechanical Systems 30
2.2.1 MEMS Fabrication 31

www.manaraa.com

Page

2.2.1.1. Bulk Micromachining 32
2.2.1.2. Micromolding 33
2.2.1.3. Surface Micromachining (polyMUMPS ®, SUMMIT V ™) 34
2.2.1.4. MEMS Fabrication Method for Meta-atoms 37
2.2.2. Actuation Methods 37
2.2.3. Electrostatic Actuation 39
2.2.3.1. Fringe effect on cantilevers 44
2.2.3.2. Dielectric effect on cantilevers 44
2.2.3.3. Cantilever thickness variation 45
2.2.3.4. Anchor Moment 45
2.3. Summary 46

III. RF Metamaterial Structures 47

3.1. Fixed Meta-atoms for Metamaterial Structures 47
3.2. Capacitive Tunable Meta-atoms 49
3.2.1. 10 – 15 GHz Gap capacitive tuning meta-atom design 49
3.2.2. 1 – 4 GHz Gap based design 52
3.2.3. 1 – 4 GHz Intra-ring Meta-atom Designs 53
3.3. 1 – 4 GHz Inductance based Meta-atom Designs 55
3.4. 1 – 4 GHz Active Element based Meta-atom Design 57
3.5. Summary 59

IV. RF Meta-atom Modeling and Simulation 60

4.1. Analytical Modeling 60
4.1.1. Meta-atom Analytical Modeling 60
4.1.2. Cantilever Analytical Modeling 64
4.2. Meta-atom Equivalent Circuit Modeling 66
4.3. RF Simulations 68
4.3.1. CoventorWare ® Modeling 68
4.3.1.1. 10 – 15 GHz Gap based Designs 70
4.3.1.2. 1 – 4 GHz Gap based Designs 71
4.3.1.3. 1 – 4 GHz Intra-Ring Designs 74
4.3.1.4. 1 – 4 GHz Inductance based Meta-atom Designs 75

المنارة للاستشارات
www.manaraa.com

Page

4.3.2. CST Microwave Studio ® Modeling ... 78
4.3.2.1. 10 – 15 GHz Gap based Designs ... 78
4.3.2.2. 1 – 4 GHz Gap based Designs ... 80
4.3.2.3. 1 – 4 GHz Intra-ring Meta-atom Designs ... 81
4.3.2.4. 1 – 4 GHz Inductance based Meta-atom Design ... 82
4.3 Summary ... 83

V. RF Metamaterial Experimental Results ... 84

5.1. Fixed Meta-atoms ... 85
5.2. Capacitive Tunable Meta-atoms ... 87
5.2.1. 10 – 15 GHz Gap based Meta-atom Designs ... 88
5.2.2. 1 – 4 GHz Gap based Meta-atom Designs ... 92
5.2.3. 1 – 4 GHz Intra-ring Meta-atom Design ... 93
5.3. 1 – 4 GHz Inductance based Meta-atom Designs ... 95
5.3.1. Static Designs ... 95
5.4. 1 – 4 GHz Active Element based Meta-atom Design ... 100
5.5. Summary ... 102

VI. Conclusion ... 104

6.1 Research and Contributions Summary ... 104
6.2 Recommendations for Future Research ... 106
6.2.1. Tunable Inductance Meta-atom Design ... 106
6.2.2. Meta-atoms combined into Metamaterials for 2-D Focus Beam System ... 106
6.2.3. Future Work Summary ... 109

Appendix A. Process Followers ... 110

Appendix B. Matlab Files ... 119

Appendix C. Investigation of Terahertz Metamaterials ... 130

Appendix C.1. PolyMUMPS ® Terahertz Metamaterial Structure Background ... 130
Appendix C.2. Simulation for polyMUMPS ® Terahertz Metamaterial Structures ... 135
Appendix C.3. Testing for polyMUMPS ® Terahertz Metamaterial Structures ... 137

المنارة للاستشارات
www.manaraa.com

Page

Appendix D. Investigation into Optical Metamaterials 141

Appendix D.1. Optical Metamaterial Structures Background 141
Appendix D.2. Simulation for Optical Metamaterial 146
Appendix D.3. Testing for Optical Metamaterial 146

Appendix E. IR Meta-atom Incorporated with a Thin-Film Transistor 151

Appendix E.1 IR Metamaterial Structure Background 151
Appendix E.2. Analytical Approach to IR Meta-atom 153
Appendix E.3. IR Application 156
Appendix E.4. IR Meta-atom Structure at 60 THz 158

Bibliography 165

Vita 173

المنارة للاستشارات
www.manaraa.com

List of Figures

Figure Page

1. Optical microscope picture of (a) electric split-ring resonator and (b) meanderline waveplate used to generate circular polarization at IR frequencies [6]. 2

2. 2D microwave cloaking structure (background image) with a plot of the material parameters that are implemented. μ_r (red line) is multiplied by a factor of 10 for clarity. μ_θ (green line) has the constant value 1. ε_z (blue line has the constant value 3.423. The SRRs of cylinder 1 (inner) and cylinder 10 (outer) are shown in expanded schematic form (transparent square insets) [10]. 5

3. RF Strip Line used for electromagnetic plane wave propagation. 14

4. Split Ring Resonators 16

5. Periodic thin wire mesh 17

6. (a) Simple loop showing the voltage applied and the direction of the current flow. (b) sub-conductors (*a*) in a thin conductor (*k*) with cross-sectional area indicating the number of filaments in the wire. 19

7. Parallel Plate Capacitor 21

8. Capacitor model showing the fringing effect. 23

9. 1 – 4 GHz meta-atom transmission response with resonance at 2.83 GHz. 25

10. Series Resonant Bandstop Filter Equivalent Circuit 26

11. PolyMUMPS ® layers and dimensions for MEMS. The layers provide structures to build devices with a surface micromachine process. 35

12. SUMMiT IV & V™ fabrication layers. The polysilicon layers are the structural mechanical layers. 36

13. MEMS electro-thermal technique illustrating beam elongation due to Joule heating caused by current flow through the conductor material 38

14. Parallel plate capacitor used to describe electrostatic actuation. 40

15. Cantilever 43

16. Simple cantilever beam with actuation pad covered with a thin dielectric layer for short circuit protection. 44

المنارة للاستشارات
www.manaraa.com

Figure Page

17. Cantilever anchor deflecting due to an applied force 46

18. Advances in metamaterials. The solid symbols denote $n < 0$; the open symbols denote $\mu < 0$. Orange: data from structures based on the double split-ring resonator (SRR); green: data from U-shaped SRRs; blue data from pairs of metallic nanorods; red: data from the fishnet structure. The four insets give pictures of fabricated structures in different frequency regions [56]. 47

19. (a) Diagram of the baseline SRR with additional rods. (b) RF Transmission measurement showing resonance at 2.8 GHz with SRR inserted in RF strip-line. 49

20. SRR unit cell schematic showing modifications to the gap region to accommodate the cantilever array.. 50

21. Layout showing cantilevers in the 10 – 15 GHz meta-atom design [57]................... 52

22. Layout for the 1 – 4 GHz Gap based meta-atom design... 53

23. Layout of the three intra-ring meta-atom design variations integrated with (Design 1) cantilevers between rings, (Design 2) cantilevers in the gap and connecting the rings, and (Design 3) cantilevers with varying widths between the rings. 55

24. Layouts of the meta-atoms (a) baseline, (b) Loop A with loop extending up and down the outer SRR's vertical side and (c) Loop B with the loop equal to the outer SRR's vertical side. 56

25. Active element integrated into the 1 – 4 GHz meta-atom. The GaAs low noise amplifier integrated into the baseline meta-atom is used to effect the resonant frequency based on a gain medium inserted into the SRR. 59

26. Meta-atom showing dimensions used to calculate the capacitance and inductance values. 60

27. The 1 – 4 GHz Meta-atom showing sections for capacitance calculations. 61

28. Cantilever deflection force versus cantilever thickness.. 64

29. Cantilever pull-in voltage as a function of length and capacitance model. The fringing effect on the capacitance model shows the largest deviation from the simple model. The simple model and model with the dielectric layer show a similar pattern........... 65

30. Meta-atom equivalent circuit model. 67

31. Meta-atom equivalent circuit frequency response 68

32. Cantilever actuation simulated with CoventorWare ® to determine the biasing voltage necessary to draw the cantilevers to the actuation pads.. 70

المنارة للاستشارات
www.manaraa.com

Figure Page

33. Meshedcantilever in CoventorWare ® used to calculate pull-in voltage, capacitance and release voltage [57]. 71

34. 1 – 4 GHz Baseline meta-atom design with dimensions used in analytical modeling and CoventorWare ® simulations. 72

35. Baseline meta-atom meshed and prepared for CoventorWare ® simulations. 73

36. Meta-atom design modified with cantilevers for a tunable resonant frequency response. 74

37. CoventorWare ® plots showing magnitude of imaginary current density incident on the (a) Baseline, (b) Loop A and (c) Loop B versions of the meta-atom designs. Changes in the imaginary current density were observed as the length of each loop increased from the Baseline to the Loop B design. The magnitude of the imaginary current density increases on the inner split ring resonator which is relative to the increase in inductance and capacitance. However, the magnitude of the imaginary current density decreases for the outer split ring resonator. 77

38. CST Microwave Studio ® model of the Baseline meta-atom designed with lumped element capacitors. Periodic boundary conditions are used in the xy-plane. [67]...... 79

39. S-parameter results from the single cell periodic model with fixed gap capacitance. (a) The magnitudes of S_{11} and S_{21} show resonance points near 11, 20 and 23 GHz. (b) The phases of S_{11} and S_{21} show the largest changes around the resonance points [67]. 80

40. 1 – 4 GHz meta-atom integrated with cantilevers. The cantilevers are simulated with lumped elements capacitors. 81

41. Intra-ring Meta-atom designs simulated in CST Microwave Studio®. The transmission response for each design show the resonant frequency shifts to lower frequency as the capacitance increases. 82

42. CST Microwave Studio ® simulation results for the Loop B Inductance Meta-atom design. The resonant frequency shifted to 2.5 GHz based on the added loop on the outer split ring resonator. 83

43. The Agilent E8362B Programmable Network Analyzer connected to 4 GHz strip-line and 10 GHz strip-line. 84

44. 4 GHz RF strip-line with 1 – 4 GHz Baseline meta-atom designs inserted for testing 85

45. Transmission response captured for the 1 – 4 GHz Baseline meta-atom. The transmission magnitude approaches zero at 2.83 GHz. 86

المنارة للاستشارات
www.manaraa.com

Figure Page

46. The transmission magnitude response captured for the 10 – 15 GHz Baseline meta-atom showing the resonant frequency occurring just above 10 GHz. The inset shows a 10 – 15 GHz Baseline meta-atom inserted in the RF strip-line between the inner and outer conductor. 87

47. A 10 – 15 GHz Capacitive tunable meta-atom fabricated on quartz substrate. The meta-atom had to be cut at the metal trace leading to the cantilever actuation pads for the inner split ring resonator. Two types of cuts were created with a focused ion beam to isolate the split ring resonator which led to two testing methods. 89

48. Cantilevers pulled-in at 60 VDC. Image captured during DC testing on meta-atom array. All the cantilevers are pulled-in which represents the maximum capacitance value achieved. 90

49. Transmission from a 1 × 17 array of the 10 – 15 GHz Capacitive Meta-atom with cut across the outer split ring resonator. As the applied voltage is increased the resonant frequency shifts from 14.2 GHz to 12.6 GHz. 91

50. Transmission from a 1 × 17 array the 10 – 15 GHz Capacitive Meta-atom with cut across the metal trace. As the applied voltage is increased the resonant frequency shifts from 8.4 GHz to 8.04 GHz. 92

51. Experimental setup showing 4 unit cells of the 1 – 4 GHz meta-atom embedded with cantilever in the gap and placed in the RF strip-line. The image shows the DC wires bonded to the actuation pads to control the electrostatic actuation. The array is suspended between the inner conductor and outer conductor by styrofoam to help with electrical isolation. 93

52. Plot of the transmission response for the meta-atom design with cantilevers embedded in the split ring resonator's gap. The initial resonant frequency occurs at 2.06 GHz as predicted by the simulation; however, the change in resonance shifts by 0.18 GHz. 93

53. Transmission responses for the Baseline and three modified meta-atom designs in the initial and final operational states. 95

54. Meta-atoms inserted in the RF strip-line between the center and outer conductor. The signals propagating down the strip-line generate planar electric and magnetic wave from the center to the outer conductor. 96

55. Fabricated Inductance based meta-atom designs: a) prototypes on printed circuit board and b) designs made by microelectronic fabrication techniques on quartz substrates. The FR4 PCB samples have rough edges which is a result from the milling process. The microelectronic fabrication improved the edges on the samples. 97

المنارة للاستشارات
www.manaraa.com

Figure Page

56. a) Data collected on meta-atoms fabricated on FR4 printed circuit board. b) Data collected on meta-atoms fabricated on quartz substrates. The samples are measured in a 4 GHz strip-line to obtain the small signal S-parameters. 99

57. The effective refractive index (*n*) for each design calculated from transmission data collected between 1.5 – 3.5 GHz. 100

58. 1 – 4 GHz meta-atoms integrated with LNAs placed in 4 GHz RF strip-line. 101

59. a) Transmission response for the meta-atoms in the RF strip-line. The Baseline, Baseline with a 0.4 mm gap in the outer split ring resonator and meta-atom integrated with the low noise amplifier were tested using a programmable network analyzer. The data is collected over 10 MHz to 4 GHz. In the plot, the frequency range is 10 MHz to 4.2 GHz to show the location of the resonant frequency. Samples are taken at biasing steps from 0 to 7 VDC at one volt intervals. The transmission response plots show the resonant response at 0 and 7 VDC. 102

60. Schematic of a focused beam system [71]. 107

61. 6 – 8 GHz Meta-atom for testing in the 2-D Focused Beam System. Based on modeling and simulation, the meta-atom will resonate at 7 GHz. 108

62. A schematic of a top down view of a single unit SRR with the dimensions indicated. 132

63. 3D Diagram of a unit cell of the patterned metamaterial shows the three polysilicon and two silicon dioxide alternating layers grown on a silicon wafer with a thin silicon nitride buffer layer. 133

64. A schematic illustrating the layers and their corresponding dimensions used in the polyMUMPS ® process. 135

65. Charge density simulated on the THz SRR which is used to calculate the capacitance of the conductors with respect to the other conductors. 136

66. The imaginary current density magnitude simulated for the SRRs of the metamaterial structure. 137

67. THz Metamaterial structures shown in an SEM image to show quality of SRRs and surrounding surface area. This image is a 0.06 mm^2 area taken out of a 1 cm^2 area. 138

68. Layers of the polyMUMPS ® structures etched out using a focused ion beam to inspect the Polysilicon and silicon dioxide layers. 138

69. Transmission spectra of the polyMUMPS ® material without the SRRs showing zero transmission across the measured frequency range. 140

للاستشارات المنارة

www.manaraa.com

Figure Page

70. Transmission spectra of the polyMUMPS ® samples fabricated with SRRs showing a transmission of about 25% and a resonance at 3.7 and 18.4 THz 140

71. Optical Metamaterial Designs.. 141

72. Metamaterial etching results 145

73. SEM image of optical fishnet structure 146

74. Optical metamaterial fishnet pattern generated by E-beam lithograpy 147

75. Interferometric Lithography sample completed at the University of Dayton. 148

76. Interferometric Samples generated at Air Force Research Laboratory. 149

77. AFIT's complete angle scatter instrument used to measure bi-directional reflection distribution function for optical metamaterials. 150

78. Bi-directional reflectance distribution function measurements for the optical metamaterial fishnet. Results show the structure is a diffraction grating at optical frequencies. 150

79. Cartoon showing the effect of negative refractive index. 153

80. SeeSPOT III+ Imager uses IR to detect object at night [95]. 157

81. IR Images obtained with the SeeSPOT III+ Imager. 157

82. Free-space wavelength as a function of permittivity, width, gap and length. 159

83. Effective permeability as a function of frequency. 160

84. Index of refraction calculated using the effective permittivity and permeability. 161

85. Thin film transistor integrated into SRR meta-atom.. 162

86. Images showing charge density of the gate when the doped ZnO act as a metal. 163

87. Charge density simulated on thin film transistor. The SRRs are removed to show the charge density region. 164

www.manaraa.com

List of Tables

Table Page

1. PolyMUMPS ® Run #83 material information 35

2. Simulated capacitance and induction parameters for the designs at initial operational state where the capacitance gap is 2 μm and no actuation voltage applied; along with the calculated resonant frequency for each design. 75

3. Simulated capacitance and induction parameters for the designs at final operational state where the capacitance gap is closed and maximum actuation voltage applied; along with the calculated resonant frequency for each design. 75

4. Inductance and capacitance values obtained during modeling and simulations......... 77

5. Advantages and disadvantages of IR wireless communication. 151

المنارة للاستشارات

www.manaraa.com

List of Symbols

Symbol		Page
n	Refractive Index	2
VO_2	Vanadium Dioxide	2
λ	Wavelength	3
ω	Radian Frequency	3
c	Speed of Light	3
i	Imaginary	3
k_x	Wave Vector	3
k_z	Wave Vector	3
nm	Nanometer	3
x	X-axis	3
z	Z-axis	3
ε_z	Permittivity Tensor	5
μ_θ	Permeability Tensor	5
μ_r	Permeability Tensor	5
ε	Permittivity	10
μ	Permeability	10
k_i	Wave Vector	11
k_j	Wave Vector	11
θ_ε	Permittivity Phase	11
θ_μ	Permeability Phase	11
ε'	Real Permittivity	12
ε''	Imaginary Permittivity	12
μ'	Real Permeability	12
μ''	Imaginary Permeability	12
π	Pi	12
e	Exponential	12

المنارة للاستشارات

www.manaraa.com

Symbol		Page
ρ	Material Resistivity	15
ω_0	Resonant Frequency	15
Γ	Damping Factor	15
a	Periodic Spacing	15
f	Fill Factor	15
r	Radius	15
γ	Damping Factor	16
ω_p	Plasma Frequency	16
m_{eff}	Effective Mass	16
q	Electron Charge	16
N	Electron Concentration	16
μ_0	Permeability Constant	18
l	Length	18
t	Thickness	18
w	Width	18
C	Capacitance	18
L	Inductance	18
Ψ_{ij}	Magnetic Flux	19
a	Sub-conductor Cross Section	19
k	Conductor	19
ln	Natural Logarithm	19
u	Length to Width Ratio	19
I_j	Current in Loop j	19
$L_{P_{ii}}$	Self-inductance	19
cof	Cofactor	20
det	Determinant	20
s	Sign ±	20
I	Current	20

المنارة للاستشارات
www.manaraa.com

Symbol		Page
V	Voltage	20
ε_0	Permittivity Constant	22
ε_r	Relative Permittivity	22
d	Distance	22
$Area$	Surface Area	22
ε_{air}	Relative Permittivity of Air	23
$\varepsilon_{Si_3N_4}$	Relative Permittivity of Silicon Nitride	23
$C_{combined}$	Combined Capacitance	23
C_{air}	Capacitance of Air	23
$C_{dielectric}$	Capacitance of Dielectric	23
z	Impedance	28
$\mathbf{E}_{inc}$	Incident Electric Field	28
$\mathbf{E}_{refl}$	Reflected Electric Field	28
$\mathbf{E}_{trans}$	Transmitted Electric Field	28
S_{11}	Input Reflection Scattering Parameter	28
S_{12}	Reverse Transmission Scattering Parameter	28
S_{21}	Forward Transmission Scattering Parameter	28
m	Integer	29
Å	Angstrom	35
cm	Centimeter	35
mm	Millimeter	35
sq	Square	35
MPA	One Million Pascals	35
R	Resistance	35
T	Tensile Stress	35
α_L	Coefficient of Linear Thermal Expansion	38
L_0	Initial Beam Length	38
L_{new}	Beam Length	38

المنارة للاستشارات
www.manaraa.com

Symbol		Page
T_0	Initial Beam Temperature	38
T_{avg}	Average Final Beam Temperature	38
$E_{e,m}$	Electrostatic Potential Energy	40
F	Force	40
F_x	Force	40
V_b	Electrical Breakdown Voltage	40
k_m	Mechanical Spring Constant	41
x_0	X-axis Initial Position	41
$F_{electrical}$	Electrostatic Force	41
$F_{mechanical}$	Mechanical Restoring Force	41
E	Young's Modulus	42
V_{pi}	Pull-in Voltage	42
Si_3N_4	Silicon Nitride	44
µm	Micrometer	49
pF	Picofarad	50
pHEMT	Pseudomorphic High Electron Mobility Transistor	57
GaAs	Gallium Arsenide	57
dB	Decibel	58
g_0	Initial Gap	61
nH	Nanohenry	63
C_0	Initial Capacitance	66
ω_{res}	Resonant Frequency	75
L_{Inner}	Inner Ring Self-inductance	75
L_{Outer}	Outer Ring Self-inductance	75
Au	Gold	96
Ti	Titanium	96
pC	Picocoulombs	135
Cr	Chromium	135

المنارة للاستشارات
www.manaraa.com

Symbol		Page
pH	Picohenry	136
Ag	Silver	143
Al_2O_3	Alumina	143
Ga-ZnO	Gallium doped Zinc Oxide	143
λ_{LC}	Free-space Wavelength	155
ω_{LC}	Resonant Frequency	155
μ_{eff}	Effective Permeability	160

المنارة للاستشارات

www.manaraa.com

List of Abbreviations

Abbreviation		Page
AFRL	Air Force Research Laboratory	v
CASI	Complete Angle Scatter Instrument	149
CD	Compact Disc	151
DXRL	Deep X-ray Lithography	33
EM	Electro-magnetic	1
ETS	Enhanced Targeting Sight	157
FR4	Insulating Glass Reinforced Epoxy Resin	58
FTS	Fourier Transform Spectroscopy	137
GB	Gigabits	78
GHz	Gigahertz	4
ICP	Inductively Coupled Plasma	144
IR	Infrared	iv
LIGA	Deep X-ray Lithography, Electroplating (Galvanoformung in German) and Injection Molding (Abformung in German)	32
LNA	Low Noise Amplifier	57
LOREIab	Low Observable Radar and Electromagnetic Laboratory	84
LOREnet	Low Observable Radar and Electromagnetic Network	78
MHz	Megahertz	75
MIT	Metal-insulator Transition	106
MMIC	Monolithic Microwave Integrated Circuit	57
MOSFET	Metal-Oxide-Semiconductor Field Effect Transistor	161
PCB	Printed Circuit Board	58
PECVD	Plasma Enhanced Chemical Vapor Deposition	51
PLD	Pulsed Laser Deposition	144
PNA	Programmable Network Analyzer	84
polyMUMPS®	Polysilicon Multi-User MEMS Processes	34
PSG	Phosphosilicate Glass	34

للاستشارات المنارة
www.manaraa.com

Abbreviation		Page
SEM	Society for Experimental Mechanics	8
SEM	Scanning Electron Microscope	138
S-Band	S-Band Radio Frequencies (2 – 4 GHz)	57
S-Parameters	Scattering Parameters	28
SPIE	Society of Photo-Optical Instrumentation Engineers	7
SRR	Split Ring Resonator	2
SUMMiT ™	Sandia Ultra-planar, Multi-level MEMS Technology	34
TEM	Transverse Electro-Magnetic	80
TFT	Thin Film Transistor	161
THz	Terahertz	iv
TV	Television	151
2-D	Two Dimensional	59
VCR	Video Cassette Recorder	151

المنارة للاستشارات

www.manaraa.com

DESIGN, FABRICATION AND TESTING OF TUNABLE RF META-ATOMS

I. Introduction

Metamaterials are a new concept based on periodic meta-atom structures used to control electro-magnetic (EM) propagation by producing materials with a tailored index of refraction. Research into metamaterial structures began in 1968 when V. G. Veselago published an article outlining the approach and application of metamaterial structures [1]. In the years since, as modeling and fabrication techniques matured, researchers were able to design and create structures that have an effective electric permittivity and effective magnetic permeability. The initial concepts opened up a new field of study into the investigation of the electric and magnetic properties of metamaterials. Previous research efforts focused on modeling, designing, fabrication for radio frequency (RF), infrared (IR) and optical metamaterials which will be discussed in this introduction. This research effort focuses on modeling, designing, fabrication and testing of tunable metamaterials operating at RF frequencies and implementing a gain medium to compensate for loss. Terahertz, infrared and optical metamaterials were briefly investigated and appear in the appendix.

Metamaterial structures affect the propagation of electromagnetic waves based on the size, dimension, periodicity and material properties of the structures. Investigation into RF metamaterial began in 1996 when Pendry *et al*. first theoretically suggested (and later experimentally demonstrated) that a composite medium of periodically placed thin metallic wires can behave as an effective plasma medium of radiation with wavelength much larger than the spatial periodicity of the structure [2]. A year later, they discovered

المنارة للاستشارات
www.manaraa.com

a split ring resonator (SRR) produces the changes in the refractive index (*n*) and effectively changes the EM propagation [3]. His work in RF signal propagation has been applied to other areas of the EM spectrum.

IR metamaterial has the potential to revolutionize the research into IR applications by improving signal propagation and enhancing sensing capabilities. In the IR region, metamaterial structures are still of considerable size and dimension, which enables the use of microelectronic fabrication techniques. Some current research into metamaterial designs for IR frequencies include: 1) dynamic tuning of an infrared hybrid-metamaterial resonance using a sapphire substrate, thin layer of vanadium dioxide (VO_2) and thick gold SRRs [4], 2) an optical band-pass filter based on a double lattice SRR array [5].

A final example for an IR application is a comparison of birefringent electric split-ring resonator and meanderline structures as quarter-wave plates at terahertz frequencies [6]. Strikwerda *et al*. fabricated a quarter-wave plate from a single layer of birefringent electric split-ring resonators and compared the transmission and reflection IR signals to a scaled double layer meanderline structure. Figure 1 shows the structures used in the comparison of the designs to generate circular polarization.

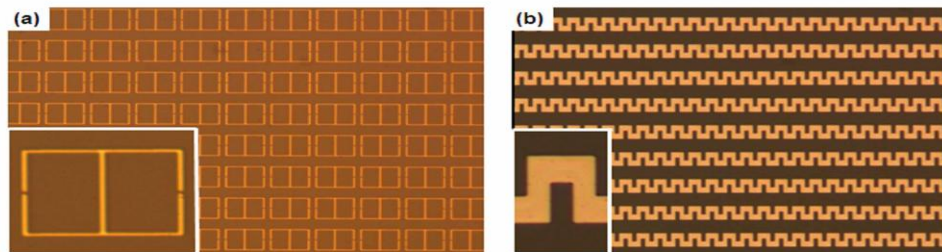

Figure 1. Optical microscope picture of (a) electric split-ring resonator and (b) meanderline waveplate used to generate circular polarization at IR frequencies [6].

المنارة للاستشارات
www.manaraa.com

Optical metamaterials generate a different set of challenges compared to RF and IR metamaterials due to the decrease in wavelength (λ). The most difficult challenge is scaling the dimension of the elements to be less than $\lambda/5$ size to avoid undesired interaction between the EM radiation and the elements. Chettiar *et al*. investigated metamaterials at optical frequencies and outlined fabrication challenges and the impact of fabrication limitations, specifically surface roughness, of the fabricated structures on the optical properties of the metamaterials [7]. One of the main goals of the investigation was to produce negative index material behavior for red light at a wavelength of 710 nm. By incorporating silver and alumina layers into a fishnet structure, made by a tailored evaporation process, Chettiar *et al*. demonstrated a single negative-negative index material property that was supported by their simulations.

Another challenge at optical frequencies is overcoming the diffraction limit, or the problem of decreasing evanescent modes [8]. Pendry *et al*. show that material with a negative index of refraction (n) can successfully spread waves, such that the component k_z of the wave vector along the direction of spreading has an imaginary value [9].

$$k_z = i\sqrt{\frac{\omega^2}{c^2} - k_x^2} \tag{1}$$

Where ω is the radian frequency, c is the speed of light in a vacuum, k_x and k_z is the wave vector components along the x and z axis, respectively. This model is valid for very large k_x, or in other words, for very short electromagnetic waves. In materials with positive values of n, where $n = kc/\omega$, the amplitude of such waves (the evanescent modes), in accordance with Equation (1), will exponentially decrease along the z axis, thereby making it impossible for an optical system to image objects with sizes noticeably smaller

المنارة للاستشارات
www.manaraa.com

than the wavelength [8]. However, in work [9] Pendry suggests that in material with negative refraction index, waves with large values of k_x do not decrease, but increase thus suggesting that it is possible to transfer images with sizes much less than the wavelength from one point of space to another [8], [9]. This suggestion was motivated by the possibility of increasing surface modes due to resonance in material with negative refraction [8].

1.1. Long Term Problem

Baseline meta-atom designs are static structures that cannot be used in tuning applications. The static structures are suitable for fixed frequency operations, but having a tunable meta-atom increases the functionality for broader applications. For example, a cloaking device devised by Schuring *et al.* is able to block an obstacle by surrounding it with artificially structured metamaterials designed for operation over a narrow band of microwave frequencies. The cloak decreased scattering from the hidden object while at the same time reducing its shadow, so that the cloak and object combined began to resemble empty space [10]. Figure 2 shows the cloaking device designed by Schuring *et al*. which is composed of copper split ring resonators on Duroid 5870 material. A limitation of this cloaking implementation is that it has a fixed resonant frequency at 8.5 Gigahertz (GHz). To implement a tunable metamaterial structure, more research is required into the modeling, design, fabrication and testing for meta-atoms that can shift the resonant frequency based on changing structural dimensions or material properties. My research focuses on the individual meta-atom to determine methods to tune the

المنارة للاستشارات
www.manaraa.com

resonant frequency. In addition, loss associated with metamaterial designs will be investigated.

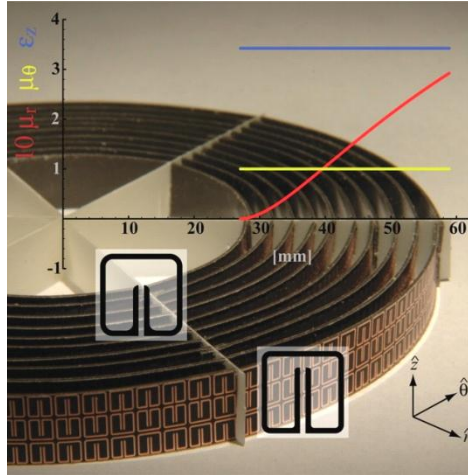

Figure 2. 2D microwave cloaking structure (background image) with a plot of the material parameters that are implemented. μ_r (red line) is multiplied by a factor of 10 for clarity. μ_θ (green line) has the constant value 1. ε_z (blue line has the constant value 3.423. The SRRs of cylinder 1 (inner) and cylinder 10 (outer) are shown in expanded schematic form (transparent square insets) [10].

1.2. Contributions

The novel contributions of this work, to the metamaterial field, include:

1. Demonstrate tunable meta-atoms based on shifting capacitance with electrostatically actuated MEMS varactors. By integrating these tunable capacitive elements into the double split ring resonator baseline meta-atom, I developed a method to tune the meta-atom based on how the electrostatic MEMS varactors adjust the overall capacitance. Also, integrating the baseline meta-atom with the electrostatic MEMS varactors at different locations on the double split ring resonators provides design, modeling and experimental verification into the effect tunable capacitive elements have on the design's response to electromagnetic fields.

المنارة للاستشارات
www.manaraa.com

2. Produced novel 1 – 4 GHz meta-atoms that shift the resonant frequency location based structural design changes. Provides a contribution to the field using these 1 – 4 GHz meta-atoms which shift the resonant frequency based on the changes in the self-inductance value of the outer split ring resonator. Developed modeling and testing methods to understand the role self-inductance has on the resonant frequency location for meta-atoms. Fabricated and experimentally verified the designs which are in agreement with the modeling and simulations results.
3. Designed, fabricated and tested a 1 – 4 GHz active element meta-atom which compensates for losses at the individual meta-atom. This is accomplished by integrating the baseline meta-atom with a low noise amplifier which provides impedance matching and gain. Through experimental testing, I have shown that the 1 – 4 GHz active element meta-atom produces a deeper null at the resonant frequency that is often reduced in a meta-atom due to loss. Furthermore, the resonant null depth is controllable based on the biasing level applied to the low noise amplifier.

1.3. Publications

The following papers were published/ submitted during the course of this dissertations research:

Journal Articles:

1. Moore, E. A., D. Langley, M. E. Jussaume, L. A. Rederus, C. A. Lundell, R. A. Coutu, Jr., P. J. Collins and L. A. Starman. "SRRs Embedded with MEMS

المنارة للاستشارات
www.manaraa.com

Cantilevers to Enable Electrostatic Tuning of the Resonant Frequency," *Experimental Mechanics*, DOI: 10.1007/s11340-011-9498-8: 1-9 (April 2011). [58]

2. Coutu, Jr., R. A., P. J. Collins, E. A. Moore, D. Langley, M. E. Jussaume and L. A. Starman. "Electrostatically tunable meta-atoms integrated with in-situ fabricated MEMS cantilever beam arrays," *IEEE/ASME Journal of Microelectromechanical Systems*, 99: 1-6 (October 2011). [59]

3. Langley, D., R. A. Coutu, Jr. and P. J. Collins. "Investigation of between the ring capacitance shifts on meta-atom resonant frequency" (Sensors and Actuators A: Physical, Submitted November 2011)
4. Deibel, J. A., R. A. Coutu, Jr., S. Ganti, H. R. Jones and D. Langley. "Three dimensional terahertz frequency metamaterial device fabricated with MEMS processing techniques" (Optical Engineering, Submitted December 2011)
5. Langley, D., R. A. Coutu, Jr. and P. J. Collins. "Low-loss meta-atom for improved resonance response" (AIP Advances, Accepted for publication March 2012)
6. Langley, D., R. A. Coutu, Jr. and P. J. Collins. "The effects of inductance on meta-atom frequency response," (Nano-Micro Letters, Submitted March 2012)

Conference Papers:

1. Langley, D., R. A. Coutu, Jr., L. A. Starman and S. Rogers. "Optical metamaterials for photonic applications," *Proceedings of SPIE*, 7468: 74680H (August 2009). [83]
2. Langley, D., R. A. Coutu, Jr. L. A. Starman, P. J. Collins. "Fabrication Capabilities," *AFRL Metamaterials Workshop*, (October 2009)

المنارة للاستشارات
www.manaraa.com

3. Langley, D., R. A. Coutu, Jr. L. A. Starman, and M. A. Marciniak. "Investigation into metamaterial structures operating at terahertz wavelength," *Proceedings of SPIE*, 7592: 75920X (January 2010) [72]
4. Langley, D., R. A. Coutu, Jr. L. A. Starman, P. J. Collins. "MEMS integrated metamaterial structure having variable resonance for RF applications" *Proceedings of the 2010 SEM Annual Conference and Exposition on Experimental and Applied Mechanics*, 313: 1-6 (June 2010). [60]
5. Moore, E. A., D. Langley and R. A. Coutu, Jr. "Terahertz metamaterial structures fabricated by polyMUMPS," *Proceedings of the 2011 SEM Annual Conference and Exposition on Experimental and Applied Mechanics*, 284: 1-6 (June 2011). [73]
6. Langley, D., E. A. Moore, R. A. Coutu, Jr., P. J. Collins. "MEMS integrated metamaterials with variable resonance operating at RF frequencies," *Proceedings of the 2011 SEM Annual Conference and Exposition on Experimental and Applied Mechanics*, 328: 1-8 (June 2011). [61]

1.4. Dissertation Organization

This dissertation is organized as follows. Chapter I, the introduction, gives a general overview of the metamaterials field. Background information on metamaterial theory, design parameters and lumped circuit elements along with MEMS fabrication and actuation methods are covered in Chapter II. Chapter III examines RF metamaterial designs based on individual meta-atoms and how variations in the meta-atom design create engineered magnetic and electric responses. Chapter IV provides analytic modeling, finite element modeling and electromagnetic propagation simulation results

المنارة للاستشارات
www.manaraa.com

that were generated based on the meta-atom designs detailed in Chapter III. Chapter V provides the experimental results resulting from each meta-atom design. Chapter VI concludes the main document by providing an overall summary of research activities, a summary of key findings, and recommendations for subsequent research. This is followed by an appendix that provides a design toolbox consisting of fabrication process followers and developmental MATLAB® code used to support the research. Optical, terahertz and infrared metamaterials are covered in the appendix, as additional research conducted during this period. Finally, the appendix includes an example illustrating a design based on a infrared meta-atom incorporated with thin film transistor.

المنارة للاستشارات
www.manaraa.com

II. Background

2.1. Metamaterials

Metamaterials are structures composed of engineered materials [11]. These man-made structures are arranged in many different shapes based on the way the structures interact with propagating electromagnetic waves. At RF, the most abundant metamaterials consists of meta-atoms composed with split-ring resonators, and metal rods/traces [11], [12], [13], [14], [15], [16].

The meta-atom is the single element representation of metamaterials. It is the smallest component that can produce the effective parameters that help to describe the behavior of metamaterials. Based on the effective parameters, the meta-atom can help engineer structures for metamaterials and characterize the expected behavior of the designs.

In the following subsections, the effective parameters will be described in detail. Methods to determine the effective parameters will be developed based on equivalent circuit modeling and a retrieval process to extract parameters from scattering parameters. The subsections will conclude with a discussion on implementing gain using active elements.

2.1.1. Metamaterials Effective Parameters

Stemming from a 1968 landmark paper by V. G. Veselago, the race to create negative refractive material structures has been gaining momentum. Veselago discusses the effect of the permittivity (ε) and the magnetic permeability (μ) on propagating electromagnetic waves [1]. Both ε and μ are the fundamental characteristic quantities that

المنارة للاستشارات
www.manaraa.com

determine the propagation of electromagnetic waves in matter. Both exist in Equation (2), the dispersion equation, which connects the frequency (ω) of a monochromatic wave and its wave vector (k).

$$\left| \frac{\omega^2}{c^2} \varepsilon_{ij} \mu_{ij} - k^2 \delta_{ij} + k_i k_j \right| = 0 \tag{2}$$

where c is the speed of light in a vacuum. For isotropic substances, the dispersion equation can be simplified into the following form.

$$k^2 = \frac{\omega^2}{c^2} n^2 \tag{3}$$

By knowing that n^2 is the square of the index of refraction of the substance, we can replace n^2 with the permittivity and permeability through this formal use of the refractive index.

$$n^2 = \varepsilon \mu \tag{4}$$

Expanding the components of n to account for lossy media allows the investigation of the lossy effects by argumentative or complex forms. Using the expansion of the refractive index,

$$n = \sqrt{|\varepsilon||\mu|}^{\,i\frac{1}{2}(\theta_\varepsilon + \theta_\mu)} \tag{5}$$

where θ_ε and θ_μ are the tensors representing the permittivity and permeability phase relationship; respectively. The permittivity and permeability can be separated and examined independently for effects on the refractive index and as a method to characterize what happens at the resonant frequency. In the argumentative form, the permittivity is

المنارة للاستشارات
www.manaraa.com

$$\varepsilon = |\varepsilon| e^{i\theta_\varepsilon} \tag{6}$$

which gives the magnitude ($|\varepsilon|$) and phase relationship ($e^{i\theta_\varepsilon}$) for permittivity. In the complex form, the permittivity is

$$\varepsilon = \varepsilon' + i\varepsilon'' \tag{7}$$

which expands the permittivity into a rectangular form. Where ε' is the real part denoted by the single quotation and ε'' is the imaginary part denoted by the double quotation mark.

For permeability, the argumentative and complex forms are expanded similar to permittivity in the following manner.

$$\mu = |\mu| e^{i\theta_\mu} \tag{8}$$

$$\mu = \mu' + i\mu'' \tag{9}$$

where μ' is the real part denoted by the single quotation and μ'' is the imaginary part denoted by the double quotation mark. Using the magnitude and phase relationship form, the refractive index can shift to a negative value when the argument of the ε and μ goes to π ($e^{i\pi} = -1$).

Determining the method to have negative refractive index started Veselago to theorize the possible opportunities of the double negative refractive index material. His theories would take time to develop and materialize. To have isotropic materials with a double negative behavior is difficult and as of yet hard to produce. Current research has shown results in anisotropic and bi-anisotropic materials. In our work, the meta-atom is considered as an anisotropic medium. The development of the permittivity and

المنارة للاستشارات
www.manaraa.com

permeability parameters to characterize the meta-atom will be based on the anisotropic behavior and the interaction with electromagnetic plane waves.

The tensors of anisotropic permittivity and permeability can be used to help show the latest development to engineered materials (metamaterials) which have double negative refractive index. Using the anisotropic tensors of permittivity and permeability has started metamaterials on a direction toward creating these structures up to isotropic behavior; however, the current progress remains at anisotropic and bi-anisotropic materials.

For anisotropic and bi-anisotropic materials, permittivity and permeability parameters respond differently than those observed by isotropic materials. The response is determined by the direction the electromagnetic wave travels and material parameters along that direction. Based on the type of material, these anisotropic and bi-anisotropic materials can be described using effective models. The anisotropic permittivity and permeability matrices are provided in several references to anisotropic materials [17], [18]. The tensors can be represented in a 3 x 3 square Cartesian matrix to show the interaction of each permittivity and permeability element based on direction.

$$\varepsilon = \begin{pmatrix} \varepsilon_{xx} & \varepsilon_{xy} & \varepsilon_{xz} \\ \varepsilon_{yx} & \varepsilon_{yy} & \varepsilon_{yz} \\ \varepsilon_{zx} & \varepsilon_{zy} & \varepsilon_{zz} \end{pmatrix} \quad (10)$$

المنارة للاستشارات
www.manaraa.com

$$\mu = \begin{pmatrix} \mu_{xx} & \mu_{xy} & \mu_{xz} \\ \mu_{yx} & \mu_{yy} & \mu_{yz} \\ \mu_{zx} & \mu_{zy} & \mu_{zz} \end{pmatrix} \tag{11}$$

For the meta-atom, the permittivity and permeability will be dependent on the propagation of the electromagnetic wave within the RF strip line. The RF strip line allows the use of simple orthogonal coordinates for permittivity and permeability based on the electromagnetic plane wave generated. For this reason, the EM plane wave will interact with the anisotropic meta-atom and have the electric field oriented in one direction normal to the center conductor. The magnetic field will be oriented normal to the electric field. The principle reason behind this electromagnetic wave orientation is to test meta-atoms with a fixed alignment and orientation. This will simplify the permittivity and permeability tensors needed to characterize the meta-atom behavior [19], [20], [21]. And limit the amount of unknown parameters that must be solved. The RF strip line is shown in Figure 3 with the direction of the electromagnetic plane wave propagation indicated at the beginning of the strip line. Having the RF strip line generate the electromagnetic plane wave illumination will aid the modeling and experimental verification for the meta-atom designs.

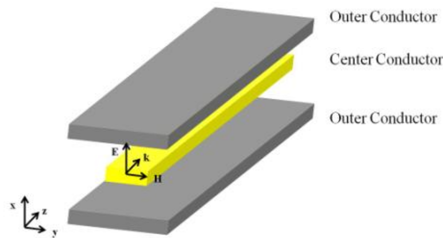

Figure 3. RF Strip Line used for electromagnetic plane wave propagation.

المنارة للاستشارات
www.manaraa.com

The permittivity and permeability models are described in detail by several authors [22], [23], [24]. To help understand this observation, meta-atoms are designed to exhibit specific electromagnetic properties at particular wavelengths that are much larger than the single meta-atom. One critical parameter to the responses is the resonant frequency. The resonant frequency (ω_0) is the point along the frequency spectrum where a large amount of dispersion occurs. Near the resonant frequency, the imaginary components of the permittivity, permeability and refractive index gain magnitude due to the resonance. By properly driving and enhancing the resonance, the permittivity or permeability material parameters can become negative in a frequency band slightly above the resonance frequency.

Using the resonant frequency, and the effective magnetic permeability model,

$$\mu(\omega) = 1 + \frac{f\omega^2}{\omega_0^2 - \omega^2 - i\Gamma\omega} \tag{12}$$

can describe the behavior for metamaterials where the fill factor (f) and damping factor (Γ) are associated with material losses. Smith *et al.* states that the fill factor depends on feature dimensions like the radius (r) and periodic spacing (a) by $f = \pi r^2/a^2$ [11]. The damping factor is directly dependent on the material resistivity (ρ), periodic distance (p) between layers and inversely dependent on the radius of the split ring by $\Gamma = (2\rho p)/(\mu_0 r)$ [11]. In our meta-atoms, the designs are square, so the length and the radius are based off dimensions of the square meta-atom.

المنارة للاستشارات
www.manaraa.com

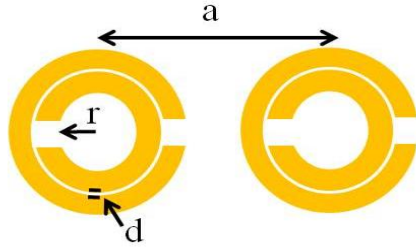

Figure 4. Split Ring Resonators

The effective permittivity model,

$$\varepsilon(\omega) = 1 - \frac{\omega_p^2}{\omega(\omega + i\gamma)} \tag{13}$$

where ω_p is the plasma frequency and γ is the damping factor, characterizes the anisotropic permittivity. The effective permittivity model describes the interaction of surface plasmons on thin metal wires. As shown in Figure 5 the thin metal wires can be arranged to behave as a low frequency plasma. This model is derived from the Lorentz model and tailored for thin metal wires [2], [25]. The effective permittivity is dependent on metal, dimensions and the induced electric field. The plasma frequency

$$\omega_p = \sqrt{\frac{Nq^2}{\varepsilon_0 m_{eff}}} \tag{14}$$

is characterized by the electron concentration (N), electron charge (q), permittivity and effective mass (m_{eff}) of the metal or semiconductor layers [2]. Plasma frequency is the natural frequency of oscillation in the metal at which free electrons and positive ions may be thought of as plasma. The damping factor (γ) is a damping term representing dissipation of the plasmon's energy into the system. The damping factor considers the conductivity (σ) of the metal, periodic spacing between the traces and the radius of the

المنارة للاستشارات
www.manaraa.com

trace ($\gamma=\varepsilon_0 a^2\omega_p^2/\pi r^2\sigma$) [25]. The effective permittivity is essentially negative below the plasma frequency and characterizes the thin wire in the meta-atom design.

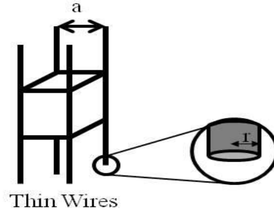

Figure 5. Periodic thin wire mesh

Using the effective parameters helps to determine the electromagnetic wave's response to the meta-atom. The effective permeability parameter depends on the resonance response of the meta-atom. The effective permittivity parameter depends on the plasma frequency of the meta-atom. Combining both parameters establishes the range where the negative index behavior occurs for metamaterials. Understanding the physical characteristics of the meta-atom leads to design, simulation expected experimental characteristics which can be defined by additional methods. Two methods that show my contribution to the metamaterials field are based on equivalent circuit modeling and parameter retrieval process to characterize meta-atom designs.

2.1.2. Meta-atom Equivalent Circuit Modeling

At resonance, meta-atoms can induce large amounts of dispersion in the effective medium parameters at frequencies close to the resonant frequency. The resonant frequency of meta-atom designs can be calculated using

www.manaraa.com

$$\omega_0 = \frac{1}{\sqrt{LC}} \tag{15}$$

which consists of lumped inductance (L) and capacitance (C) parameters used to describe the circuit behavior. Inductance and capacitance have been described by several researchers. Two commonly used definitions for inductance and capacitance will be described and used for defining lumped element models.

2.1.2.1. Lumped Elements

This section provides background information on two lumped elements used in meta-atom designs. Inductance and capacitance are two parameters that define the resonant frequency used in the effective parameters. In this section, each lumped element is described to provide an understanding into how the elements can be used for meta-atom designs.

The general inductance model is defined as

$$L = \frac{\mu_0 l^2}{t} \tag{16}$$

where l is the length of the conductor, t is the thickness of the conductor and μ_0 is the permeability constant. This induction model does not describe the reaction of the component to the internal current flow. A more detailed inductance model depends on the material, length (l), thickness (t), width (w), and total induced current on the component, wire, or trace. Based on applied current, inductance is defined as

المنارة للاستشارات
www.manaraa.com

$$L = \frac{\psi_{ij}}{I_j} \text{ for } I_k = 0 \text{ if } k \neq j, \tag{17}$$

where ψ_{ij} represents the magnetic flux in the loop due to a current I_j in the loop j [26]. From this definition, the self-inductance of any wire, loop, or filament can be described using the dimensions of the structure and the induced current. For instance, using a simple loop as shown in Figure 6 (a) the self-inductance of the loop can be determined by introducing a potential across the opening of the loop and tracing the current path around the loop.

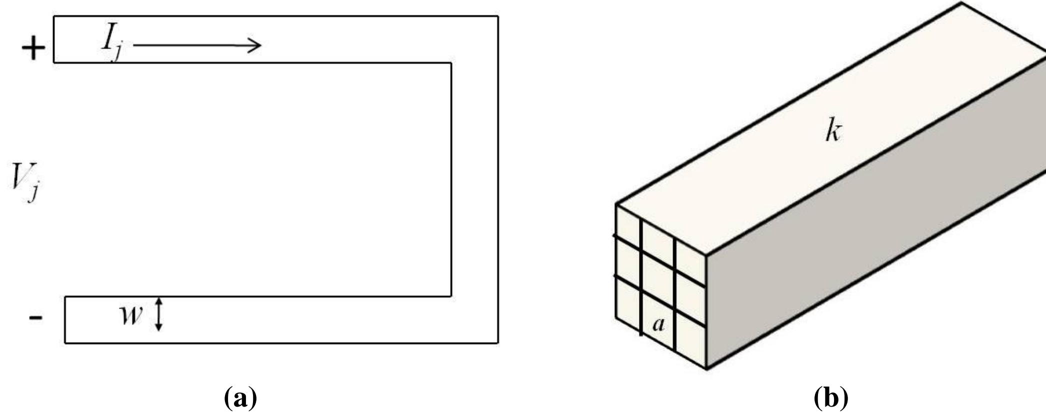

Figure 6 (a) Simple loop showing the voltage applied and the direction of the current flow. (b) sub-conductors (a) in a thin conductor (k) with cross-sectional area indicating the number of filaments in the wire.

In [26], Ruehli provides a derivation of partial self-induction per length which leads to a simplified equation for infinitely thin conductors

$$\frac{L_{P_{ii}}}{l} = \frac{\mu}{6\pi}\left\{3\ln[u+(u^2+1)^{\frac{1}{2}}]+u^2+u^{-1}+3u\ln[\frac{1}{u}+(\frac{1}{u^2}+1)^{\frac{1}{2}}]-[u^{\frac{4}{3}}+(\frac{1}{u})^{\frac{2}{3}}]^{\frac{3}{2}}\right\} \tag{18}$$

where μ is the permeability and u is defined as the ratio of the l to the w. For this simplified equation, the ratio of the thickness to the width of the conductor is considered less than 0.01.

المنارة للاستشارات
www.manaraa.com

From the derivation of infinitely thin conductors, Ruehli goes on to give the equation for partial self-inductance of rectangular conductors with an arbitrary cross section [26]. Using Figure 6 (b), given a straight conductor k of length l with an arbitrary cross section, let the conductor cross section be approximated by a set of sub-conductors each having rectangular cross section (a); then the partial self-inductance is given by

$$L_{P_{kk}} = \left[2\sum_{i=1}^{N-1} \sum_{j=i+1}^{N} \text{cof } L_{P_{ij}} + \sum_{i=1}^{N} \text{cof } L_{P_{ij}} \right]^{-1} \det L_P \, , \tag{19}$$

where **cof** indicates the cofactor of the element in the matrix and **det** is the determinant with the summation conducted over the conductor's area. The definition of inductance for each sub-conductor is

$$L_{P_{ij}} = \frac{V}{s\sum_{i=1}^{N} I_i} \tag{20}$$

where the voltage drop (V) and the sign (s) associated with the direction (±1) and frequency of current flow (I) to solve the self-inductance [26]. Since the voltage drop along the sub-conductors is related to the current vector by $\mathbf{V} = s\mathbf{L_P I}$ and since all voltages along the conductor are equal to $V_i = V$. Use is made also of the symmetry of the matrix of partial sub-inductances [26].

From this derivation, the calculation of the partial self-inductance for complex traces or circuits can be solved using Equation (18) or Equation (19). CoventorWare ®, a finite element model program, determines the inductance of our designs using an integral equation approach combined with a multipole-accelerated solution algorithm [26], [27], [28]. The use of this simulation helps with the evaluation of the complex layouts showing

المنارة للاستشارات
www.manaraa.com

how the inductance changed with design modifications. These simulations will be discussed in section 4.3.

Capacitance is the measure of a capacitor's ability to store an electric charge on plates. The charge is built up on the plates by creating a voltage potential difference between the plates. Figure 7 shows the diagram that demonstrates the buildup of charge on plates by a voltage source. This model not only describes capacitance but also shows a parallel plate capacitor, the simplest capacitor model.

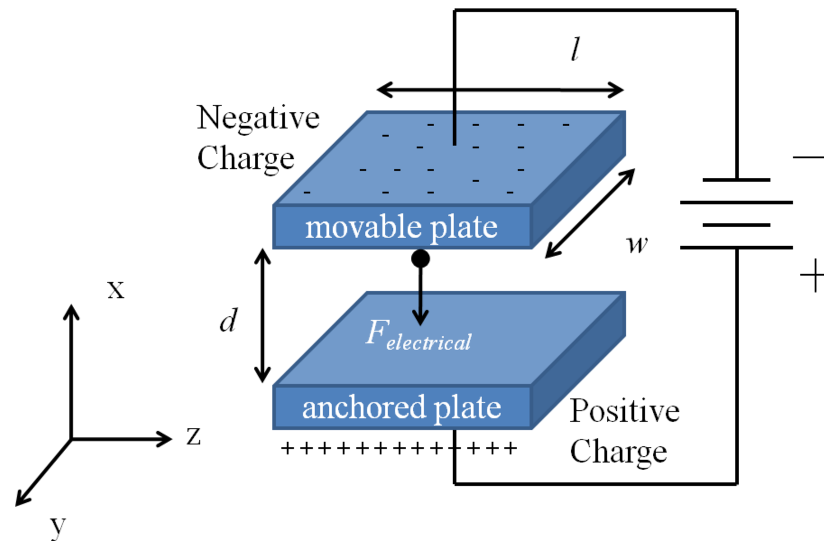

Figure 7. Parallel Plate Capacitor

Three factors contribute to the capacitance of a capacitor. The first factor is permittivity or dielectric constant of the insulator. The second factor is the surface area of the plates that build up charge. And the third factor is the distance between the plates which is inversely related to the capacitance. Each is represented in the capacitance analytical model

المنارة للاستشارات
www.manaraa.com

$$C = \varepsilon_0 \varepsilon_r \frac{Area}{d} \tag{21}$$

where ε_0 is the absolute permittivity, ε_r is the relative permittivity, *Area* is surface area of the plates, and *d* the distance between the plates.

The parallel plate capacitor model and the physical capacitor component have useful applications in DC and AC operations. For DC operations, the charge builds up until the potential equals the source voltage and stops the flow of current in the circuit. At AC operations, the capacitor acts like a voltage source because it builds up and drains the potential energy from the plates.

A capacitor can have a fixed value or be manufactured as a variable component. In order to change the capacitance of the capacitor one of the three factors must be adjustable. Two commonly used methods to vary capacitance are adjusting the distance between the plates or changing the overlapping surface areas of the two plates. Besides the parameters found in the simple capacitor model, additional factors must be considered to fully characterize the capacitor.

The parallel plate capacitor is a commonly used model to help determine capacitance. However, incorporating a dielectric or insulator into the gap along with an air gap complicates the analysis of the parallel plate capacitor. The dielectric creates its own charge on the component and causes a shift in the overall capacitance. The dielectric and air gap can be considered as two parallel plate capacitors in series. The analytical approach to calculate the expected capacitance is to consider two capacitors in a series capacitance model

المنارة للاستشارات
www.manaraa.com

$$C_{combined} = \frac{1}{\frac{1}{C_{dielectric}} + \frac{1}{C_{air}}} = \frac{1}{\frac{t}{\varepsilon_0 \varepsilon_r wl} + \frac{d}{\varepsilon_0 \varepsilon_{air} wl}} = \frac{wl \varepsilon_0 \varepsilon_r \varepsilon_{air}}{t \varepsilon_{air} + d \varepsilon_r} \quad (22)$$

where t is the thickness of the dielectric. Based on the model, the thickness of the dielectric causes the total capacitance to decrease as the thickness of the material increases.

Another factor to consider for capacitors is the fringing effect on the plates. Fringing fields develop around the edge of the capacitor plates. Figure 8 shows the fringing effect on a one dimensional model. The fringing fields cause changes to the capacitance to account for these edge effects.

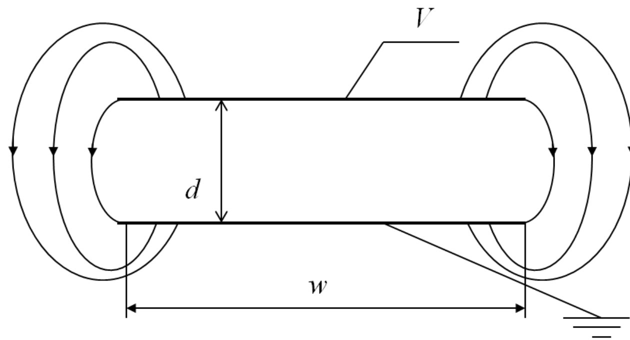

Figure 8. Capacitor model showing the fringing effect.

Two models were found in previous research conducted by Palmer *et al.* and Yang *et al*. And based on these models an improved approximation is described by Leus *et al.* which combines the models to increase the accuracy of the computation [29]. Based on the parallel plate with fringing effect the one dimensional capacitance model becomes

$$C = \varepsilon_0 \varepsilon_r \frac{w}{d}\left(1 + \frac{2d}{\pi w}\ln\left(\frac{\pi w}{d}\right) + \frac{2d}{\pi w}\ln\left(1 + \frac{2t}{d} + 2\sqrt{\frac{t}{d} + \frac{t^2}{d^2}}\right)\right) \quad (23)$$

where t represents the thickness of the metal plate, w is the width and d is the spacing between plates. Within the model, the first term defines the capacitance. The second term

المنارة للاستشارات
www.manaraa.com

defines the fringing field due to finite dimensions of the plate. Finally, the third term defines the fringing field associated with the thickness of the plates which vanishes for zero-thickness plates.

Another capacitance model that considers first-order fringing field was developed by Osterberg and Senturia [30], [31]. This capacitance model,

$$C = \frac{\varepsilon_0 \varepsilon_r Area}{2d}\left[1 + 0.42\frac{d_0}{w}\right] \tag{24}$$

where d is the distance between plates, d_0 is the initial distance and w represents the width is based on overlapping parallel plates. In this analytical equation, the capacitance model is an adjusted model used to account for non-parallel electric fields that develop outside the confines of the parallel plate capacitor. The first-order fringing field is due to an oversized conducting plate interacting with a smaller plate (such as a cantilever beam) which creates additional fields outside the overlapping plates. The model accounts for variations in the total capacitance and will be used in the analytical sections to determining capacitance.

Based on the capacitance and the factors that are used to determine the value of capacitors, the analytical solution can be used to determine designs for meta-atom designs and electrostatic actuated MEMS. As a first order approximation, the parallel plate capacitor which accounts for fringing fields will be used to help determine design requirements for tunable meta-atom designs. The background on inductance and capacitance will be used to help build on the contribution to meta-atom design using equivalent circuit modeling and for MEMS.

المنارة للاستشارات
www.manaraa.com

2.1.2.2. Equivalent Circuit Modeling

To understand the behavior of the meta-atom, the equivalent circuit model can be applied to simulate responses similar to experimental results using inductance and capacitance lumped elements. After acquiring test results for the 1 – 4 GHz baseline meta-atom, the frequency response was plotted for the transmission response. Figure 9 shows the results from the 1 – 4 GHz meta-atom design indicating response characteristics for a bandstop filter at the resonant frequency.

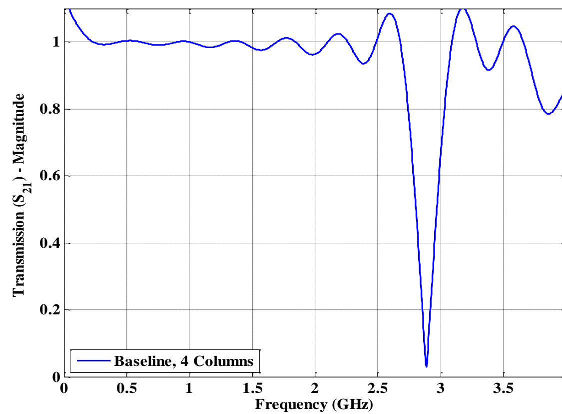

Figure 9. 1 – 4 GHz meta-atom transmission response with resonance at 2.83 GHz.

The equivalent circuit model that closely resembles the resonant response is the series resonant bandstop filter which causes a short circuit at the resonant frequency and does not allow a band of frequencies to pass voltage to a load. The simplest bandstop filter design consists of a capacitor and inductor in series resonating at a specific frequency. Figure 10 shows the series resonant bandstop filter which combines the capacitor and inductor components in series. The circuit model has two operational states. One operational state is outside the resonance bandwidth where the RF signal continues to propagate to the output of the model. The second operational state occurs within the

www.manaraa.com

resonance bandwidth where the RF signal shorts through the series resonant bandstop filter and does not propagate to the output.

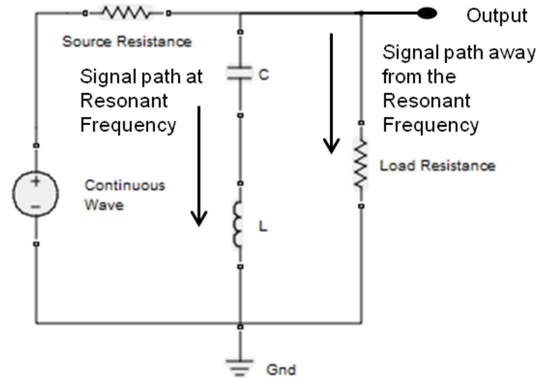

Figure 10. Series Resonant Bandstop Filter Equivalent Circuit

Knowing the equivalent circuit response depends on the capacitor and inductor values at resonance, the simple model can be used to obtain a first order approximation for the meta-atom characteristics. This model will be the further investigated using experimental data and simulations to build a model that considers the interaction of propagating signals and the meta-atom. For example, by properly driving and enhancing the resonance, one can cause the effective material parameters ε or μ to become negative in a frequency band slightly above the resonance frequency [2].

Lumped elements in equivalent circuit modeling are common in the microwave and RF regime; however, these circuit elements have played a limited role in optics [32], [33], [34]. There has always been a jump from electromagnetic models to plasmons at optical frequencies. Lumped optical circuit models are now available for metallic nano-spheres, split-ring resonators and nanorods, but the simplest case of the electrical circuit for a flat metallic surface plasmon has not been presented [35]. In [35], electrical circuit

www.manaraa.com

descriptions for bulk plasmons, single surface plasmons and parallel-plate plasmons are discussed. For these plasmons, simple circuits can reproduce the exactly known frequency versus wave-vector dispersion relations, with reasonable accuracy. The circuit paradigm directly provides a characteristic wave-impedance that is rarely discussed in the context of plasmonics. Now, for metal-optics, the wave propagation can be modeled using a one-dimensional distributed element transmission line based on transmission line dispersion and wave impedance. The simplest metal-optics circuit model incorporates capacitance, Faraday inductance, and also includes kinetic inductance arising from the inertia of the electrons in a metal. Kinetic inductance dominates over Faraday inductance for devices with characteristic dimensions smaller than the collision-less skin depth. When kinetic inductance dominates over Faraday inductance, the frequency region is called the plasmonic regime. Based on the metal-optics response, the model must include all three circuit components. To help explain the modeling, Staffaroni *et al.*, provide detail on kinetic inductance and how it arises from the simple *LC* circuit model [35]. They also discuss the link between metal dielectric constant and resistivity, whose imaginary part represents kinetic inductance. Finally, they demonstrate equivalent transmission line circuits for surface plasmon waves on a single metal surface, and between a parallel plate metal waveguide [35]. Based on their research, the equivalent circuit model used for meta-atoms must be considerate of the frequency regime and the structural design.

المنارة للاستشارات
www.manaraa.com

2.1.3. Retrieval Process for Effective Parameters

Another approach to finding the effective permeability and permittivity is using the retrieval process described by Smith *et al.* and Chen *et al.* [36], [37] where the known scattering parameters (S-parameters) can be used to determine the refractive index and impedance. This retrieval process is important for simulation and experimental data verification. Beginning with the definition for S-parameters,

$$S_{11} = \frac{\mathbf{E}_{refl}(z=0)}{\mathbf{E}_{inc}(x=0)} \tag{25}$$

$$S_{21} = \frac{\mathbf{E}_{trans}(z=d_1+d+d_2)}{\mathbf{E}_{inc}(z=0)} \tag{26}$$

$$S_{12} = S_{21} \tag{27}$$

where $\mathbf{E}_{inc}$, $\mathbf{E}_{refl}$ and $\mathbf{E}_{trans}$ are the incident, reflected and transmitted electric fields; respectively, as observed by a plane wave within a parallel plate waveguide.

Computing the impedance (z) from the S-parameter values is performed using

$$z = \pm\sqrt{\frac{(1+S_{11})^2 - S_{21}^2}{(1-S_{11})^2 - S_{21}^2}} \tag{28}$$

where, the S-parameter data is collected over a frequency spectrum.

To determine the refractive index (n), a derivation must be completed on the following equation to solve for real and imaginary refractive index values.

$$e^{ink_0d} = X \pm i\sqrt{1-X^2} \tag{29}$$

where $X = (1 - S_{11}^2 + S_{21}^2)/(2S_{21})$ [2]. The advantage of this intermediary step is that the index of refraction and the impedance are physical quantities upon which a series of

المنارة للاستشارات
www.manaraa.com

requirements can be imposed. For instance, if the material is passive, the requirement that Re (z) ≥ 0 fixes the choice of the sign on the impedance.

Rearranging Equation (29) to solve for the refractive index leads to a complex solution

$$n = \frac{1}{k_0 d}\left\{\left[\operatorname{Im}\left(\ln\left(e^{ink_0 d}\right)\right) + 2m\pi\right] - i\left[\operatorname{Re}\left(\ln\left(e^{ink_0 d}\right)\right)\right]\right\} \quad (30)$$

that when solved, careful attention must be taken to select the correct solution. Inspecting the solution and setting Im (n) ≥ 0 leads to an unambiguous result for Im (n). For the integer (m), which is related to the number of wavelengths that propagate inside the slab, short samples must be chosen to ensure the sample is smaller than one wavelength, thus automatically selecting $m = 0$ is a good solution. The Re (n) is not a problem for metamaterial designs; in fact, it helps identify regions which are left-handed.

To determine the electric permittivity and magnetic permeability, the refractive index and impedance derived from the S-parameters can be used for solutions where

$$\varepsilon = \frac{n}{z} \quad (31)$$

and

$$\mu = nz \quad (32)$$

Both n and z, and therefore ε and μ, are frequency dependent complex functions that satisfy certain requirements based on causality [30]. This calculation is carried out in MATLAB and used on S-parameter simulation and experimental data sets.

المنارة للاستشارات
www.manaraa.com

2.1.4. Compensating for loss at resonant frequency

An active material incorporated into the meta-atom is a method to compensate for loss associated with dispersion [22], [38], [39], [40], [41], [42], [43]. The anisotropic parameters for permittivity and permeability model the loss observed in the meta-atom structure by the damping factors. The main issue of loss is the damping of the response which reduces the null at the resonant frequency. To compensate for the loss, active materials that generate a gain at the resonant frequency are considered possible solutions. Components and materials used by other researchers include RF amplifier, tunable phase shifter, Rh800-epoxy, and optical parametric amplification [40], [38], [39], [41]. Based on the previous research conducted to compensate for loss, a low noise amplifier will be integrated in the design and used to demonstrate that loss can be controlled by a gain medium. Details of the design will be covered in section 3.4. The experimental results will be discussed in section 5.4.

2.2. Microelectromechanical Systems

Microelectromechanical Systems (MEMS) applications involve sensors and actuators, collectively known as transducers [44]. Two MEMS technologies relative to metamaterials are RF MEMS and Optical MEMS. Examples of RF MEMS include micromachined relays, tunable capacitors, micro-integrated inductors and solenoid coils, resonators and filters, and antennas. Examples of Optical MEMS are binary optical lenses, diffraction gratings, tunable optical mirrors, interferometric filters, and phase modulators for applications including optical display, adaptive optics, tunable filters, gas spectrum analyzers, and network routers.

المنارة للاستشارات
www.manaraa.com

MEMS sensing and actuation involves transforming signals or power from one energy domain to another. There are six major energy domains of interest: 1. Electrical, 2. Mechanical, 3. Chemical, 4. Radiative, 5. Magnetic, and 6. Thermal. The electrical, magnetic and radiative domains are used in metamaterials research to help understand the material and electromagnetic parameters of metamaterial designs. The parameters include electromagnetic waves, infrared radiation, absorption, transmission, voltage, current, current density, capacitance, inductance and electrostatic actuation. Capacitance, inductance and electrostatic actuation are the three main parameters used to combine metamaterial designs and MEMS.

Combining MEMS with the baseline SRR offers a unique way to have variable resonance shifts from an otherwise static design. MEMS provide the ability to use micro-mechanical devices in applications at the macro scale. Incorporating MEMS into the SRR gives the ability to bring functional mechanical capabilities into meta-atom designs at the micro-level which is essential for varying capacitance on small structures.

2.2.1 MEMS Fabrication

MEMS fabrication consists of a portfolio of techniques. These techniques are derived from the integrated circuit industry and are based on micromachining. Micromachining combines lithography, thin film processing and sacrificial layer etching to form mechanical devices. The three types of micromachining fabrication processes are bulk micromachining, microforming and surface micromachining. Each fabrication process will be discussed in the following subsections to provide information on MEMS fabrication.

المنارة للاستشارات
www.manaraa.com

2.2.1.1. Bulk Micromachining

Bulk micromachining is the creation of microstructures by bulk etching of material from the substrate by anisotropic/isotropic wet/dry etching or reactive ion etching. It is a subtractive process. For example, on a silicon substrate the silicon is removed from the bulk of the substrate using etching to form features. In processing a bulk material, the substrate is the key to the outcome of the process. Many bulk micromachining processes are customized for particular applications. Large features and structures are the expected outcome from the process.

Beginning with the substrate, masking is performed with thin films. Etching is the next process step to remove undesired material. The key to making etching useful is to precisely and with repeatable results control the material that is removed. After the etching process, wafer bonding is completed to add additional material for further processing.

Wafer bonding is used to create high-aspect ratios for multilayer structures, sealed cavities and multi-level chambers to name a few examples. The types of wafer bonding are anodic bonding, fusion bonding and other low temperature methods. Anodic bonding is caused by a force with voltage applied across the interface. Fusion bonding is caused by covalent bonding and highly dependent on surface preparation, contact surface and annealing temperature. An example of low temperature bonding is adhesive bonding [45]. For low temperature adhesive bonding, the representative adhesive layers include photoresist, polymer adhesive and spin-on glass adhesive [44]

المنارة للاستشارات
www.manaraa.com

2.2.1.2. Micromolding

Micromolding is commonly referred to as a process called LIGA. The word LIGA is an acronym that stands for the main steps of its process: deep X-ray lithography, electroplating (Galvanoformung in German) and injection molding (Abformung in German) [44]. Early developers of the LIGA process recognized the broader implications of the process as a new means of low-cost manufacturing of a wide variety of microparts previously impossible to batch fabricate [46]. It involves patterning a thick layer of photoresist with high-energy beams produced by a synchrotron radiation (SR) X-ray source. The photoresist is developed for structures with deep vertical walls and high aspect ratios. Electroplating is conducted to fill the cavities with metal. The metal piece is harvested by removing the resist and can be used as a precision metal part, or as a mold for the batch fabrication of plastic parts [44].

The latest development in micromolding is the use of deep X-ray lithography (DXRL) exposures which uses a critical dose underneath the absorber to avoid development. The critical dose consists of a top dose used at the top resist layer before bubble formation occurs and a bottom dose which is the minimum dose needed at resist to substrate interface to completely dissolve the resist. Key features of DXRL microstructures are the ability to define arbitrary shapes, structure heights up to several millimeters, minimum feature sizes in the order of micrometers, sub-micrometer topographical details, vertical sidewall profile and smooth sidewalls. DXRL has provided the ability of three-dimensional X-ray lithography based on a technique to tilt and rotate the assembly of an X-ray mask and a resist coated substrate exposed to incident X-rays [47].

المنارة للاستشارات
www.manaraa.com

2.2.1.3. Surface Micromachining (polyMUMPS ®, SUMMIT V ™)

Surface micromachining is based on integrated circuit fabrication techniques. This process builds up microstructures on the surface of the wafer (silicon, quartz) by making use of the full lithography capability of integrated circuit processing. The processes commonly involve deposition, patterning and removal of various layers of silicon dioxide, polysilicon, phosphosilicate glass (PSG) and silicon nitride [48]. Thin films are the main structural materials along with the sacrificial layers. Surface micromachining is considered a planar process because of the well defined process layers. Examples of surface micromachined devices are single layer structures like cantilevers, bridges and sealed cavities. There are movable in-plane structures like parts for turbines, gear train and micro-motors. Micro-hinges and flip up structures can also be made with surface micromachining. Two foundry processes are based on the surface micromachining process which are Polysilicon Multi-User MEMS processes (polyMUMPS ®) and Sandia Ultra-planar, Multi-level MEMS Technology (SUMMiT V ™).

PolyMUMPS ® was started in 1992. It began as a foundry to produce MEMS in a commercially available surface micromachining process [49]. The foundry provides a process with a crystalline silicon wafer, silicon nitride layer, three polysilicon layers, two silicon dioxide layers and a metal layer. Various structures are possible from this process which range from accelerometers, micro-motors, microfluid channels, tunable mirrors, capacitors and inductors. Figure 11 shows the layers currently available for the polyMUMPS ® process.

المنارة للاستشارات
www.manaraa.com

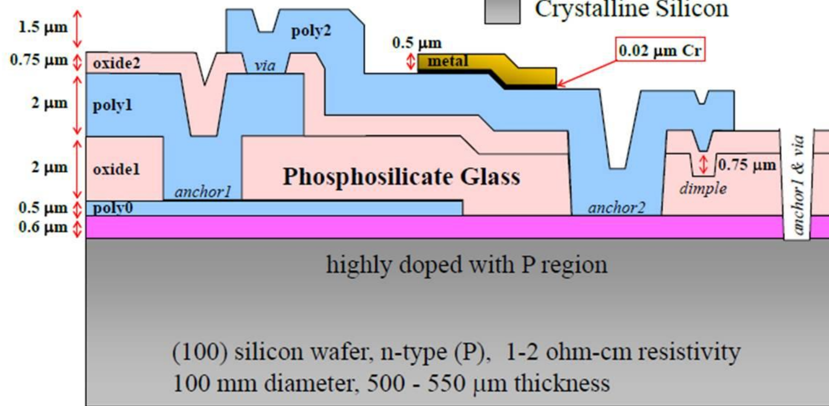

Figure 11. PolyMUMPS ® layers and dimensions for MEMS. The layers provide structures to build devices with a surface micromachine process.

Since polyMUMPS ® is a commercial foundry, the processing data for each layer is available to help with designs. Table 1 shows the polyMUMPS ® process run number 83 material information as an example for the characteristics of each layer.

Table 1. PolyMUMPS ® Run #83 material information

PolyMUMPS ® Layer Data Run #83 150mm wafers					
	Thickness (Å)	**Standard Deviation (Å)**	**Sheet Resistance (ohm/sq)**	**Resistivity (ohm-cm)**	**Stress (MPa)**
Nitride	6,015	239	-	-	108 T
Poly0	5,026	32	32	1.61E-03	33 C
Oxide1	19,477	293	-	-	-
Poly1	19,867	161	12	2.38E-03	8 C
Oxide2	7,054	97	-	-	-
Poly2	14,880	12	24	3.57E-03	9 C
Metal	5,204	-	0.056	2.91E-06	21 T

The Sandia Ultra-planar, Multi-level MEMS Technology is available as a four or five-layer polycrystalline silicon surface micromachining process based on SUMMiT

المنارة للاستشارات
www.manaraa.com

IV™ or SUMMiT V™ fabrication process. The fabrication process is a batch fabrication process using conventional integrated circuit processing tools. Using this technology, high volume and low-cost production can be achieved. Common processing challenges, such as topography and film stress are overcome using these processing methods. For example topography issues are mitigated by using chemical-mechanical polishing to achieve planarization. The stress is maintained at low levels using a proprietary process [50]. MEMS are produced by alternately depositing a film, photolithographically patterning the film, and then performing chemical etching. By repeating the process with layers of silicon dioxide and polycrystalline silicon, interconnected three-dimensional shapes can be formed [50]. Figure 12 shows the mechanical layers used in the SUMMiT V™ fabrication process.

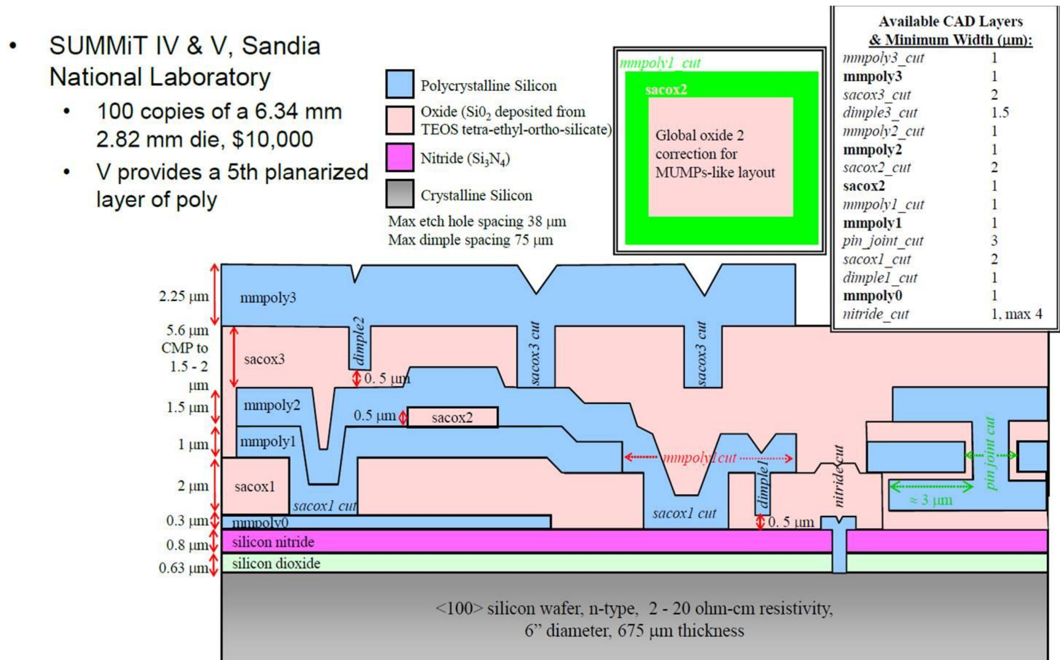

Figure 12. SUMMiT IV & V™ fabrication layers. The polysilicon layers are the structural mechanical layers.

المنارة للاستشارات
www.manaraa.com

2.2.1.4. MEMS Fabrication Method for Meta-atoms

Three MEMS fabrications techniques were discuss in the previous subsections. The decision on which fabrication technique to use for research revolves on three factors. The first factor is the availability of materials to build the meta-atoms. The meta-atom must consist of metal or semiconductor split-ring resonators and traces. The split-ring resonators must be separated with insulating materials to build up surface charge. Second, the method to establish the structures must be repeatable over large surface area. Third, the fabrication method must allow the integration of tunable features that can shift the resonant frequency. Surface micromachining fabrication provides solutions to all these factors. And, an additional benefit is the ability to use clean rooms at AFIT and AFRL to process the meta-atoms.

2.2.2. Actuation Methods

MEMS actuation mainly involves the movement of structures by either electrical or thermal excitations. Actuation methods examined in the research are electrothermal, piezoelectric and electrostatic actuation. Each actuation method has unique characteristics for actuating devices. And, each method can be accomplished using surface micromachining fabrication.

Electro-thermal actuators operate based upon thermal expansion properties of materials used to fabricate the MEMS devices. In principle, as a current is passed through a MEMS conductor, Joule heating causes the material of the conductor to increase in temperature. As the material of the beam heats up, the thermal expansion of

المنارة للاستشارات
www.manaraa.com

the material causes the beam to elongate. Figure 13 depicts this elongation effect of a MEMS beam and can be described by

$$L_{new} = L_0 + \alpha_L [L_0 (T_{avg} - T_0)] \tag{33}$$

where L_{new} is the new beam length; L_0 is the initial beam length; α_L is the coefficient of linear thermal expansion; T_{avg} is the average final temperature of the beam; and, T_0 is the initial temperature before current flow [51]. The change in beam length can be utilized in various configurations to create mechanical displacements in MEMS devices. A major disadvantage of electro-thermal devices is the much slower actuation response times and power requirements. Once the applied voltage is removed, these devices must cool using thermal conduction and convection. Given the operational attributes of these devices, they tend to be highly suited for the physical movement of larger MEMS objects; however, they are very poor when high repetition and speed is required [52], [53], [54], [55].

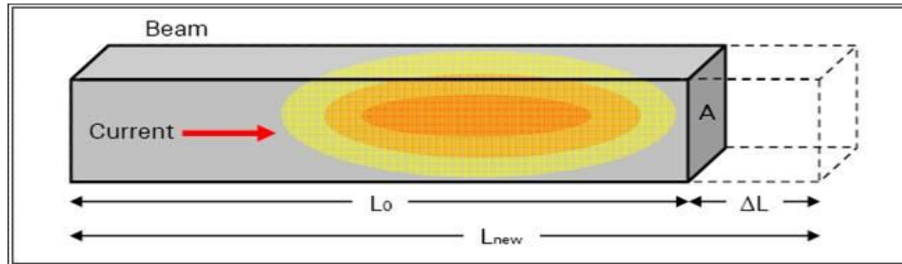

Figure 13. MEMS electro-thermal technique illustrating beam elongation due to Joule heating caused by current flow through the conductor material

The piezoelectric actuation is based on using piezoelectric material where an applied voltage induces an internal stress [44]. Zinc Oxide is a common material found in piezoelectric actuators [44]. By applying an external voltage, the internal stress changes

المنارة للاستشارات
www.manaraa.com

and creates a longitudinal strain along the axis of the material. Actuation results from an expansion of the material which can be used to create displacement.

Electrostatic actuation is based on using an applied electric field to generate a force. The electric field acts on induced or permanent charges to generate a electrostatic force between conductors. Advantages to using electrostatic actuation are low power operation and high response speed. One disadvantage is the small range of motion. Another disadvantage is the large footprint required to generate large force and displacement. Despite the disadvantages, electrostatic actuation offers the best actuation choice to build tunable meta-atoms. Based on the decision to use electrostatic actuation, more detail will be developed to understand this actuation method and provide a contribution to meta-atom designs in the following subsections.

2.2.3. Electrostatic Actuation

Electrostatic actuation is described as the force generated when an applied electric field acts on induced or permanent charges [44]. The electrostatic force is a result of this actuation and is defined as a surface force on a moving particle due to applied electric fields [44]. To help understand electrostatic actuation, the simple parallel plate capacitor can be used to derive the force based on the electrostatic potential energy stored in the capacitor. The dimensions of the capacitor in Figure 14 are width (w), length (l) and gap (d).

المنارة للاستشارات
www.manaraa.com

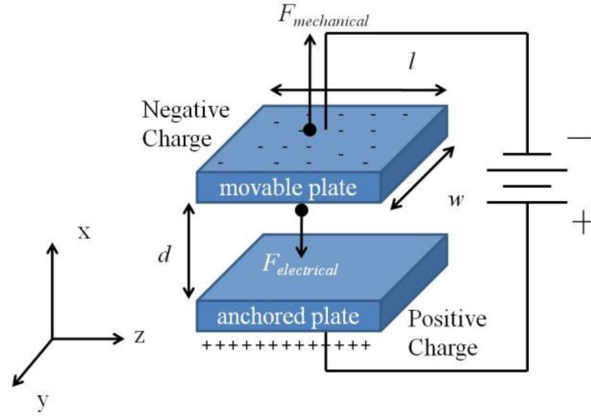

Figure 14. Parallel plate capacitor used to describe electrostatic actuation.

The maximum electrostatic potential energy, $E_{e,m}$, stored in the capacitor is

$$E_{e,m} = \frac{\varepsilon_0 \varepsilon_r w l V_b^2}{2d} \quad (34)$$

where V_b represents the electrical breakdown voltage and $\varepsilon_0\varepsilon_r wl/d$ the capacitance (C) [46]. When moving one plate of the capacitor with respect to the other in any direction, the electrostatic force involved is the negative spatial derivative in the direction of the stored energy E_e [46]. A movement of one plate in a microactuator (i.e. cantilever) in any direction leads to a force (F). For example a translational movement of one plate in a microactuator in the direction, x, leads to a force, F_x, as

$$F_x = -\frac{\partial E_e}{\partial x} = -\frac{V^2}{2}\frac{\partial C}{\partial x} \quad (35)$$

where V is the applied voltage [46]. For two plates of a parallel capacitor in a microactuator displaced perpendicular to each other in the x-direction, the force at its starting position is given as

$$F_x = \frac{\varepsilon_0 \varepsilon_r w l V^2}{2d^2} = \frac{1}{2}\frac{CV^2}{d} \quad (36)$$

المنارة للاستشارات
www.manaraa.com

This force will tend to decrease the gap, which gives rise to displacements and the mechanical restoring force ($F_{mechanical}$). The $F_{mechanical}$ is defined using Hooke's Law

$$F = k_m d \tag{37}$$

where k_m is the mechanical spring constant and d represents the gap. Under static equilibrium, the mechanical restoring force has an equal magnitude but opposite direction as the electrostatic force ($F_{electrical}$). Setting the mechanical restoring force and electrostatic force equal to each other allows you to determine the voltage necessary to move the plate. To help simplify the equation, two variable changes are required on the force equations. The first change is replacing mechanical distance (d) with x. And the second change involves replacing the new equilibrium position with ($x_0 - x$). This provides the voltage equation,

$$V = (x_0 - x)\sqrt{\frac{2k_m x}{\varepsilon_0 \varepsilon_r wl}} \tag{38}$$

where the voltage can be used to help determine pull-in distance and pull-in voltage. The pull-in distance is determined by finding the maximum or minimum point for the change in the voltage equation based on the change in gap distance. Using the derivative of voltage equation,

$$\frac{dV}{dx} = 0 = (x_0 - x)\sqrt{\frac{2k_m}{\varepsilon_0 \varepsilon_r wl}}\frac{1}{2}x^{-1/2} + \sqrt{\frac{2k_m}{\varepsilon_0 \varepsilon_r wl}}x^{1/2}(-1) \tag{39}$$

the derivative can be solved for the pull-in distance of $x = x_0/3$. Plugging the pull-in distance into the voltage equation provides the model for determining the pull-in voltage

المنارة للاستشارات

www.manaraa.com

$$V_{pi} = (x_0 - \frac{x_0}{3})\sqrt{\frac{2k_m \frac{x_0}{3}}{\varepsilon_0 \varepsilon_r wl}} = \frac{2x_0}{3}\sqrt{\frac{k_m}{1.5C_0}} \tag{40}$$

which can be used to determine the electrostatic actuation voltage for MEMS cantilevers.

The mechanical spring constant (k_m) calculated using parallel plate capacitor in Figure 14 with a loading force applied normal to the movable plate is,

$$k_m = \frac{Ewt^3}{4l^3}, \tag{41}$$

where E is the Young's modulus of the material, w is the width, t is for the thickness, and l is the length [38]. By actuating the movable plate, the capacitance can shift based on the distance of the gap and the biasing voltage.

The principle for electrostatic actuation on parallel plate capacitors applies to electrostatically actuated MEMS cantilevers. The cantilever is a device used in MEMS to transfer signals, actuate a circuit or act as a sensor. The cantilever is defined as a fixed-free beam anchored at one end and free to move at the other end. The beam can be made out of several different types of materials, but copper, gold and semiconductors are common materials used in the MEMS industry.

The cantilever dimensions and material properties are two factors that can determine the cantilever operation. The dimensions considered for cantilever operation are beam width, length and thickness. The dimensions help define the degrees of freedom (DOF) the beam can move. Figure 15 shows the cantilever with labeled dimensions. Based on the dimensions, the cantilever can bend when subject to an applied force. The location and amount external force exerted on the cantilever causes the cantilever to

المنارة للاستشارات
www.manaraa.com

deflect out of plane. The material properties that effect the cantilever operation are internal stress due to the material and beam's spring constant which includes the Young's modulus. For example, the internal stress deflects the beam when trying to compensate for residual material stress.

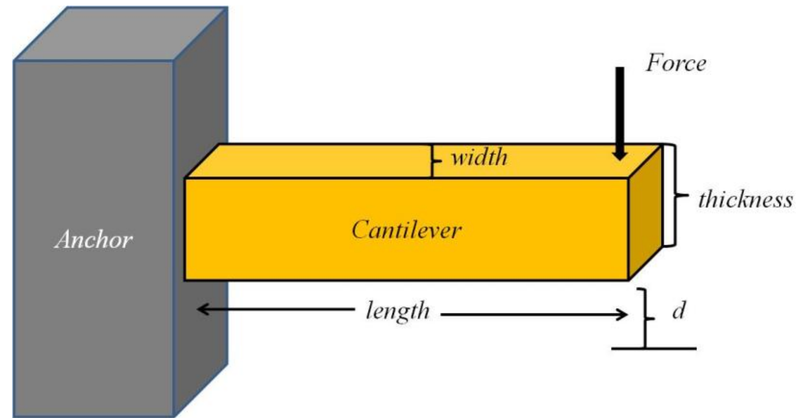

Figure 15. Cantilever

The parallel plate capacitor model was defined in Equation (21) to describe the capacitance between two adjacent metal plates or structures. Equation (21) can apply for MEMS cantilevers which can be integrated into meta-atom structures for variable capacitor components. In fact, the cantilevers will be used on split ring resonators to vary the capacitance. The MEMS cantilever has been studied for many applications besides RF MEMS. The cantilever which is shown in Figure 16 is a simple illustration of the cantilever structure which consists of a beam, anchor, actuation pad covered with dielectric, an air gap and signal pad coated with a dielectric material to avoid shorting out the device. Details on various parameters the effect the actuation for the cantilever beam will be discussed in detail in the following subsections. Each subsection builds on my contributions that help to understand the expected actuation response for the cantilever.

المنارة للاستشارات
www.manaraa.com

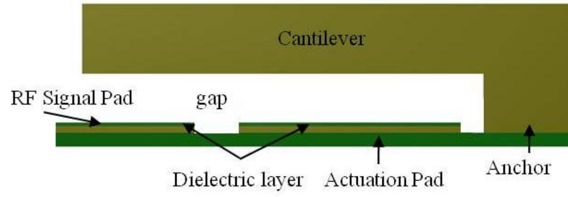

Figure 16 Simple cantilever beam with actuation pad covered with a thin dielectric layer for short circuit protection.

2.2.3.1. Fringe effect on cantilevers

Using the actuation pad and cantilever depicted in Figure 16, the fringing effect responsible for changing the capacitance can be described using Equation (24). As the overlapping area of the cantilever and actuation pad changes, the total fringing capacitance is altered by the structural modifications. Incorporating the fringing effect, the total capacitance increases as a function of the overlapping area.

2.2.3.2. Dielectric effect on cantilevers

The actuation pad is used to pull the cantilever down reducing the air gap thus increasing the capacitance. Adding the dielectric material within the gap further complicates the design by having a material within the gap which must be included in the capacitance calculation. To include the effect of the dielectric material, Equation (22) must be used and modified by the properties of the dielectric layer. Now the capacitor model,

$$C = \frac{1}{\frac{1}{C_{air}} + \frac{1}{C_{Si_3N_4}}} = \frac{1}{\frac{t}{\varepsilon_0 \varepsilon_{Si_3N_4} wl} + \frac{d}{\varepsilon_0 \varepsilon_{air} wl}} = \frac{\varepsilon_{Si_3N_4} \varepsilon_{air} \varepsilon_0 A}{\varepsilon_{Si_3N_4} gap + \varepsilon_{air} t} \quad (42)$$

will include the air gap and the dielectric material thickness (t) and relative permittivity (air or Si_3N_4). Including this dielectric effect into the actuation modeling, increases the

المنارة للاستشارات
www.manaraa.com

required pull-in voltage for the cantilevers. For multiple cantilever beams, the solution becomes even more complex. The use of computer simulations helps determine the capacitance of multi-cantilever designs to reduce differences between the experimental values and those in the analytical solutions.

2.2.3.3. Cantilever thickness variation

Figure 15 shows the force applied in a downward direction. The force and moment of inertia of the cantilever along with the dimensions effect the operation of the cantilever. The mechanical spring constant for this cantilever is provided by Equation (41). The length and thickness control the amount of force necessary to deflect the cantilever. However, the thickness is the dominate factor for determining the spring constant, mechanical restoring force, deflection and pull-in voltage. Using the spring constant, the thickness is raised to a third power which effects all aspects of the cantilever actuation response.

2.2.3.4. Anchor Moment

The final factor effecting electrostatic actuation of the cantilever considers the anchor response to electrostatic actuation. By applying a force to create a moment at the anchor, the cantilevers deflection changes due to the electrostatic actuation. In general, the anchor in the fixed-free beam is considered an immovable object. . This first order approximation works well for describing beam deflection. However, for anchors on cantilevers with a high aspect ratio of the anchor pad to height of the anchor, the deflection generates a higher order effect based on the shifting anchor. Figure 17 shows a diagram of the potential change that can occur at the anchor due to the flexible anchor.

المنارة للاستشارات
www.manaraa.com

Solutions to ensure the stability of the anchor are the large anchor pads, low height aspect ratio, and maintain a cantilever thickness that does not require a large force to generate a deflection. In the design, the anchor consists of a large area on the double split ring resonators with a small height and factors out this effect.

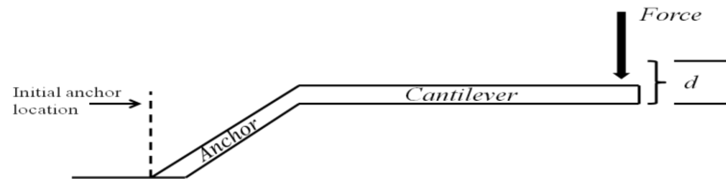

Figure 17. Cantilever anchor deflecting due to an applied force

2.3. Summary

An overview of the theory which began with Veselago's initial analytical work on negative refractive index which leads to metamaterials was presented. Effective parameters were described to understand the characteristics of anisotropic meta-atoms. Using the resonant frequency model, the meta-atom behavior was explained using lumped elements and equivalent circuit modeling. A retrieval process which uses experimental data was explained on how it can be useful to characterize the effective parameters. This background research leads to identifying parameters like inductance and capacitance that can help identify methods to integrate tunable elements into the meta-atom. And, provide understanding on how incorporating active materials in the meta-atom will help compensate for loss at the resonant frequency

To incorporate the tunable components, MEMS was discussed as a potential device for building the tunable elements into RF meta-atoms which are based on variable capacitance, inductance and electrostatic actuation. Chapter III presents the RF meta-atoms that incorporate tunable elements and active materials.

المنارة للاستشارات
www.manaraa.com

III. RF Metamaterial Structures

3.1. Fixed Meta-atoms for Metamaterial Structures

Metamaterials research covers the electromagnetic spectrum from acoustics to optical frequencies. At the various frequencies, the structures are arranged in patterns that generate a resonant frequency. For this research, the focus is on RF metamaterial structures. The metamaterial dimensions at different wavelengths is provided in Figure 18 which shows split ring resonators at RF and Terahertz frequencies and fishnet structures at the optical frequencies.

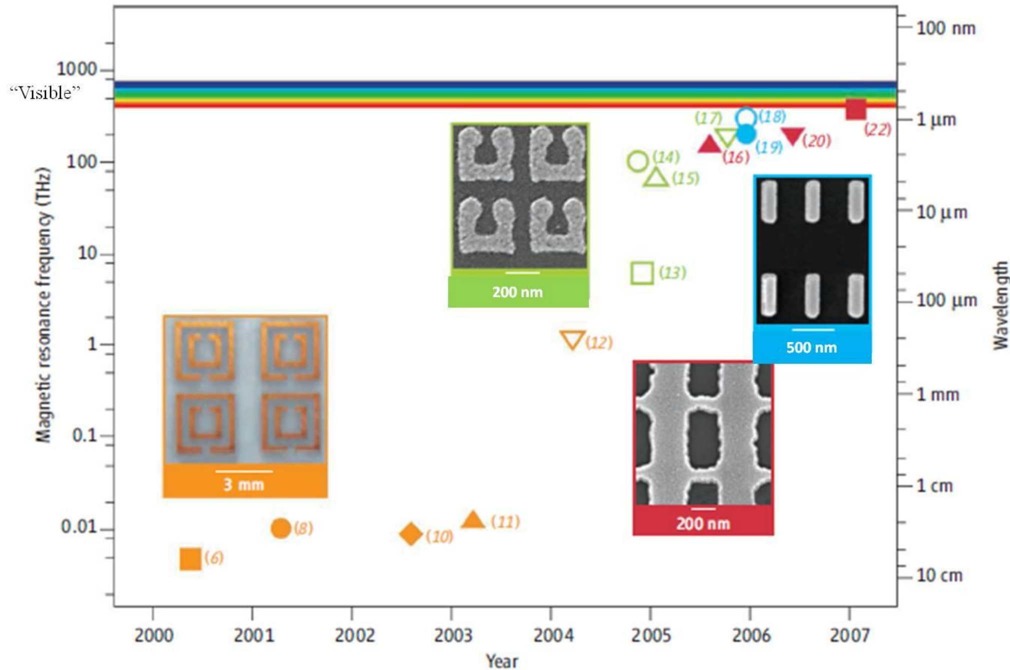

Figure 18. Advances in metamaterials. The solid symbols denote $n < 0$; the open symbols denote $\mu < 0$. Orange: data from structures based on the double split-ring resonator (SRR); green: data from U-shaped SRRs; blue data from pairs of metallic nanorods; red: data from the fishnet structure. The four insets give pictures of fabricated structures in different frequency regions [56].

In the RF part of the spectrum, most meta-atoms are composed of split ring resonators which make up the individual elements for RF metamaterial designs. The

المنارة للاستشارات
www.manaraa.com

meta-atom sizes range from micrometer to millimeter which depend on the expected resonant frequency. At RF, the meta-atom size allows flexibility for several design iterations to help understand the behavior of these structures and theorize on methods to adapt tuning methods for shifting the resonance frequency.

The baseline meta-atom was carried through the modeling, fabrication and testing phases to verify the design process. Two baseline meta-atoms were completed for design verification one at the 10 – 15 GHz range and one at 1 – 4 GHz range. Using the baseline meta-atom as a reference, the structural design can be defined to determine the inductance and capacitance parameters inherent in the structure used to establish a resonant frequency. Figure 19 shows the baseline structure that creates a resonance at 2.8 GHz. The split ring resonator loops interact primarily with the corresponding magnetic field to produce an effective permeability. The metal rods interact primarily with the electric field oriented along their length to produce an effective permittivity. The unit cell of the meta-atom includes rods from which an electromagnetic field is induced which behave as low frequency plasma [2]. The rods are also used to actuate the tuning elements. The baseline meta-atoms are arranged in a periodic array of four unit cells for testing of the structure which established a baseline for our modified designs.

Using the baseline design of a double split ring resonator meta-atom, several modifications are made to change the structure and observe the effects on the resonant frequency. The modifications are based on: 1) varying the capacitance using MEMS devices, 2) varying the inductance with design modifications and 3) adding a gain element to compensate for loss.

المنارة للاستشارات
www.manaraa.com

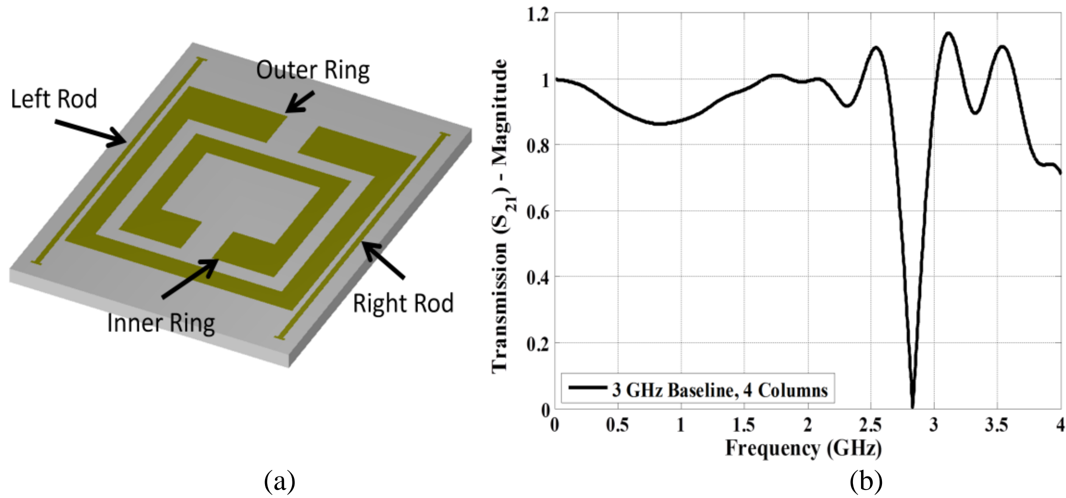

Figure 19 (a) Diagram of the baseline SRR with additional rods. (b) RF Transmission measurement showing resonance at 2.8 GHz with SRR inserted in RF strip-line.

3.2. Capacitive Tunable Meta-atoms

The meta-atoms are integrated with electrostatically actuated MEMS cantilevers to change the effective resonant frequency based on shifting the capacitance. The designs are arranged to investigate two conditions. First, the effect capacitance has on the designs at two different RF frequencies (10 – 15 GHz and 1 – 4 GHz). Second, modified designs are implemented to look at the effect of capacitance change within the gap and between the rings of the double split ring design.

3.2.1. 10 – 15 GHz Gap capacitive tuning meta-atom design

The baseline meta-atom was modified to meet the design requirements for electrostatic cantilevers. At 10 – 15 GHz, the meta-atom is defined with the following dimensions [57]. The outer SRR had a height of 2400 μm and a width of 2200 μm. The metal trace width is 200 μm for both the inner and outer SRR, except for the sides containing the gap which was expanded to 400 μm to accommodate the cantilever array. The inner/outer ring separation is 150 μm and the gap separation begins at 280 μm. The

www.manaraa.com

gap separation decreases in a stair step fashion to create identical overlapping areas for each of the varying length beams. The gap is decreased by 25 µm for an overall decrease of 100 µm for the shortest beam. This design feature ensures that each beam will contribute the same amount to the overall capacitance as it actuates. Figure 20 shows the double SRR unit cell with modifications to the gap regions to accommodate the cantilever array.

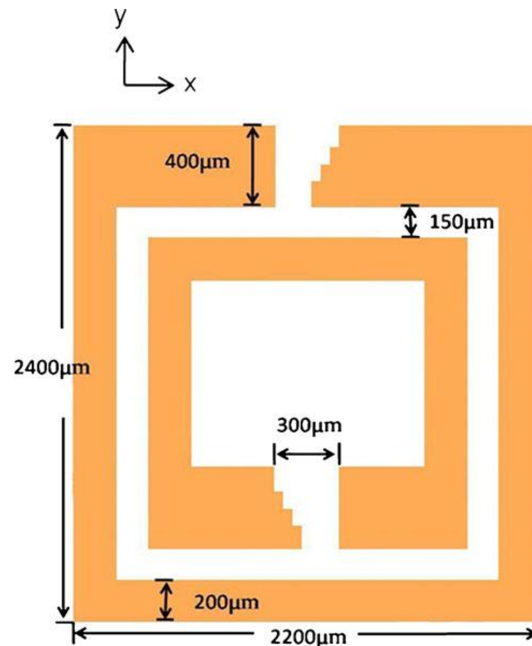

Figure 20. SRR unit cell schematic showing modifications to the gap region to accommodate the cantilever array.

The cantilever array was designed to produce a continuous transition of the resonance frequency as the beams were actuated or pulled-in. To achieve a steady increase in capacitance, the SRR gap region was altered to create identical landing pads for each cantilever. The cantilever dimensions were chosen so that upon actuation approximately two picofarads (pF) were added to the overall capacitance of the structure. The cantilever array was also designed to actuate at low voltages. To ensure the low

المنارة للاستشارات
www.manaraa.com

voltage requirement, the cantilever dimensions and dielectric were chosen so that the actuation voltage will be less than 100 VDC. Figure 21 is a layout view of the 10 – 15 GHz meta-atom showing the location of the cantilevers, and voltage control lines [57] - [59].

The cantilever array consists of five beams separated by 10 μm that are 75 μm wide and have lengths of 300, 325, 350, 375, and 400 μm. For each cantilever, the thickness is expected to be 4.75 μm based on analytical modeling and simulation results to maintain the low actuation voltage requirement. Each cantilever is fixed to one side of the SRR gap and overlaps the other end of the SRR by 120 μm. The initial gap height of the cantilever is 2 μm. Beneath the cantilever is a separate drive electrode that is 120 μm by 75 μm. The electrode is 10 μm away from the edge of the SRR. All the electrodes in the array are electrically connected so that one voltage source can actuate all the beams.

To achieve the desired added capacitance, the landing area of the SRR is coated in a dielectric. Silicon nitride (Si_3N_4) was chosen as the dielectric due to its high relative dielectric constant (6 – 9) [46]. The Si_3N_4 was deposited using plasma enhanced chemical vapor deposition (PECVD). The dielectric strength of PECVD silicon nitride is 5 MV/cm which corresponds to a breakdown voltage of 150 V for a 3000 Å-thick film [46], which is well above the range required to pull-in the cantilevers. PECVD deposited films often exhibit “pin holes” which reduce the breakdown voltage however, not significantly enough to inhibit the actuation.

The capacitance, pull-in voltage and resonant frequency calculations are provided in the analytical and simulation sections located in Chapter IV of this dissertation.

www.manaraa.com

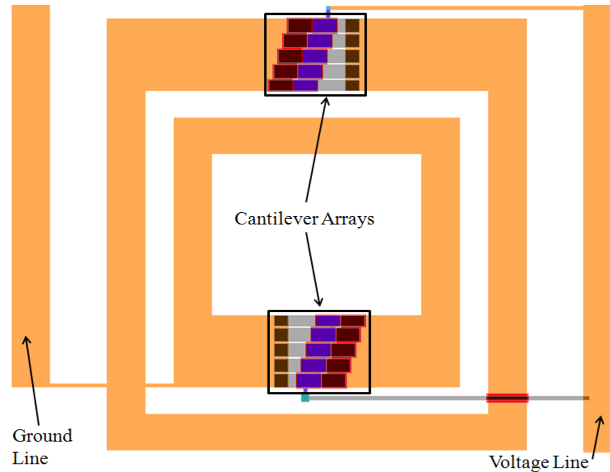

Figure 21. Layout showing cantilevers in the 10 – 15 GHz meta-atom design [57].

3.2.2. 1 – 4 GHz Gap based design

The 1 – 4 GHz design is similar to the design developed for 10 – 15 GHz testing. Reasons for integrating to a 1 – 4 GHz design are to allow for scaling of the meta-atom, integrating larger MEMS components and allowing greater flexibility for design changes. The larger scale for the designs allowed the investigation for capacitance effects based on locating cantilevers at the SRR gap, and intra-ring location between the double rings.

The first design layout at 1 – 4 GHz is a scaled up version for the 10 – 15 GHz design which integrates cantilevers into the gaps of both the inner and outer SRRs. The cantilever array consists of five cantilevers 300 µm wide that vary in length. The length of each cantilever varies by 50 µm to have cantilevers ranging from 300 to 500 µm. Each beam extends over the gap to the opposite side of the SRR overlapping the SRR by 75 µm. Each cantilever is isolated from the SRR by a 0.3 µm layer of silicon nitride and a gap with a height of 2.0 µm. Figure 22 is the layout view with the dimensions for the overall meta-atom design placed on an insulating quartz substrate. The quartz substrate was chosen for isolating the meta-atoms and ease of fabrication processing constraints.

المنارة للاستشارات
www.manaraa.com

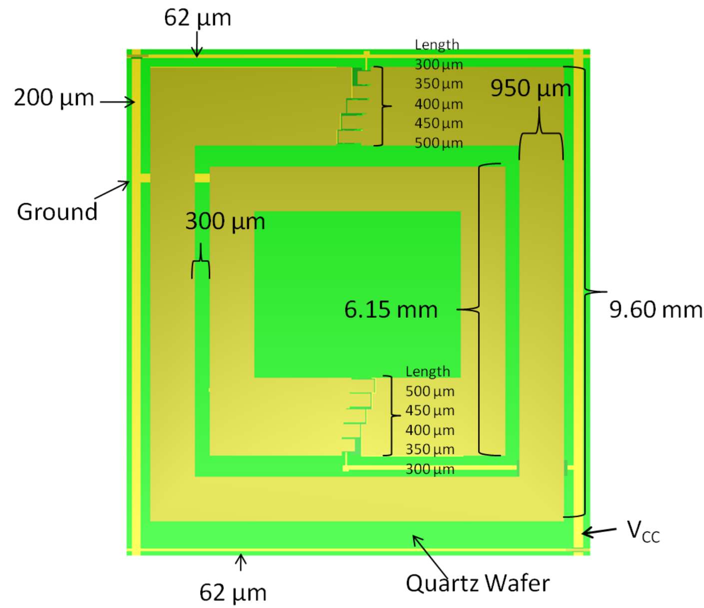

Figure 22. Layout for the 1 – 4 GHz Gap based meta-atom design.

3.2.3. 1 – 4 GHz Intra-ring Meta-atom Designs

Three designs modifications were decided on to layout and fabricate as meta-atoms. Each design helps to look at how capacitance changes affect the resonance frequency when cantilevers are incorporated into the double split ring resonators. The first intra-ring design incorporates cantilevers sets between the inner and outer split ring resonators by having four cantilevers make up a set of variable capacitors (varactors) for the design. There are two sets of cantilever arrays located on the adjacent sides of the SRR from the gap. For the design, the cantilever arrays consist of four beams each 300 µm wide, whose length varies from 350 to 500 µm in 50 µm steps. The cantilevers extend from the inner SRR across the gap to the outer SRR, overlapping it by 75 µm. The actuation pads are placed between the rings at locations to vary the pull-in voltage. The longest beams on all four arrays should pull-in at the same voltage, thus creating four shifts in the resonant frequency.

www.manaraa.com

The second intra-ring design incorporates cantilevers in the SRR gaps as well as between the SRRs. The cantilever arrays in this design have the same dimensions as those of the meta-atom with cantilever in the SRR gaps and the meta-atom with intra-ring cantilevers. The overall intention of this design is to increase the range in which the resonance frequency shifts by incorporating more cantilevers for a larger increase in the capacitance. With all the cantilevers at the same length having the same pull-in voltage, the design has a larger shift in resonance per cantilever.

The third intra-ring design has three arrays consisting of four cantilevers placed between the SRRs. The widths of each cantilever array are varied to change the capacitance area of each array. One set of the cantilevers has a width of 300 μm while the other cantilevers sets are 400 and 500 μm wide, respectively. Increasing the area creates a broader change in capacitance than the other designs.

Developing the intra-ring structures from the baseline meta-atom design presented some design challenges. For instance, the actuation pads and interconnects add unnecessary capacitance and inductance which shifts the resonant frequency. To alleviate this problem, interconnects are scaled to smaller sizes to minimize the additional capacitance and/or mutual inductance.

In the intra-ring meta-atom designs, the metal components are fabricated with gold to improve: conductivity, ease of micro fabrication, and prevent oxidation of the material. A quartz substrate was used as a base for the metal components to increase electrical isolation since quartz is a non-conducting material [60]. All three designs were fabricated based on the two modification options (intra-ring and between the gap) in

المنارة للاستشارات
www.manaraa.com

order to test the effect of integrating MEMS cantilevers into the SRR structure and determine the configuration that offered the widest tunable range [61].

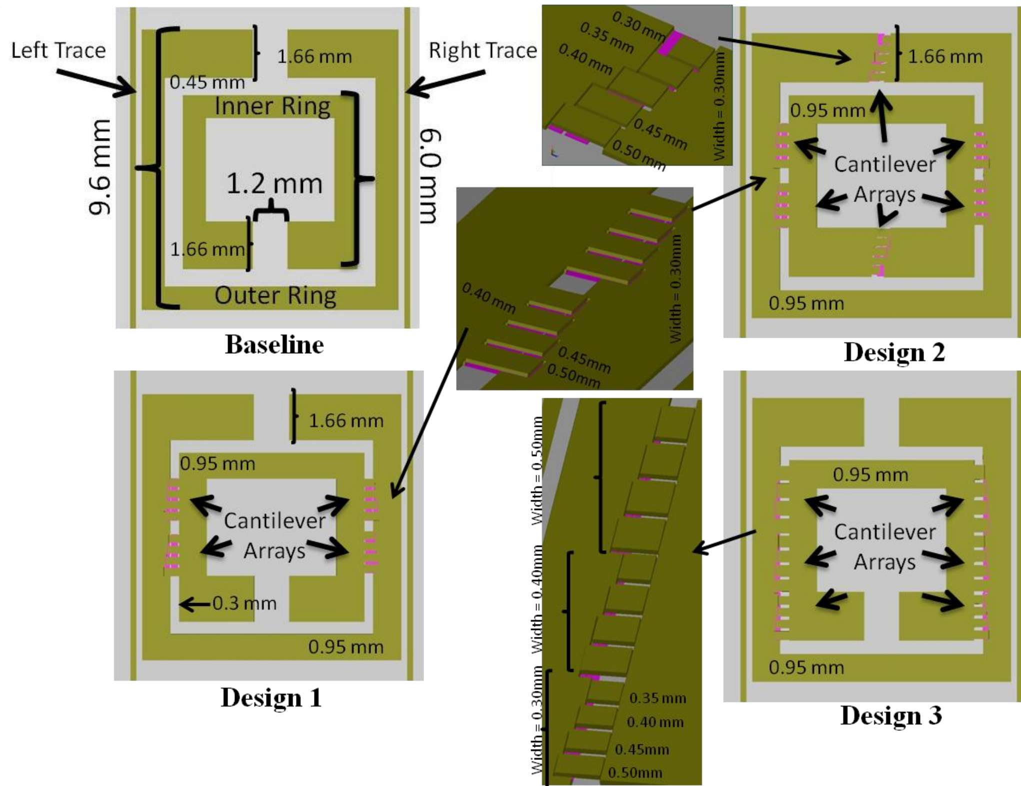

Figure 23. Layout of the three intra-ring meta-atom design variations integrated with (Design 1) cantilevers between rings, (Design 2) cantilevers in the gap and connecting the rings, and (Design 3) cantilevers with varying widths between the rings.

3.3. 1 – 4 GHz Inductance based Meta-atom Designs

Based on Equation (15), the simplest resonant frequency analytical model involves inductance as well as capacitance from structures. This section introduces meta-atoms which vary the overall inductance while at the same time minimize capacitance change based on the design. The section covers designs for static inductive meta-atoms.

Based on the 1 – 4 GHz baseline meta-atom, structural modifications were made to increase the amount of inductance with minimal changes in the structure's capacitance.

المنارة للاستشارات
www.manaraa.com

Two meta-atoms were designed which altered the outer SRR to increase the total inductance.

To modify the 1 – 4 GHz baseline meta-atom with minimum capacitance change, the outer SRR was changed with a 0.15 mm gap in the middle of the vertical sides. Loops were added to the outer SRR which increased the overall length of the outer SRR. The increased length produced a change in the induction based on the increased path for current flow. From the baseline design, two modifications are implemented with each meta-atom design increasing the length of the loop which in turn increased inductance of the outer SRR.

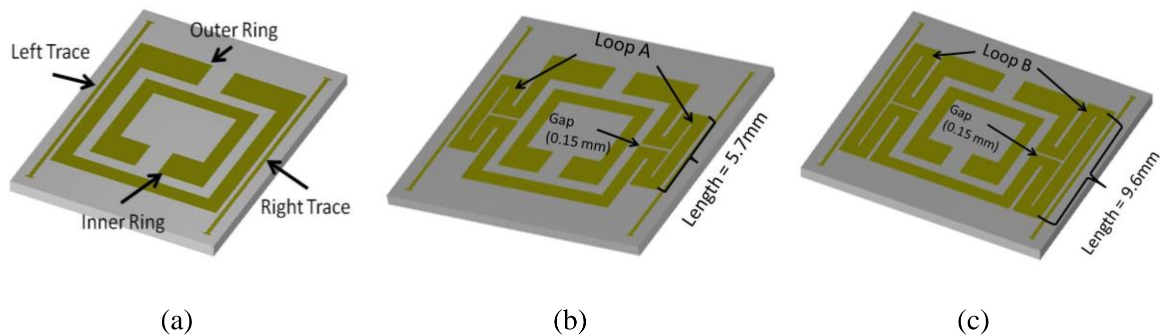

(a) (b) (c)

Figure 24. Layouts of the meta-atoms (a) baseline, (b) Loop A with loop extending up and down the outer SRR's vertical side and (c) Loop B with the loop equal to the outer SRR's vertical side.

On all the meta-atoms for inductance variation, the periodic distance between meta-atoms remains constant on the substrate and between arrays inserted in the RF strip-line. And the 0.15 mm gap in the vertical sides of the outer SRR is maintained on both modifications to connect the loops of the various designs. The designs were laid out using L-Edit. After laying out the designs, a computer simulation of each design is accomplished using CoventorWare ® to determine the self-inductance and capacitance of each ring and trace.

المنارة للاستشارات
www.manaraa.com

3.4. 1 – 4 GHz Active Element based Meta-atom Design

Based on the previous capacitive and inductive design approaches, the meta-atom lends itself to another design concept which is implementing a meta-atom with an active element. The active element consists of a gain medium such as a transistor or a low noise amplifier (LNA) which is needed to overcome resonant null loss. The concept behind the integration is to have the ability to control current flow around the SRR. Incorporating the low noise amplifier into the baseline meta-atom involves creating a gap in the outer split ring resonator and connecting the input and output of the amplifier to either side of the gap. With this design, the original gap is preserved and can still be used for tuning. The current flow for the outer split ring resonator goes from the split ring resonator gap around the ring to the input of the amplifier. The current flow then proceeds out of the amplifier and continues around the split ring resonator to stop at the opposite side of the gap. The gap of the split ring resonator functions as a charged capacitor generating the electromagnetic field that provides a built up charge on the split ring resonator. The low noise amplifier controls the amount of charge build-up through the split ring which in turns controls the level of the resonant null of the meta-atom.

For the research into the active element, a 0.5 – 6.0 GHz Low Noise Gallium Arsenide (GaAs) MMIC Amplifier (LNA) was chosen as the gain medium integrated into the outer SRR based on the operating rang of the LNA and matching to the meta-atom. [62]. The 1 – 4 GHz baseline meta-atom design was chosen to integrate the active element because of the size, ease of device integration and availability of impedance matched LNA operating at the 1 – 6 GHz (S-Band) frequency range. The equivalent circuit for the LNA uses pHEMT technology with self-biasing current sources, a source-

المنارة للاستشارات
www.manaraa.com

follower inter-stage, resistive feedback, and on-chip impedance matching networks. The normal operating voltage range of the amplifier is 0 – 7 VDC and generated 18 – 20 dB of gain at ~4 GHz. Incorporating the low noise amplifier into the baseline meta-atom involves creating a 0.40 mm gap in the outer split ring resonator and connecting the RF input and output of the amplifier at the gap. The current flow for the outer split ring resonator travels from the large split ring resonator gap around the ring to the RF input of the amplifier. The current flow then proceeds out of the amplifier and continues around the split ring resonator stopping at the opposite side of the large gap. The large gap of the split ring resonator functions as a charged capacitor generating the electromagnetic field that provides a charge built up on the split ring resonator. The low noise amplifier controls the amount of free flowing electrons traveling through the split ring resonator which in turn controls the resonant null level of the meta-atom by counteracting any loss.

To build and integrate the meta-atom, prototypes were drawn up with a printed circuit board (PCB) layout editor. The layout consists of the 1 – 4 GHz baseline meta-atom along with landing pads for the LNA surface mount devices, and interconnects for DC bias and ground. A 0.40 mm gap is cut out of the outer SRR to integrate the LNA and interconnects. The DC bias and ground interconnect traces are located on the backside of the layout and connected with thru-vias to the topside for the LNA. The design layouts are inspected and sent for fabrication on double sided printed circuit board (PCB) made of insulating glass reinforced epoxy resin (FR4) at a commercial foundry [63].

المنارة للاستشارات
www.manaraa.com

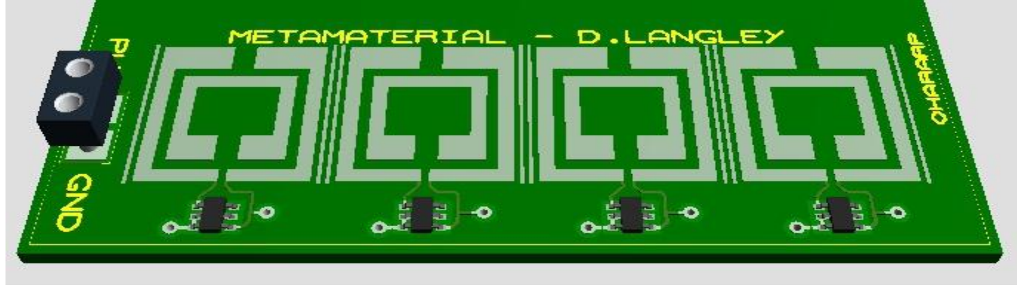

Figure 25. Active element integrated into the 1 – 4 GHz meta-atom. The GaAs low noise amplifier integrated into the baseline meta-atom is used to effect the resonant frequency based on a gain medium inserted into the SRR.

3.5. Summary

Variations on RF meta-atom designs were presented. The Baseline meta-atom and modifications to the structure were discussed to implement tunable resonant frequency and compensate for loss. The modifications incorporate electrostatic cantilevers, inductive loops and active elements. Based on the modifications, new concepts will be discussed in the future research section that can be experimentally investigated as future work. These new concepts are inductive tuning with phase change material and investigating metamaterials with two dimensional (2-D) focus beam system.

المنارة للاستشارات
www.manaraa.com

IV. RF Meta-atom Modeling and Simulation

4.1. Analytical Modeling

This section cover the analytical modeling completed on the meta-atom designs to compare with simulation and experimental results. The section also covers analytical modeling completed on the cantilever which will be used in tunable meta-atom designs.

4.1.1. Meta-atom Analytical Modeling

Analytical modeling for RF meta-atoms used to calculate the resonant frequency helps define the effective permeability parameter. The approach used to define the parameters for meta-atoms begins by knowing at what specific frequency the resonance should occur. To help understand the analytical modeling, a resonance occurring between 1 – 4 GHz was chosen for the modeling approach to show how the modeling is used to derive a solution for the baseline design. From the design described in section 3.1, the analytical modeling begins with defining the capacitance and then the inductance based on type of metal, and dimensions for the split ring resonator as shown in Figure 26.

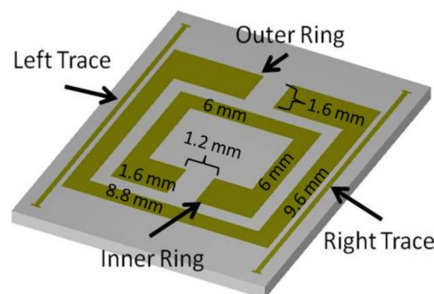

Figure 26. Meta-atom showing dimensions used to calculate the capacitance and inductance values.

The capacitance can be described by the parallel plate capacitance model

المنارة للاستشارات
www.manaraa.com

$$C = \varepsilon_0 \varepsilon_r \frac{wl}{g_0} \quad (43)$$

as described in the background section on lumped elements under capacitance. To define the capacitance, the meta-atom is divided into four sections that represent the total capacitance in the design. Figure 27 shows how the design is diced into sections to obtain the capacitance. Section A determines the capacitance of the sides away from the gap in the split ring resonator. Section B determines the capacitance by calculating the capacitance at the gap of the outer split ring resonator and the section of the inner ring adjacent to the outer ring's gap. Section C determines the capacitance by calculating the capacitance at the gap of the inner split ring resonator and the section of the outer ring adjacent to the inner ring's gap.

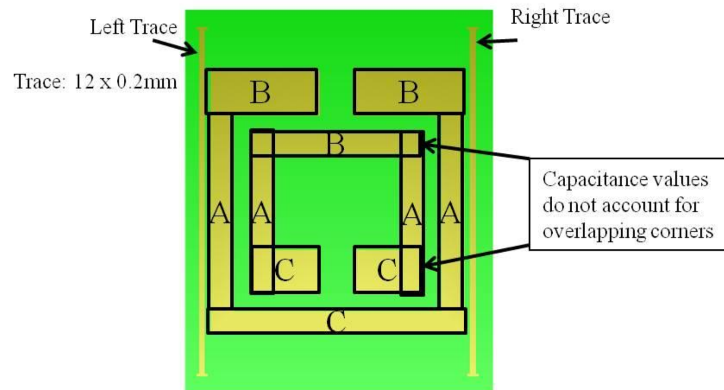

Figure 27. The 1 – 4 GHz Meta-atom showing sections for capacitance calculations.

Using the parallel plate capacitance model, the g_0 represents the open area in the split ring resonator gaps, between the rings or traces. The split ring resonator width (w) at the gap is used in the model because it is the location where the electric field builds up the charge to send current around the ring. The length (l) is based the length of the ring after accounting for the gap and width. For the analytical model, the lengths for the outer

المنارة للاستشارات
www.manaraa.com

and inner rings are 27.6 mm and 16.4 mm, respectively. For the 1 – 4 GHz baseline meta-atom, the dimensions are provided in Figure 26. Based on the dimensions and the relative permittivity for air (1.0), the capacitance for each section is determined based on the structural dimensions. For section A, the vertical sides of the outer and inner rings are used as the overlapping areas. The outer ring vertical side has the length and width equal to 7.2mm and 0.8mm, respectively. The inner ring vertical side has the length and width equal to 3.6 mm and 0.8mm, respectively. The gap between the outer and inner ring is 0.6 mm. The capacitance for section A equals 0.128 pF. For section B, the gap in the outer split ring resonator creates a capacitance value along with the capacitance observed by the side of the inner split ring resonator. Both of these capacitances make up a series combination for section B. The outer split ring resonator capacitance at the gap equals 0.09 pF, while the inner split ring contributes capacitance equal to 0.071 pF. For section C, a series capacitance occurs similar to section B. The inner split ring resonator capacitance at the gap equals 0.057 pF and the outer split ring contributes capacitance equal to 0.104pF. The metal trace capacitance calculated to a total of 0.106 pF. Combining all the capacitance values into a total provides a 0.384 pF for the meta-atom.

The inductance is based on the knowing the metal type, and structural dimensions. Using the simplified equation for infinitely thin conductors which was described in a earlier section but provided by the following model, the inductance for the outer and inner ring can be solved analytically.

المنارة للاستشارات
www.manaraa.com

$$\frac{L_{P_{ii}}}{l} = \frac{\mu}{6\pi}\left\{3\ln[u+(u^2+1)^{\frac{1}{2}}]+u^2+u^{-1}+3u\ln[\frac{1}{u}+(\frac{1}{u^2}+1)^{\frac{1}{2}}]-[u^{\frac{4}{3}}+(\frac{1}{u})^{\frac{2}{3}}]^{\frac{3}{2}}\right\} \quad (44)$$

Providing the dimensions and relative permeability for copper ($\mu = 0.999994\ \mu_0$), the outer split ring resonator inductance is calculated using the length of 27.6 mm and width of 0.8 mm. The inner split ring resonator inductance is calculated using the length of 16.4 mm and width of 0.8 mm. Based on the model, the outer and inner split ring resonator inductance are 26.19 and 13.87 nanohenry (nH), respectively.

After obtaining the capacitance and inductance for the outer and inner split ring resonators, the resonant frequency can be solved and used in analytical models to solve the effective permeability and permittivity. At RF, the resonant frequency analytical model

$$f_{res} = \frac{1}{2\pi\sqrt{LC}} \quad (45)$$

uses the parallel inductance and total capacitance for the meta-atom design. Based on the capacitance and inductance values obtained for the 1 – 4 GHz baseline design, the resonant frequency is 2.70 GHz. This value does not take into account the capacitance produced by the vertical traces and the inner ring in the meta-atom design which will be solved during the simulation of the design. It does give a relative idea of the resonant frequency but a comparison must be made between the analytical model, the simulation and experimental testing.

المنارة للاستشارات
www.manaraa.com

4.1.2. Cantilever Analytical Modeling

Building on the contributions made in the background section of electrostatic actuation, the cantilever has design parameters that must be considered for modeling and experimental analysis. The parameters include force, mechanical spring constant, pull-in voltage, and capacitance. For these parameters, the cantilever model must be thoroughly examined to understand what is expected during actuation.

The force based on spring constant variation changes with the cantilever dimensions. The cantilever thickness changes the force necessary to deflect the cantilever. Using Hooke's Law, the force versus thickness is plotted to show the dependence of force on the thickness of the cantilever. The cantilever length is kept constant at 0.30 mm. The Young's modulus of gold (78 GPa) is used in the modeling.

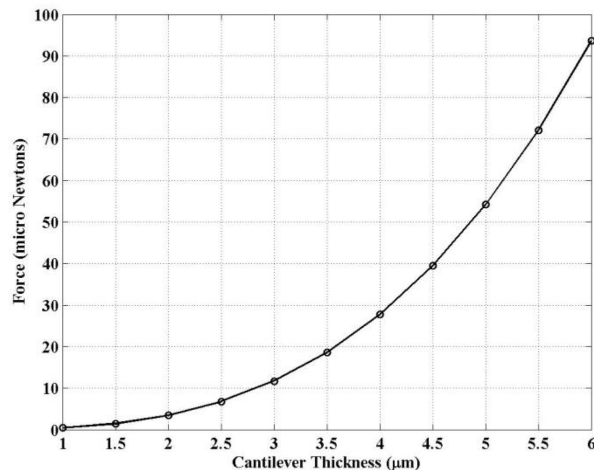

Figure 28. Cantilever deflection force versus cantilever thickness.

The cantilever pull-in voltage is a parameter that relies on the dimensions of the cantilever and the capacitance due to the electrostatic actuation. In the section on electrostatic actuation, three variables that change the level of pull-in voltage were discussed. The simple cantilever model is compared to the model when dielectric

www.manaraa.com

material and fringing effects are taken into consideration. The models discussed in the background section on electrostatic actuation are plotted in Figure 29 to show the differences in pull-in voltage as a function of cantilever length and capacitance model. The cantilever thickness and width are kept constant at 5 μm and 300 μm, respectively.

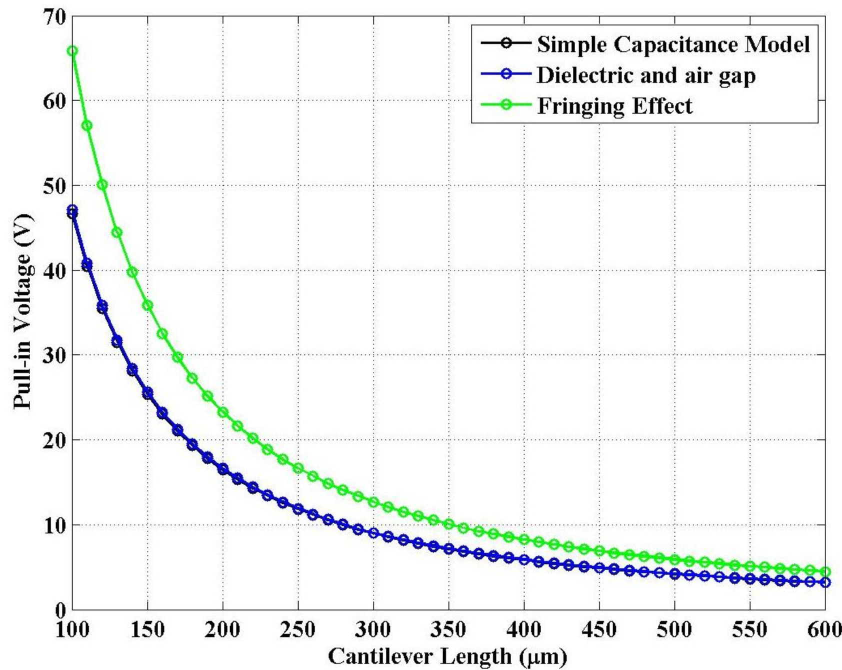

Figure 29. Cantilever pull-in voltage as a function of length and capacitance model. The fringing effect on the capacitance model shows the largest deviation from the simple model. The simple model and model with the dielectric layer show a similar pattern.

The capacitance changes as a function of these higher order variables and shifts the pull-in voltage required to deflect the cantilever. The fringing model shows the highest deviation from the simple capacitance model. In the designs, the cantilevers will overlap the actuation pads which have smaller surface area. The fringing capacitance model will be used to set design specifications. The fringing capacitance model will be compared with simulation and experimental values to check for deviations in expected values.

المنارة للاستشارات
www.manaraa.com

Four different modifications were considered based on two options to build and test the effect of integrating cantilevers into the SRR. For example, the first 1 – 4 GHz based design integrates cantilevers into the gap of the resonator rings. Five cantilevers of varying length were placed into the gap. Each cantilever has a width of 300 μm; however, the length of each cantilever varies by 50 μm to have beam lengths changing from 300 to 500 μm. The actuation pad under each cantilever is shifted to allow for varying pull-in voltages which are calculated with

$$V_{pi} = \frac{2x_0}{3}\sqrt{\frac{k_m}{1.5C_0}} \tag{46}$$

where x_0 is the initial gap, k_m is the spring constant and C_0 is the capacitance between the cantilever and actuation pad at the gap [60]. For the SRR, each cantilever contributes a change in the capacitance based on the area that overlaps the gap on the SRR, an area of 300 μm by 75 μm. The beam extends over the gap to the opposite side of the SRR. The cantilever height is 2.0 μm. The cantilever is isolated from the SRR by a layer of silicon nitride with a thickness of 0.3 μm. When the each beam is pulled in, it contributes approximately 0.6 pF to the overall capacitance.

4.2. Meta-atom Equivalent Circuit Modeling

The 1 – 4 GHz Baseline Meta-atom is used as the design to describe how to build the equivalent circuit model. In this sub-section, the lesson learned from the background research on the meta-atom and the analytical modeling will be combined to help build the equivalent circuit model that can help characterize the design at RF. The initial model used in the background section was a series resonant bandstop filter. It has a single resonant null at a given frequency. This is similar to experimental results carried out on

المنارة للاستشارات
www.manaraa.com

the baseline 1 – 4 GHz Meta-atom. However, the series resonant bandstop filter accounts for one capacitor and one inductor. In order to characterize the meta-atom, the equivalent circuit model has to consider the affect of all the meta-atom's subcomponents which are the split ring resonators, and metal traces. Based on the analytical modeling, the capacitance can be calculated for sections of the meta-atom and combined into one lumped element. A better representation will be to consider the sections as capacitor elements which combine into one branch in the model. The series resonant bandstop filter used to represent the meta-atom based on the capacitive sections is shown Figure 30. It includes the capacitors and inductors for the meta-atom. The capacitors in the circuit are equivalent to each section based on the surface charge between the metal components. Inductance values for the meta-atom come from the self-inductance of the split ring resonators. In the analytical section, the inductance was calculated for the inner and outer split ring. These values are combined in the equivalent circuit model as parallel lumped inductor elements.

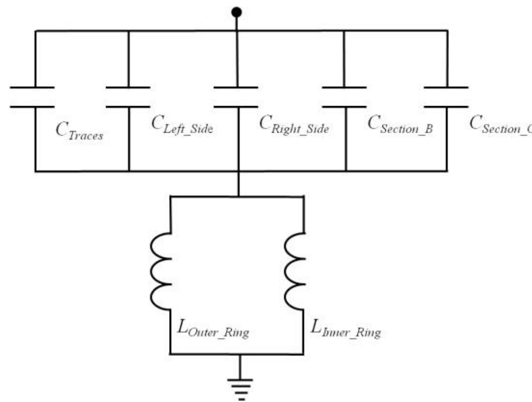

Figure 30. Meta-atom equivalent circuit model.

Simulink is used to simulate the meta-atom equivalent circuit. The capacitance and inductance values obtained in the analytical section were used in the simulation. The

المنارة للاستشارات
www.manaraa.com

response from the circuit is shown in Figure 31. The resonant null appears at the calculated frequency. Based on the response and analytical calculations, the meta-atom equivalent circuit developed for the sections provides an accurate representation for the design.

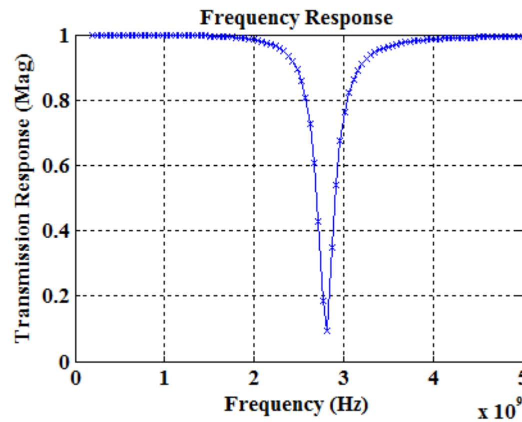

Figure 31. Meta-atom equivalent circuit frequency response

4.3. RF Simulations

Simulations for the RF meta-atom designs were completed using two simulation programs. The programs are used to compare the capacitance, inductance and resonant frequency values generated by the simulations. The first program is CoventorWare ® which generates the capacitance and inductance values. The second program is CST Microwave studio ® which simulated the condition of RF energy impinging onto the meta-atoms.

4.3.1. CoventorWare ® Modeling

To demonstrate the tuning capacitance, CoventorWare ® is used to simulate the designs determining the capacitance, inductance, and cantilever actuation values [64]. For the simulation, the meta-atoms designs are constructed with finite element models that

www.manaraa.com

sectionalize the designs into individual elements or blocks. Each element is a data point linked to all the surrounding elements composing the entire design. The element size and type in the model determines how accurate the finite element model can calculate the parameters. A mesh analysis is completed to determine the size of the elements necessary to build the models. The larger the element size, the faster the computation; however, the parameter value may be underestimated. Having a smaller element size slows the computation time and provides a more accurate the parameter value. A trade-off between the element size and parameter value is determined by completing the mesh analysis. Based on finite element modeling, the capacitance of each component against the other structural components is simulated and inserted into the resonant frequency equation. Using this method, the meta-atoms designs are simulated in two operational states to understand the effect of capacitance changes on the designs.

The first operational state is with all cantilevers located in the initial position having a 2 μm gap between the cantilever and the adjacent resonator ring coated with silicon nitride. With all the cantilevers in the initial state, the capacitance of the design is at the lowest value, which represents the highest resonator frequency achievable by the design. As the cantilevers are pulled-in, the capacitance increases which in-turn causes the resonant frequency to decrease leading to the second operational state. For the second operational state simulation, all cantilevers are located at the pull-in position. This state happens when the applied actuation voltage pulls all the cantilevers in contact with the silicon nitride on top of the actuation pad. This operational state represents the highest value capacitance position where the capacitance shifts the resonant frequency to its lowest value.

المنارة للاستشارات
www.manaraa.com

The electrostatic actuation is conducted with actuation pads which attract the cantilever using a voltage potential. By applying the voltage potential, the simulation reveals the experimental behavior of the cantilever integrated into the meta-atom design. The simulations show the cantilevers start to actuate at 26 VDC. Applying more actuation voltage, draws the cantilevers closer to the actuation pads until all the cantilevers come in contact with the dielectric layer on the actuation pad. Figure 32 shows the actuation of the cantilevers in the simulation at different voltage biasing conditions.

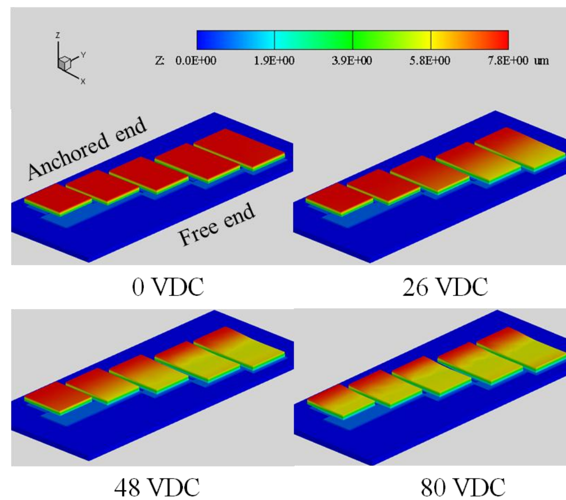

Figure 32. Cantilever actuation simulated with CoventorWare ® to determine the biasing voltage necessary to draw the cantilevers to the actuation pads.

4.3.1.1. 10 – 15 GHz Gap based Designs

The meta-atom design at 10 – 15 GHz is composed of the double split ring resonator design which was described in section 3.2.1. Rederus completed an initial investigation into the design that provided the initial research into MEMS incorporated into the split ring resonator meta-atom [57]. He developed a custom simulation process to construct the designs into a solid model. To simplify the model, the substrate and split rings were hidden during the modeling of the cantilever array to reduce simulation time

المنارة للاستشارات
www.manaraa.com

required for the design. Figure 33 shows the solid model of the cantilever meshed to perform the simulations.

Simulations carried out using CoventorWare ® provided estimates for pull-in voltage, capacitance, collapse voltage, and release voltages. Using the CoSolveEm analyzer tool, the cantilever was fixed at 0 V and the actuation electrode is simulated with applied voltages ranging from 0 to 130 VDC. As the voltage changes, the capacitance is measured for each cantilever. For the 300 µm cantilever, the capacitance changed from 0.083 pF at 0 VDC to 0.396 pF at 130 VDC which is the state when the free end of the cantilever contacts the dielectric on the opposite side of the split ring resonator gap. Based on his results, masks for the 10 – 15 GHz meta-atom design were produced to fabricate the design on insulating semiconductor substrates.

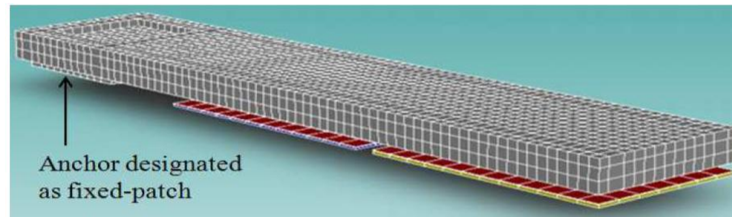

Figure 33. Meshed cantilever in CoventorWare ® used to calculate pull-in voltage, capacitance and release voltage [57].

4.3.1.2. 1 – 4 GHz Gap based Designs

The 1 – 4 GHz based designs are based on the meta-atoms discussed in section 3.2.2. The meta-atoms at the 1 – 4 GHz range provide flexibility in the meta-atom structure for the design and fabrication of tunable structures. Two designs were simulated to obtain the capacitance and inductance values based on scaling the meta-atom design. The Baseline design is the first scaled design to ensure the fundamental design performs as expected without further modifications. The Baseline design consists of the double

www.manaraa.com

split ring resonator meta-atom which is shown in Figure 34. The dimensions of the meta-atom are obtained using analytical modeling and then a device layout is completed based on the dimensions. CoventorWare ® is used to simulate the model using its FEM solvers for electrostatic and inductance values. The Baseline design is meshed to complete FEM analysis on the structure. Based on the simulation the values for the capacitance and inductance are collected on each SRR and the metal traces. The total capacitance value for the meta-atom which includes the outer and inner split ring resonators and metal traces capacitance is 0.384 pF. And the inductance values simulated for the outer and inner split ring resonators are 26.19 nH and 13.87 nH, respectively. Using the resonant frequency equation, the resonant frequency is 2.70 GHz, which equal to the analytical solution. Figure 35 shows the Baseline meta-atom meshed and prepared for CoventorWare ® simulations. For the simulation, the meta-atom is composed of gold rings and traces. The quartz substrate is not used during the simulation because electrical isolation is its main purpose.

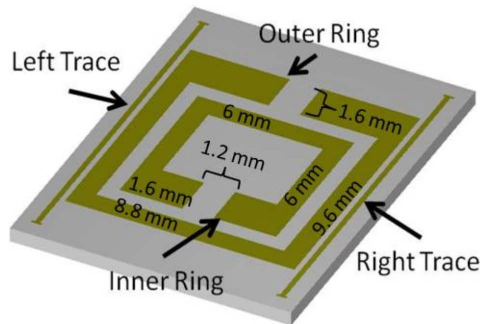

Figure 34. 1 – 4 GHz Baseline meta-atom design with dimensions used in analytical modeling and CoventorWare ® simulations.

www.manaraa.com

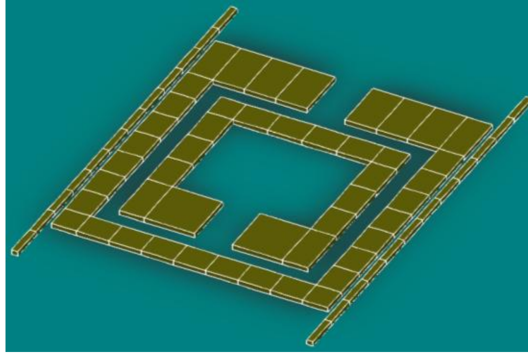

Figure 35. Baseline meta-atom meshed and prepared for CoventorWare ® simulations.

The second 1 – 4 GHz meta-atom design adds electrostatic cantilevers to the inner and outer split rings. The cantilevers are used to produce a tunable meta-atom design that allows the resonant frequency to shift based on the position of the cantilever's tip. Figure 22 shows the tunable meta-atom with dimensions for the cantilever added to the Baseline meta-atom. The design is imported in to CoventorWare ® for simulations. The MemElectro solver is used to determine the capacitance values of the design. The capacitance is solved for two operational states which are the initial operational state with cantilevers having a 2 μm gap and the final operational state with all the cantilevers pulled into contact with the dielectric layer. The inductance for the design is simulated using a block design because of issues using the 3-D design shown in Figure 36. Based on the simulated design, the total capacitance for the split ring resonators and the metal traces is 0.84 pF for the initial operational state. The total capacitance for the split ring resonators and metal traces is 0.94 pF for the final operational state. The capacitance values are used in the resonant frequency equation. The initial operational state resonant frequency is calculated to be 1.97 GHz. The final operational state resonant frequency is calculated to be 1.86 GHz.

المنارة للاستشارات
www.manaraa.com

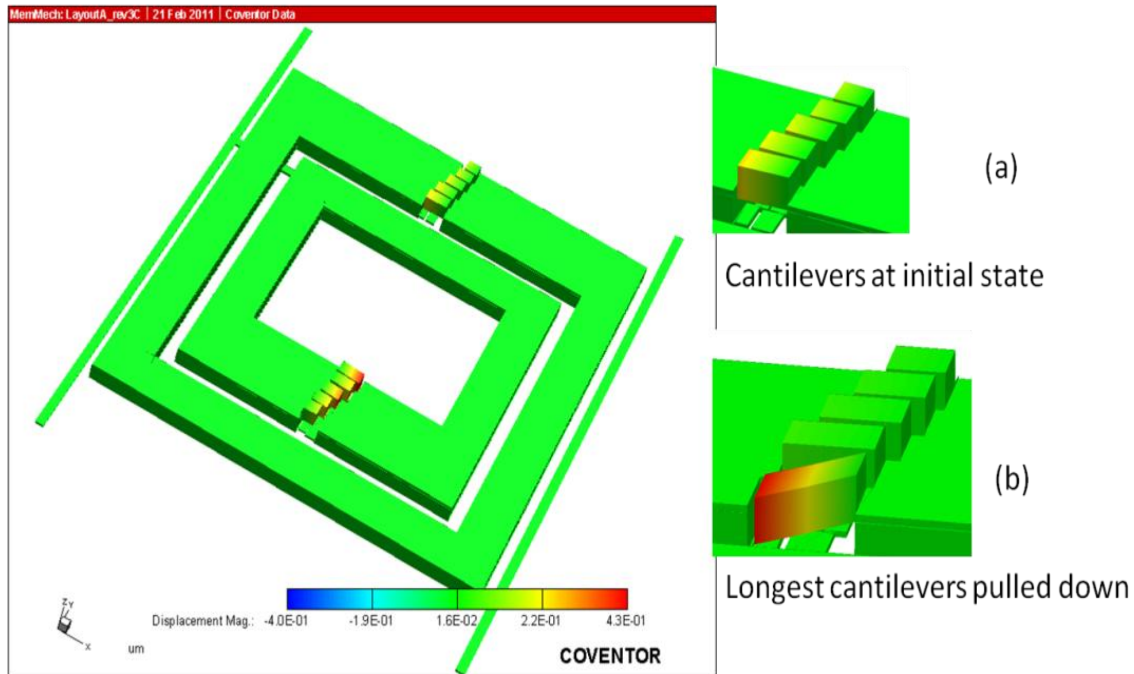

Figure 36. Meta-atom design modified with cantilevers for a tunable resonant frequency response.

4.3.1.3. 1 – 4 GHz Intra-Ring Designs

The intra-ring meta-atom designs are built with electrostatic cantilevers to examine different effects of placing cantilevers in different areas around the split ring resonators. The three designs are based on the structures discussed in section 3.3.3 and shown in Figure 23. Similar to other designs, these three designs are constructed using a layout editor and simulated with CoventorWare ®. With the simulation, the capacitance is captured at the initial and final operational states using a meshed FEM to determine the frequency range for experimental testing. The operational states are similar to the 1 – 4 GHz meta-atom design with cantilevers located in the split ring resonator gaps. Using all the simulated results compiled into Table 2 and Table 3, a simulation comparison is possible for the two operational states. From the simulation results, the resonant frequency was calculated to predict the expected results once the designs are fabricated.

المنارة للاستشارات
www.manaraa.com

As expected, the CoventorWare ® simulations show the capacitance increases as the cantilevers pull into contact with the actuation pads which in turn decreases the resonant frequency. Based on the simulated results, the meta-atom designs are fabricated to see how well the simulated and experimental results match.

Table 2. Simulated capacitance and induction parameters for the designs at initial operational state where the capacitance gap is 2 μm and no actuation voltage applied; along with the calculated resonant frequency for each design.

Design	L_{Outer} (nH)	L_{Inner} (nH)	Capacitance (pF)	ω_{res} (GHz)
Baseline	26.2	13.87	0.384	2.70
1	25	12	1.28	1.56
2	25	12	1.227	1.59
3	25	12	2.45	1.13

Table 3. Simulated capacitance and induction parameters for the designs at final operational state where the capacitance gap is closed and maximum actuation voltage applied; along with the calculated resonant frequency for each design.

Design	L_{Outer} (nH)	L_{Inner} (nH)	Capacitance (pF)	ω_{res} (GHz)
1	25	12	1.889	1.29
2	25	12	1.483	1.45
3	25	12	6.193	0.71

4.3.1.4. 1 – 4 GHz Inductance based Meta-atom Designs

Simulations for the inductive based meta-atom designs discussed on section 3.3.1 were carried out in CoventorWare ® to determine the capacitance and induction values of each design. Figure 24 shows the baseline design along with the two designs that change the induction value of the outer split ring while permitting only small changes to the capacitance values. The static designs are simulated in frequency range from 1 Megahertz (MHz) to 10 GHz to determine the capacitance and inductance of the design across a broad spectrum. To obtain inductance values, the simulated designs are biased with one

المنارة للاستشارات
www.manaraa.com

volt across the gaps of the inner and outer rings. The one volt bias stimulates a current flow through the rings similar to an induced current on the rings at the SRR capacitive gaps. Figure 37 shows the imaginary current density of each design simulated with CoventorWare ® used to solve for capacitance and inductance. As shown in the Figure 37, the magnitude of the imaginary current density increases relative to the increase in inductance for the inner split ring resonator. However, the magnitude of the imaginary current density decreases on the outer split ring resonator as the length of the loop increases.

It is critical for the inductance to remain relatively constant over a broad frequency range for stability of the design, as discussed by Grover [65]. The metal SRR structures are constructed with copper (FR4 PCB prototypes) or gold (microelectronic fabrication) to eliminate any unwanted inductance shifts as a function of the metal type or frequency. The range of operations is well below the plasma frequency of copper or gold where metals lose their complex refractive index form and become transparent. There is a slight shift in inductance as the frequency goes beyond 100 MHz due to a change in the uniform current density the across wires/conductors at higher frequencies [65]. This is due to the “skin effect” or the tendency of the current to forsake the interior of the wire cross section and crowd into portions near the surface of the wire [65].

المنارة للاستشارات
www.manaraa.com

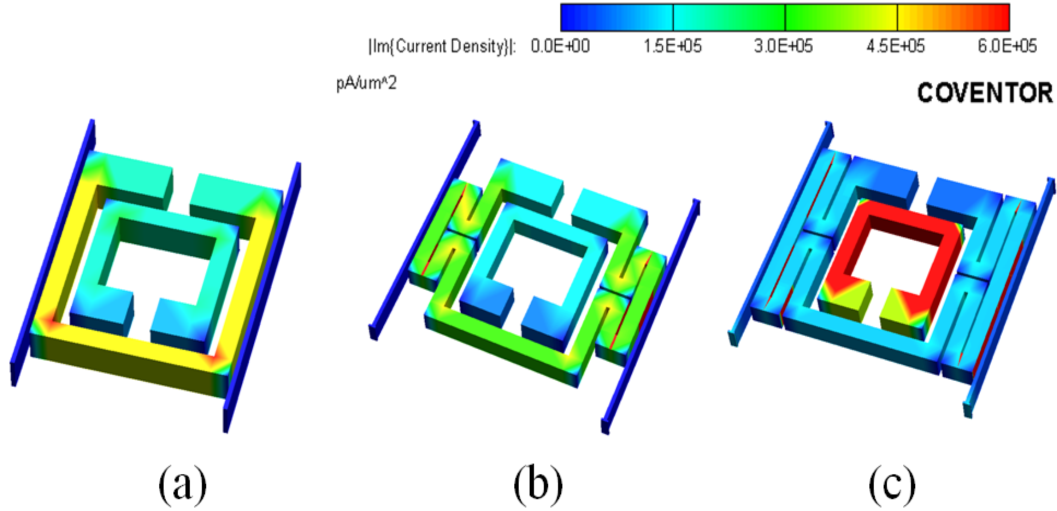

Figure 37. CoventorWare ® plots showing magnitude of imaginary current density incident on the (a) Baseline, (b) Loop A and (c) Loop B versions of the meta-atom designs. Changes in the imaginary current density were observed as the length of each loop increased from the Baseline to the Loop B design. The magnitude of the imaginary current density increases on the inner split ring resonator which is relative to the increase in inductance and capacitance. However, the magnitude of the imaginary current density decreases for the outer split ring resonator.

The CoventorWare ® simulations show a large inductance change can be achieved with minimal capacitance change. Table 4 lists the inductance and capacitance values obtained from the analytical modeling and simulations. Both designs show a shift in the resonance towards a lower frequency.

Table 4 Inductance and capacitance values obtained during modeling and simulations

Design	Outer Ring Inductance (nH)	Inner Ring Inductance (nH)	$C_{Section_B}$ (pF)	$C_{Section_C}$ (pF)	C_{Left_Side} (pF)	C_{Right_Side} (pF)	C_{Traces} (pF)	Resonant Frequency (GHz)
Baseline	26.19	13.87	0.04	0.037	0.128	0.128	0.053	2.70
Loop A	31.73	13.87	0.04	0.037	0.15	0.15	0.106	2.33
Loop B	46.94	13.87	0.04	0.037	0.153	0.153	0.106	2.20

المنارة للاستشارات
www.manaraa.com

4.3.2. CST Microwave Studio ® Modeling

CST Microwave Studio ® is a commercial full-wave electromagnetic solver that primarily uses the finite integration technique [66]. It can employ the finite integration technique in the time or frequency domain. The results from the simulations are often provided in the form of scattering parameters. From the scattering parameters, effective material parameters can be calculated using the approach described by Smith *et al*. and Chen *et al.* [36], [37]. Simulation performed for specific designs provided a comparison between the CoventorWare ® and CST Microwave Studio ® values. A thorough explanation for the capabilities from CST Microwave Studio ® is provided by Jussaume [67]. All simulations detailed in the following sub-sections were completed on the AFIT low observable radar and electromagnetic network (LOREnet) machines. The computers are Dell Precision 690™ Workstations with one Quad 3.00 GHz Intel Xeon ® processor and 32 GB of RAM. All workstations run Windows ® XP Professional x64.

4.3.2.1. 10 – 15 GHz Gap based Designs

Jussaume simulated the 10 – 15 GHz AFIT-designed adaptive metamaterial structures (meta-atoms) in CST Microwave Studio ® for the following models: 1) A single cell structure with periodic boundary conditions, 2) A single cell structure with non-periodic boundary conditions, 3) A column of four unit cells placed in the waveguide used for measurements, and 4) A column of 17 unit cells placed in the waveguide used for measurements. On all four structures, the MEMS capacitor is modeled using a lumped network element. All the models are thoroughly explained by Jussaume in his thesis [67]. For instance, the 10 – 15 GHz baseline meta-atom shown in Figure 38 is simulated with

www.manaraa.com

periodic boundary conditions along the xy-plane. The z-boundaries are the Floquet ports or the source ports for problems with periodic boundary conditions. This is the source location and the measurement area for the S-parameters analysis [67]. With the boundary conditions set, the simulation is solved using the frequency domain solver for the frequency range 1 to 25 GHz. Figure 38 shows the bulk meta-atom sample used in the simulation. Figure 39 is plots of the results of the S-parameter analysis for the baseline meta-atom design without the lumped element variable capacitors used in the simulation. The magnitudes of the simulated reflection (S_{11}) and transmission (S_{21}) cross near 11 GHz, 20 GHz, and 23 GHz indicating resonant locations.

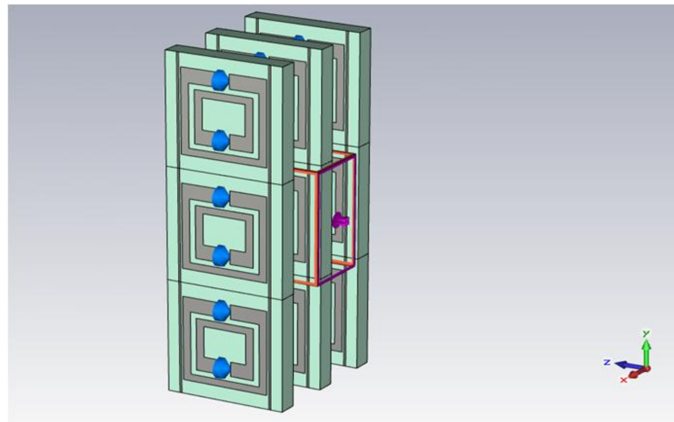

Figure 38. CST Microwave Studio ® model of the Baseline meta-atom designed with lumped element capacitors. Periodic boundary conditions are used in the xy-plane. [67]

www.manaraa.com

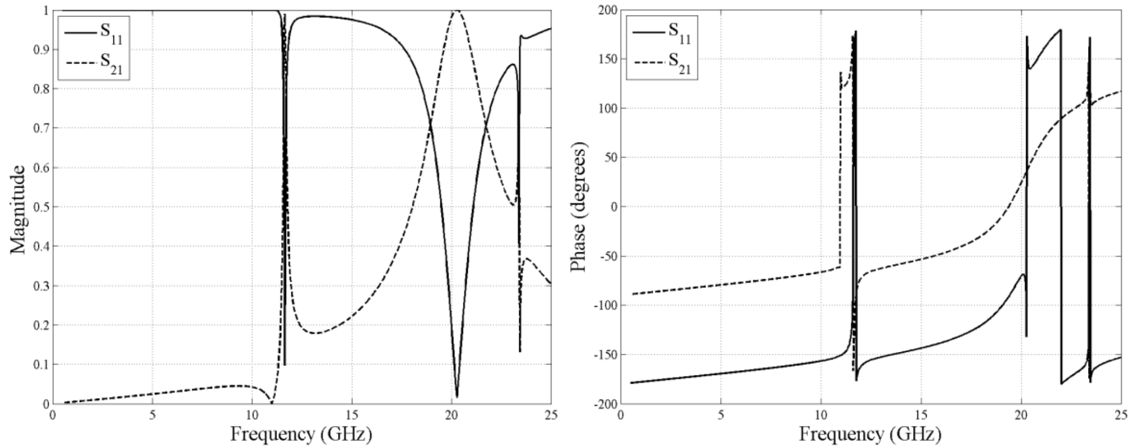

Figure 39. S-parameter results from the single cell periodic model with fixed gap capacitance. (a) The magnitudes of S_{11} and S_{21} show resonance points near 11, 20 and 23 GHz. (b) The phases of S_{11} and S_{21} show the largest changes around the resonance points [67].

Along with the baseline meta-atom design, Jussaume performed simulations on several other iterations of the 10 – 15 GHz meta-atom design to include not only the lumped element capacitors, but included cuts in the outer ring. The simulated cuts were to demonstrate how well CST Microwave Studio ® could match the fabricated designs with cuts in the outer ring [67].

4.3.2.2. 1 – 4 GHz Gap based Designs

The 1 – 4 GHz meta-atom design discussed in section 3.2.2 was simulated in CST Microwave Studio ®. The five cantilevers located in the gap region of the split ring resonators were implemented with lump element capacitors for the simulation. To construct the design in the simulation, the 1 – 4 GHz based design was simulated using the following models. 1) A unit cell model extending infinitely in the two non-propagation directions, stimulated by a transverse electro-magnetic (TEM) mode. 2) A single cell model stimulated by a TEM mode with the electric field oriented along the

المنارة للاستشارات
www.manaraa.com

vertical wire traces. 3) Four meta-atoms in a column simulated in the model of the physical waveguide. These models are also used for the intra-ring meta-atom designs. The results for the four meta-atoms in a column are provided in Figure 40 (a), which shows the dispersive transmission results and an area of resonance above 2 GHz when all cantilever have the 2 μm gap. When the meta-atom has all cantilevers pulled-in, the capacitance shifts the resonant frequency below 0.5 GHz as shown in Figure 40 (b).

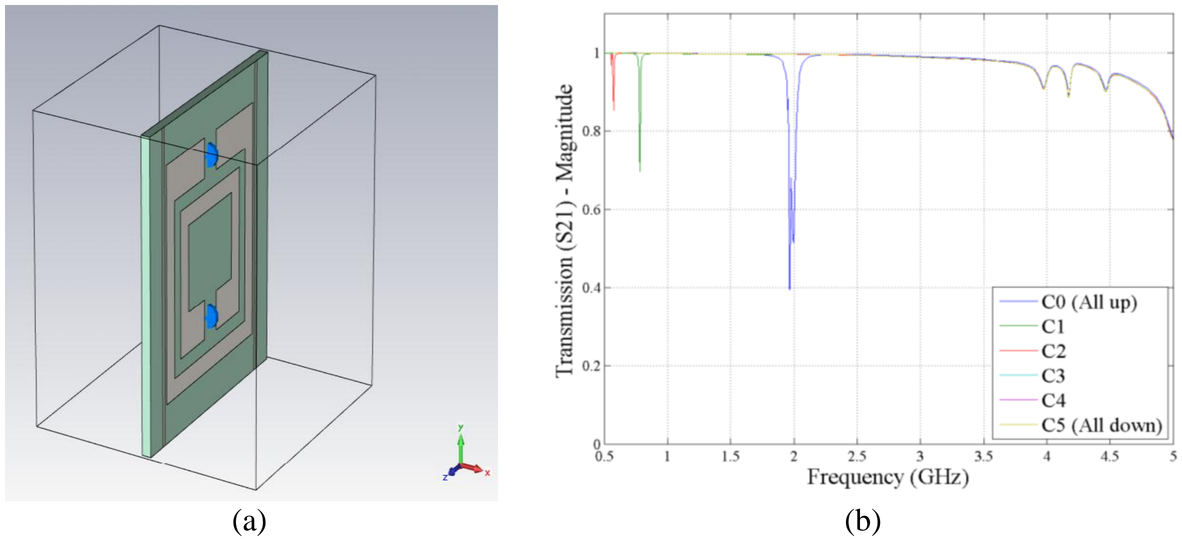

Figure 40. 1 – 4 GHz meta-atom integrated with cantilevers. The cantilevers are simulated with lumped elements capacitors.

4.3.2.3. 1 – 4 GHz Intra-ring Meta-atom Designs

The intra-ring meta-atom designs were simulated in CST Microwave Studio ® to compare with CoventorWare. The models were simulated in the same manner as the 1 – 4 GHz based design with lumped element capacitors. Figure 41 shows the three meta-atom designs used in the simulation with the location of the lumped element capacitors. The transmission response for each design arranged in a column with four meta-atoms is shown in Figure 41 under each design.

المنارة للاستشارات
www.manaraa.com

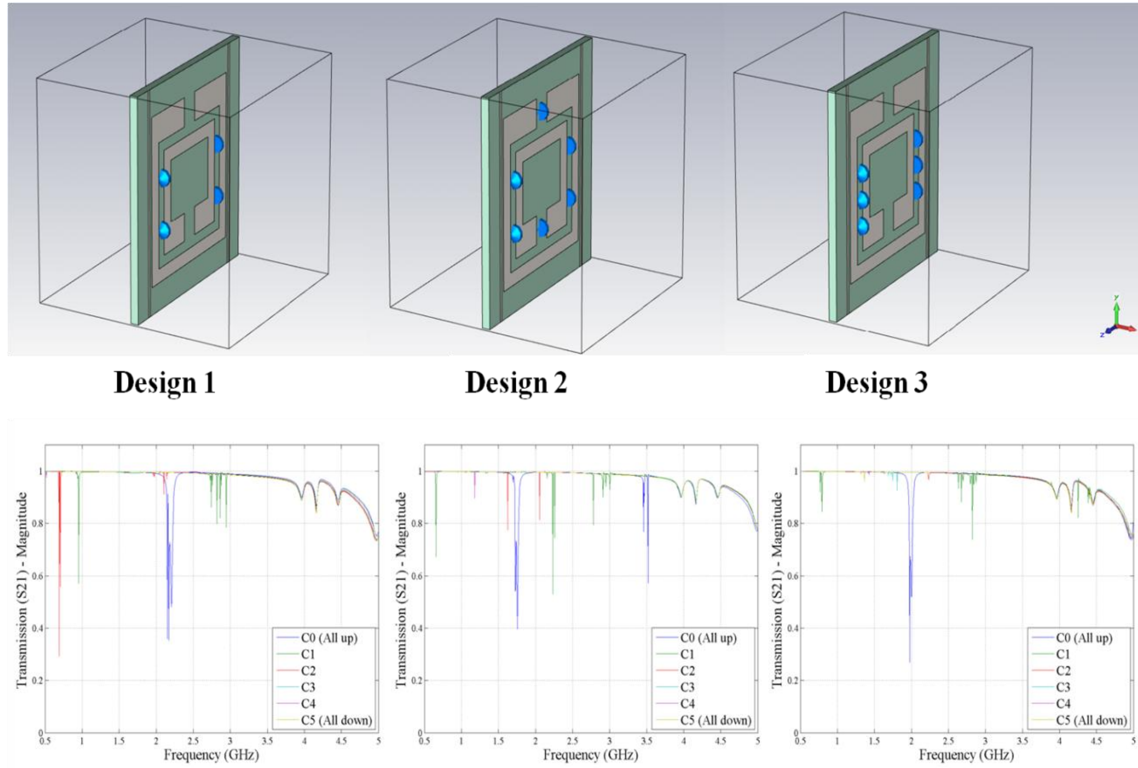

Figure 41 Intra-ring Meta-atom designs simulated in CST Microwave Studio®. The transmission response for each design show the resonant frequency shifts to lower frequency as the capacitance increases.

4.3.2.4. 1 – 4 GHz Inductance based Meta-atom Design

The Loop B inductance meta-atom design was simulated in CST Microwave Studio ® to compare to with the CoventorWare ® simulations. The design is based on the meta-atom discuss in section 3.3. For a comparison, a single meta-atom was simulated with periodic boundary conditions. The resonant frequency for the model implemented in CoventorWare ® predicted a resonant frequency at 2.20 GHz. The resonant frequency produced by this simulation is at a higher frequency of 2.5 GHz. Figure 42 shows a plot of the simulation results.

المنارة للاستشارات
www.manaraa.com

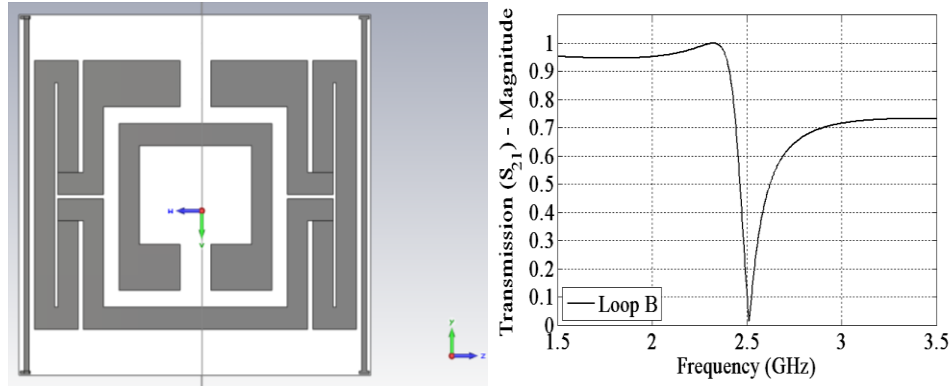

Figure 42. CST Microwave Studio ® simulation results for the Loop B Inductance Meta-atom design. The resonant frequency shifted to 2.5 GHz based on the added loop on the outer split ring resonator.

4.3 Summary

Modeling and simulation was completed on the RF meta-atom designs to provide a thorough understanding into the theory and application of the meta-atom designs that can be used as metamaterials. The analytical modeling provided a fundamental understanding for the behavior of meta-atom based on the capacitance and inductance parameters that produce the resonant frequency. Simulations conducted with CoventorWare ® and CST Microwave Studio ® provides computational analyses that help build understanding into the various designs and identify potential challenges. Based on the analytical modeling and simulations, the meta-atoms were fabricated and tested to compare with experimental results.

المنارة للاستشارات
www.manaraa.com

V. RF Metamaterial Experimental Results

Experimental testing was completed in AFIT's low observable radar and electromagnetic laboratory (LORElab). Testing capabilities for the LORElab covered testing on the meta-atoms over a radio frequency range of 0 – 20 GHz. To accomplish the testing, an Agilent E8362B Programmable Network Analyzer (PNA) and two RF strip-lines were set up for experimental testing. The PNA provides the capability to test from 10 MHz to 20 GHz. The PNA was used to stimulate the strip-line and collect the experimental S-parameter data. The S-parameter data shows the response of the propagating signal generated by the PNA to the meta-atom designs. The two RF strip-lines cover different frequency ranges which are 10 MHz – 4 GHz and 10 MHz – 18 GHz. Figure 43 shows the two RF strip-lines used in the experimental testing. Experimental testing was completed on Baseline, the capacitive tunable, inductive and active element based meta-atom designs which are described in the following sections.

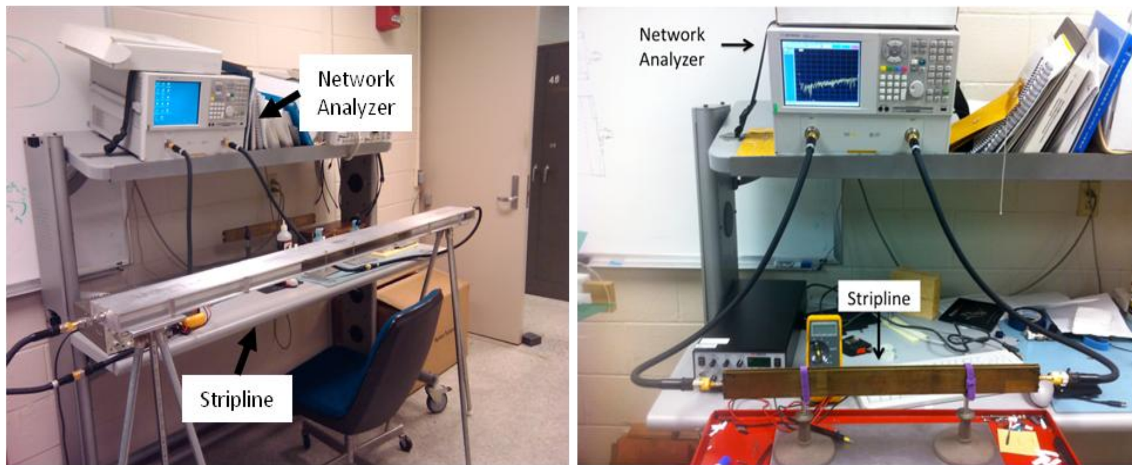

Figure 43. The Agilent E8362B Programmable Network Analyzer connected to 4 GHz strip-line and 10 GHz strip-line.

www.manaraa.com

5.1. Fixed Meta-atoms

The fixed meta-atoms are the Baseline designs at the 1 – 4 GHz and 10 – 15 GHz range. These fixed designs were modeled and fabricated to serve as references to any modifications. Because of the static structures, the fixed meta-atom designs produced a single resonant frequency which serves as a set point for all designs that implement a change to the resonant frequency. The Baseline designs were fabricated with FR4 printed circuit board and on quartz substrates using microelectronic fabrication techniques. The FR4 PCB samples served as rapid prototype samples helping to determine the experimental results for the meta-atoms. The samples on the quartz substrate served as testing samples to determine how well the results compared for microelectronic fabrication. The baseline samples were tested using the 10 MHz – 4 GHz RF strip-line, Agilent Programmable Network Analyzer, and cabling accessories. Figure 44 shows the 1 – 4 GHz Baseline sample inserted into the RF strip-line for testing. As shown, the Baseline meta-atom is arranged in columns containing four individual meta-atoms to effect the RF transmission. Figure 45 shows the transmission response that has a resonance at 2.83 GHz.

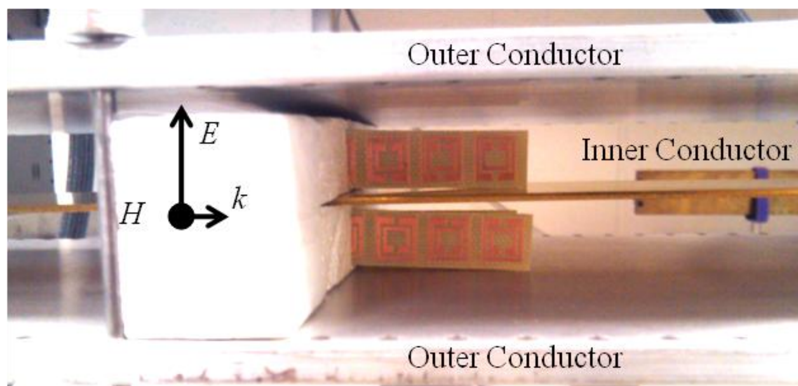

Figure 44. 4 GHz RF strip-line with 1 – 4 GHz Baseline meta-atom designs inserted for testing

www.manaraa.com

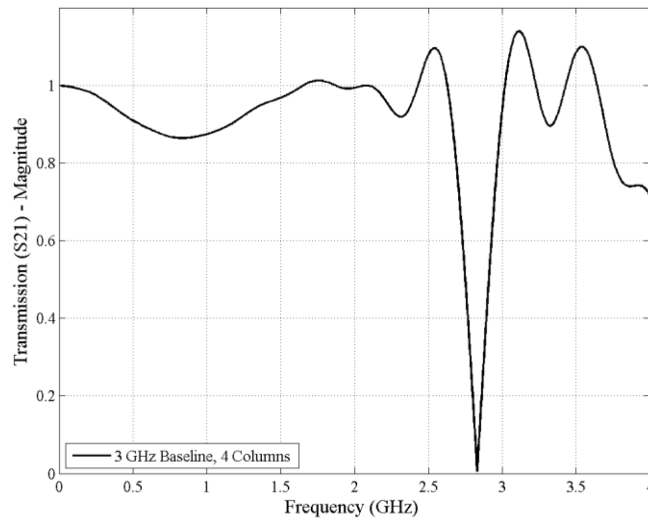

Figure 45. Transmission response captured for the 1 – 4 GHz Baseline meta-atom. The transmission magnitude approaches zero at 2.83 GHz.

The 10 – 15 GHz Baseline meta-atom was fabricated and tested in the same procedures used when testing the 1 – 4 GHz Baseline meta-atom. For this design, the resonant frequency occurred at approximately 10 GHz. Based on the design, samples were fabricated and placed into the 10 MHz – 18 GHz RF strip-line for testing in the 0 – 18 GHz range. Figure 46 shows the transmission response for the 10 – 15 GHz Baseline meta-atom along with the inset image of a sample in RF strip-line.

للاستشارات المنارة
www.manaraa.com

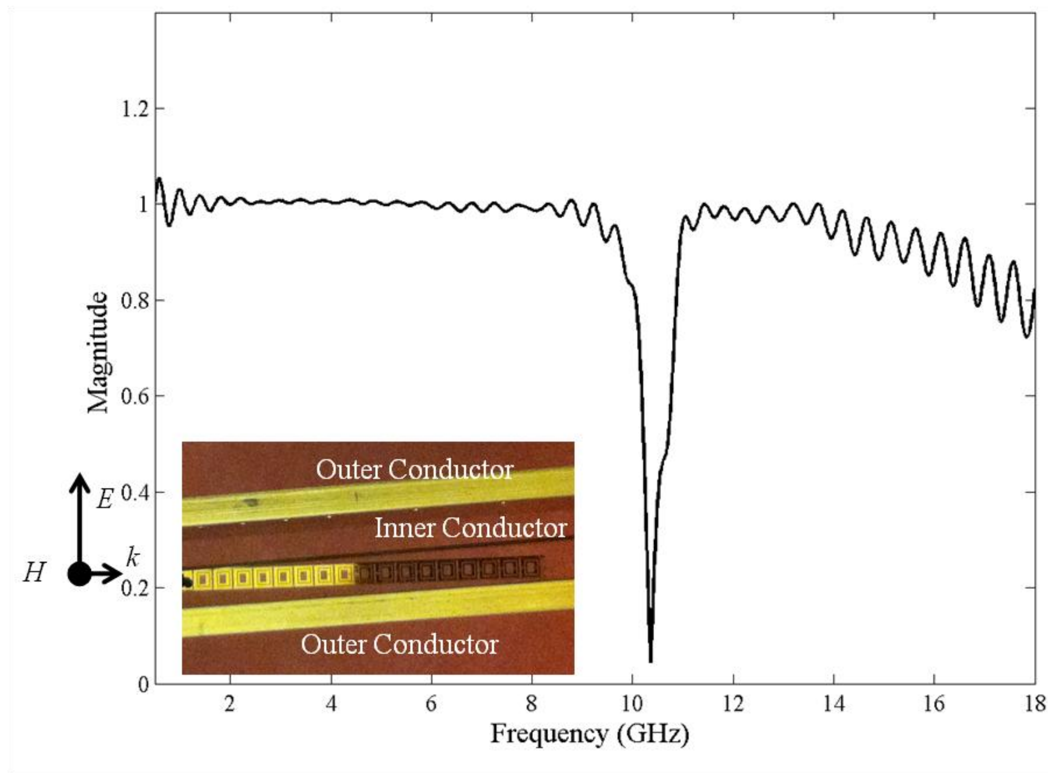

Figure 46. The transmission magnitude response captured for the 10 – 15 GHz Baseline meta-atom showing the resonant frequency occurring just above 10 GHz. The inset shows a 10 – 15 GHz Baseline meta-atom inserted in the RF strip-line between the inner and outer conductor.

5.2. Capacitive Tunable Meta-atoms

The first modification to the baseline meta-atom design involves the implementation of electrostatically actuated cantilevers. The purpose of the cantilevers is to provide a tunable element for the structure. The cantilevers were added to the split ring resonator's gap and between the rings for different designs. To test the designs, DC and RF testing was accomplished to evaluate the tunable meta-atom's overall performance. The DC testing ensured the cantilevers actuated and determined the actuation voltages of the beams. A Zygo white light interferometer helped to visualize the cantilever's actuation and pull-in based on the cantilever thickness and length. The RF testing

المنارة للاستشارات
www.manaraa.com

captured the transmission and reflection performance of the meta-atoms within the 10 MHz – 4 GHz RF strip-lines. Five designs were implemented to test the tunable meta-atom designs for 10 – 15 GHz and 1 – 4 GHz ranges and to include intra-ring variations.

5.2.1. 10 – 15 GHz Gap based Meta-atom Designs

The 10 – 15 GHz capacitive tunable meta-atom discussed in section 3.2.1 was fabricated using microelectronic fabrication. The samples were built on quartz substrates to isolate the structures within the RF strip-line. Samples were prepared into strips containing one row of 17 meta-atoms with contact pads at one end. The 17 cantilever arrays on the inner and outer split ring resonators were inspected prior to testing. A fabrication error was noticed on the design which required adjusting. The trace for the actuation pad that pulls down the cantilevers on the inner split ring resonator was shorted to the outer split ring resonator during the fabrication process used to electroplate the structure due to a photolithography mask error. To correct the error, a focused ion beam was used to mill out the trace isolating it from the outer split ring resonator by placing a gap in the resonator and by cutting the trace. Both methods were employed and devices were tested. Figure 47 shows the meta-atom and the two cutting methods used to isolate the outer split ring resonator. Also, it was observed that a few of the cantilevers were stuck down due to stiction. To release some of the cantilevers, an oxygen plasma asher was used to clean away residue and free the beams. The cantilevers were observed to actuate with an applied DC voltage and return to their original position as the voltages were decreased back to 0 VDC.

المنارة للاستشارات
www.manaraa.com

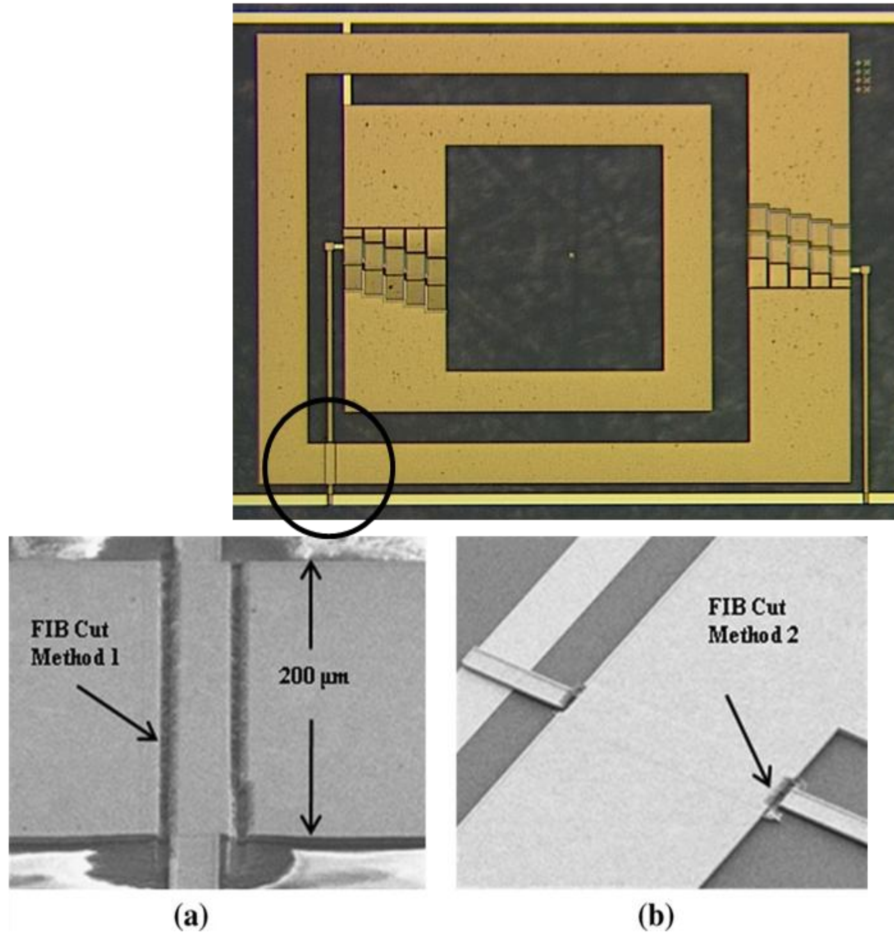

Figure 47. A 10 – 15 GHz Capacitive tunable meta-atom fabricated on quartz substrate. The meta-atom had to be cut at the metal trace leading to the cantilever actuation pads for the inner split ring resonator. Two types of cuts were created with a focused ion beam to isolate the split ring resonator which led to two testing methods.

After correcting the fabrication errors and stiction problems, the meta-atom arrays were tested for DC actuation. The Zygo tool provided visual data on the actuation of the cantilevers and helped determine the voltage range necessary to complete the RF testing. The cantilever actuation was captured with the Zygo at different voltage levels. Figure 48 shows cantilevers pulled down at 60 VDC which changed the capacitance of the meta-atom to the highest capacitance value.

المنارة للاستشارات
www.manaraa.com

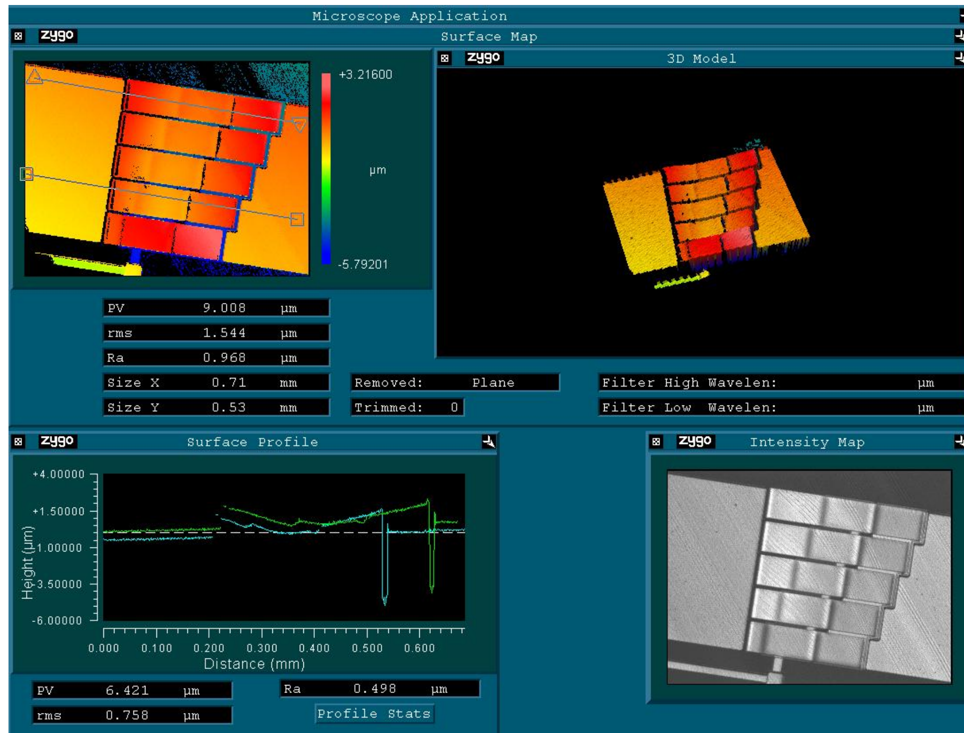

Figure 48. Cantilevers pulled-in at 60 VDC. Image captured during DC testing on meta-atom array. All the cantilevers are pulled-in which represents the maximum capacitance value achieved.

The two methods used to cut the outer split ring resonator caused the initial resonant frequency to shift away from the expected resonance frequency with no applied voltage. The initial resonant frequency is a result of the capacitance based on the gap under the cantilevers and by the gap due to the focused ion beam cuts. The meta-atom array was inserted into the RF strip-line for testing. The cantilever actuation pads were biased with the same actuation voltage observed in DC testing. The transmission response from the meta-atom array cut by the first method showed a initial resonance at 14.2 GHz. Applying a voltage up to 60 V shifted the resonance frequency to as low as 12.6 GHz for the meta-atoms. Figure 49 shows the transmission magnitude for the meta-atom array along with an inset zoomed in on the range where the resonance frequency shift occurs.

المنارة للاستشارات
www.manaraa.com

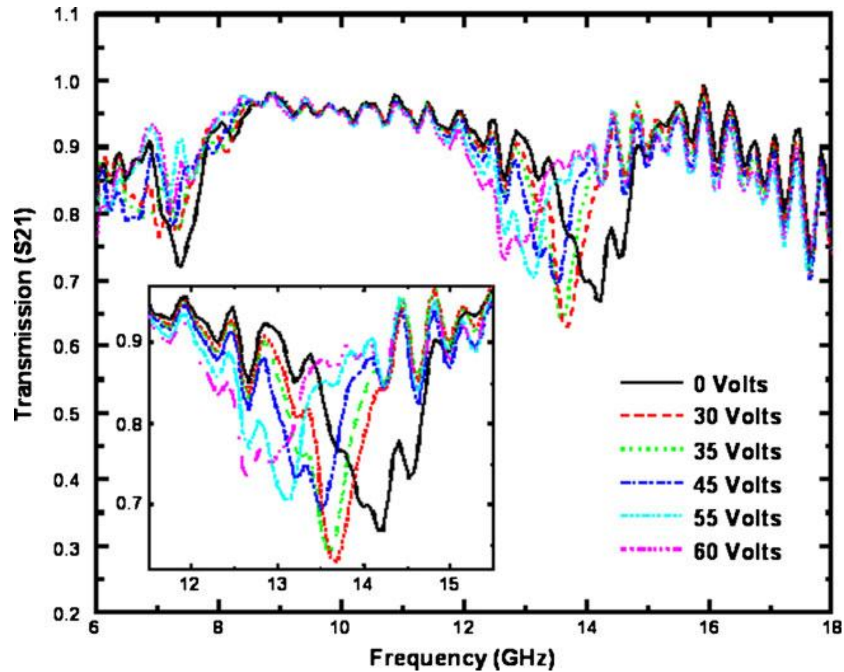

Figure 49. Transmission from a 1 × 17 array of the 10 – 15 GHz Capacitive Meta-atom with cut across the outer split ring resonator. As the applied voltage is increased the resonant frequency shifts from 14.2 GHz to 12.6 GHz.

The second focused ion beam cutting method used to isolate the outer split ring resonator caused a slightly different shift in the initial resonant frequency. Figure 50 shows the transmission response for the meta-atom array. The voltage level on the plot is not as high on this array compared to the array cut using the first method. The sample shorted out during testing and no other data could be collected. Based on the testing, the resonance frequency starts out at 8.4 GHz and shifts to 8.04 GHz which is a smaller shift when compared to the other meta-atom array. The smaller resonant frequency shift is attributed to the different effects the added capacitance will have on the inner/outer split ring resonators due to their size difference. The sample also has a resonance at 13.5 GHz that does not tune as the cantilevers are actuated and may be an artifact of capacitive gap from the FIB cutting.

المنارة للاستشارات
www.manaraa.com

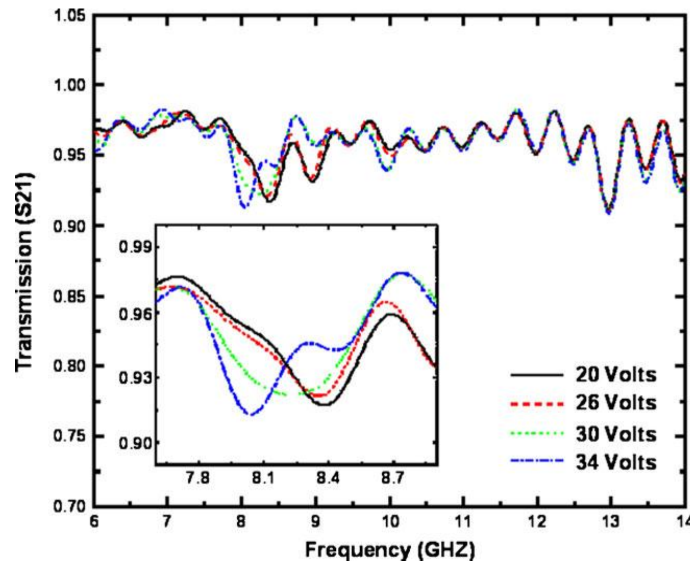

Figure 50. Transmission from a 1 × 17 array the 10 – 15 GHz Capacitive Meta-atom with cut across the metal trace. As the applied voltage is increased the resonant frequency shifts from 8.4 GHz to 8.04 GHz.

The 10 – 15 GHz capacitive meta-atom showed that tuning the resonance frequency is possible. Modifying the structure with embedded electrostatic cantilevers worked as expected. The errors in the fabrication were a minor setback but using the focused ion beam to correct the fabrication error proved to be a suitable fix.

5.2.2. 1 – 4 GHz Gap based Meta-atom Designs

The meta-atom design was scaled up by a factor of four to help with testing. The design was discussed in section 3.2.2 which provided background on the reason for scaling and the dimensions used for the design. Based on the design and modeling, the 1 – 4 GHz meta-atom design was fabricated and tested to compare the experimental results to the modeling and simulations.

Once again, the tunable meta-atom performed as expected, with the initial resonant frequency occurring at 2.06 GHz. The resonant frequency change was similar to what the simulation predicted with a change of 0.18 GHz compared to the estimated

المنارة للاستشارات
www.manaraa.com

change predicted by the simulation of 0.11 GHz. Figure 51 shows the meta-atom array suspended in the RF strip-line by Styrofoam. Figure 52 shows the transmission response to the meta-atom and the resonance shift occurring as the actuation voltage increases.

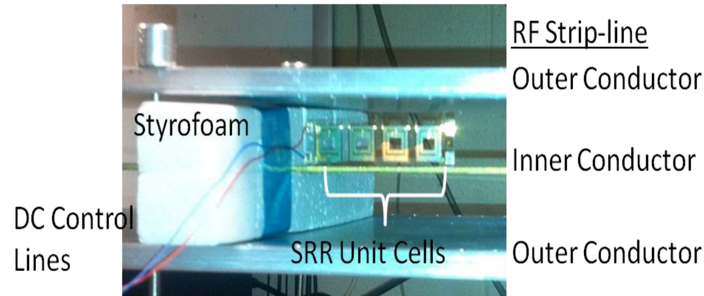

Figure 51. Experimental setup showing 4 unit cells of the 1 – 4 GHz meta-atom embedded with cantilever in the gap and placed in the RF strip-line. The image shows the DC wires bonded to the actuation pads to control the electrostatic actuation. The array is suspended between the inner conductor and outer conductor by styrofoam to help with electrical isolation.

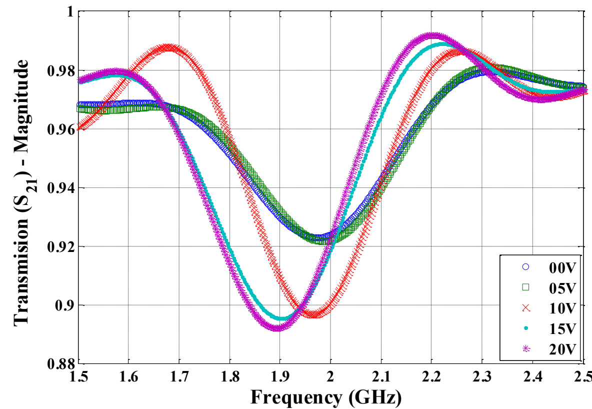

Figure 52. Plot of the transmission response for the meta-atom design with cantilevers embedded in the split ring resonator's gap. The initial resonant frequency occurs at 2.06 GHz as predicted by the simulation; however, the change in resonance shifts by 0.18 GHz.

5.2.3. 1 – 4 GHz Intra-ring Meta-atom Design

Three intra-ring meta-atom designs are inserted into the RF strip-line as shown in Figure 51 to obtain the RF response. From this testing, the S-parameter data for transmission and reflection is collected. Figure 53 shows the transmission response to

www.manaraa.com

each design ranging from 100 MHz to 2.0 GHz. Using these measurements, the experimental data results are compared to the simulations for resonant frequency comparison. Based on simulations, capacitance changes as a function of the cantilever separation gap. However, the design produced unexpected results. Design 1 has a resonance response lower than expected based on the simulation which shows a resonance at 1.56 GHz. In the measurements, a resonance occurs at 1.3 GHz with no significant shift. Design 2 measurements show a resonance occurring at 1.2 GHz; however, the signal null is not as deep as the baseline design. This is attributable to the capacitance separation gap of the electrostatic cantilevers which is not consistent across the row of meta-atoms. Inspecting the cantilevers after fabrication showed some cantilevers were not at the same initial position. Some cantilevers had larger gaps and some cantilevers had smaller gaps which affected the capacitance values for each meta-atom. In the final operational state, the resonance shifts away from the 1.2 GHz point but is not seen across the frequency range during testing. For Design 3, the resonance is not significant nor does the resonance response change from the initial to the final operational state. Based on the measurements, the capacitance change has not affected the overall capacitance enough to shift the resonant frequency.

المنارة للاستشارات
www.manaraa.com

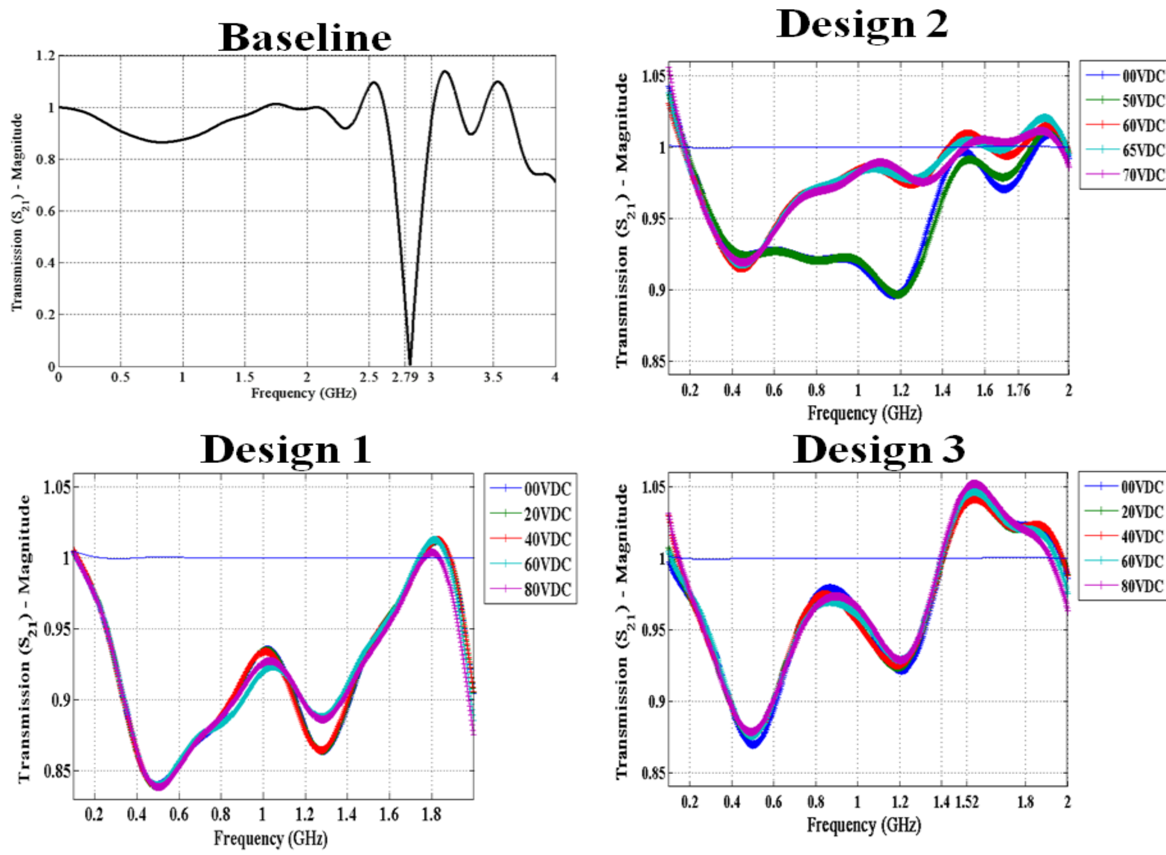

Figure 53 Transmission responses for the Baseline and three modified meta-atom designs in the initial and final operational states.

5.3. 1 – 4 GHz Inductance based Meta-atom Designs

The inductance based designs discussed in section 3.3 were fabricated to compare the modeling results with experimental data.

5.3.1. Static Designs

Experimental testing was completed on the inductive meta-atom designs using the 10 MHz – 4 GHz RF strip-line and PNA. Two sets of the three designs were fabricated; one set was prototyped on FR4 printed circuit board with single sided copper and the second set was fabricated using microelectronic techniques. These prototype designs were tested in the RF strip-line. Figure 54 shows how the Loop B design appears when

المنارة للاستشارات
www.manaraa.com

inserted into the RF strip-line. As the wave propagates down the RF strip-line, the meta-atoms affect the applied electric field (**E**) and magnetic field (**H**) when placed above and below the center conductor. In this configuration, the applied fields emulate a plane wave illumination of a larger metamaterial array.

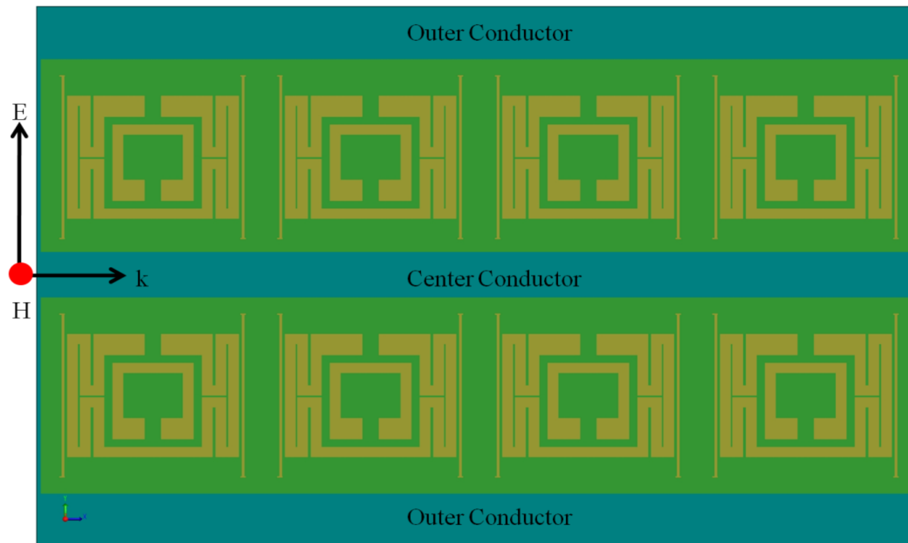

Figure 54. Meta-atoms inserted in the RF strip-line between the center and outer conductor. The signals propagating down the strip-line generate planar electric and magnetic wave from the center to the outer conductor.

The prototype designs, on the FR4 PCB, were completed using a T-Tech Inc. Quick Circuit 5000 milling system. From the PCB prototype devices, the fabrication transitioned to microelectronic fabrication where the meta-atoms were fabricated on semiconductor substrates (76 mm quartz substrates). The reason for using microelectronic fabrication is to broaden the available fabrication options. Microelectronic fabrication allows several design of experiments based on various metals, dielectrics and substrates. The fabrication process used to create these structures consisted of evaporating titanium (Ti) adhesion layer and gold (Au) seed layer. A photolithography mask was used to define the SRR and the traces. The split ring

المنارة للاستشارات
www.manaraa.com

resonators and traces are electroplated with gold onto the seed layer to define the final structures. The extra titanium and gold evaporated layers were then removed, leaving only the meta-atoms and traces on the quartz substrate. Figure 55 shows the completed samples made on the FR4 PCB and on the quartz substrates. The FR4 PCB samples have rough edges, resulting from the milling process, while the samples fabricated using the microelectronic techniques have much smaller minimum feature sizes and greater resolution. The rough edges and minimum feature sizes have the effect of reducing the magnitude of the resonant null and location of the resonant frequency.

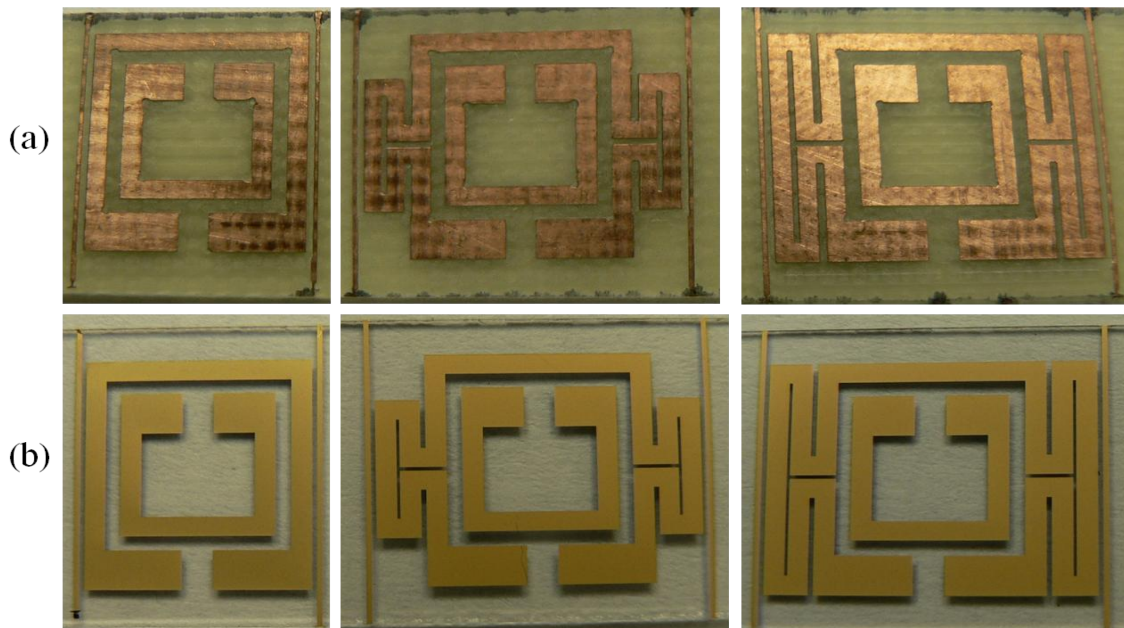

Figure 55. Fabricated Inductance based meta-atom designs: a) prototypes on printed circuit board and b) designs made by microelectronic fabrication techniques on quartz substrates. The FR4 PCB samples have rough edges which is a result from the milling process. The microelectronic fabrication improved the edges on the samples.

A 1 x 4 array of each SRR meta-atom design (Baseline, Loop A, Loop B) was tested using an RF strip-line test fixture. The meta-atom arrays are inserted into a 4 GHz strip-line oriented normal to the transverse electromagnetic mode for RF testing (i.e.

المنارة للاستشارات
www.manaraa.com

parallel to the propagation vector). An Agilent Technologies E8362B programmable network analyzer was then used to measure S-parameters within the 1.5 – 3.5 GHz spectrum incident on the meta-atom arrays.

The resonance frequency shifted based on the different designs as expected, matching the simulation results for the Baseline, Loop A, and Loop B designs. The resonant frequency for the Baseline, Loop A and Loop B designs fabricated on printed circuit board (FR4 PCB) are 2.68, 2.37 and 2.18 GHz, respectively. The designs fabricated on quartz wafers showed resonant responses at 2.78, 2.45, and 2.24 GHz, respectively. The difference is attributed to the dielectric constants of the two substrates and the level of resolution for the two fabrication methods. The resonant frequency of each fabrication process design is shown in Figure 56. The experimental data collection is close to the simulation results shown in Table 4. Figure 56 (a) shows the data collected from two arrays of FR4 PCB meta-atoms spaced 10 mm apart which form a 2D structure. Figure 56 (b) shows the data collected from two arrays of quartz substrate meta-atoms spaced 10 mm apart also forming a 2D structure. Increasing the loop size causes the resonance to shift to a lower frequency with the greatest shift occurring on the Loop B design in which the loop equals the vertical side of the outer SRR ring as shown in Figure 55 (c). Adding more meta-atom arrays and increasing the size of the 2D structure in the RF strip-line increases the magnitude of the resonant frequency null.

المنارة للاستشارات
www.manaraa.com

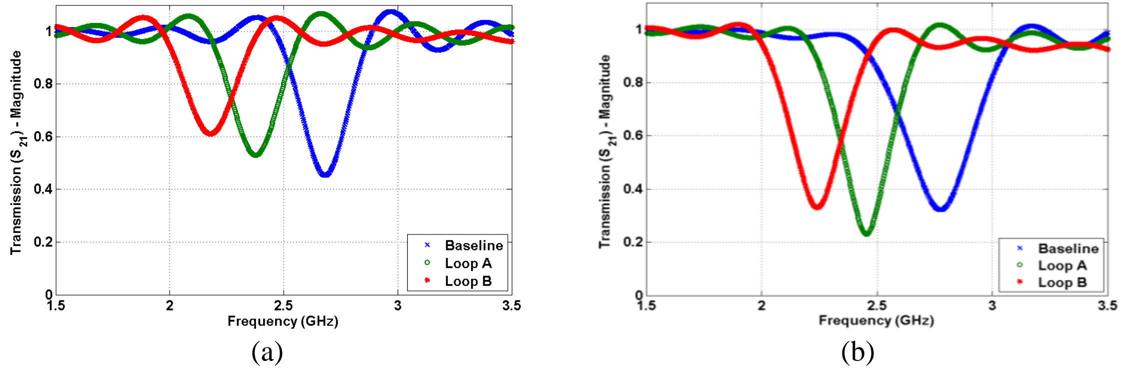

Figure 56. a) Data collected on meta-atoms fabricated on FR4 printed circuit board. b) Data collected on meta-atoms fabricated on quartz substrates. The samples are measured in a 4 GHz strip-line to obtain the small signal S-parameters.

The effective refractive index, permeability and permittivity are calculated for each design as a function of frequency. The calculations are based on previous work conducted by Smith *et al*. and Chen *et al.* [30], [37]. The values are generated using real and imaginary S-parameter data collected for the different designs. Figure 57 shows the effective values of the refractive index for each design calculated with data collected on two arrays (1×4) of meta-atoms placed in the RF strip-line The effective refractive index shifts to lower frequencies, which is consistent with the transmission data of the samples as shown in Figure 56 (a) and (b). The effective real refractive index decreases below zero on the x-axis (and goes negative) for all of the designs. These experimental results prove the effect that these meta-atoms have on the propagating signals.

المنارة للاستشارات
www.manaraa.com

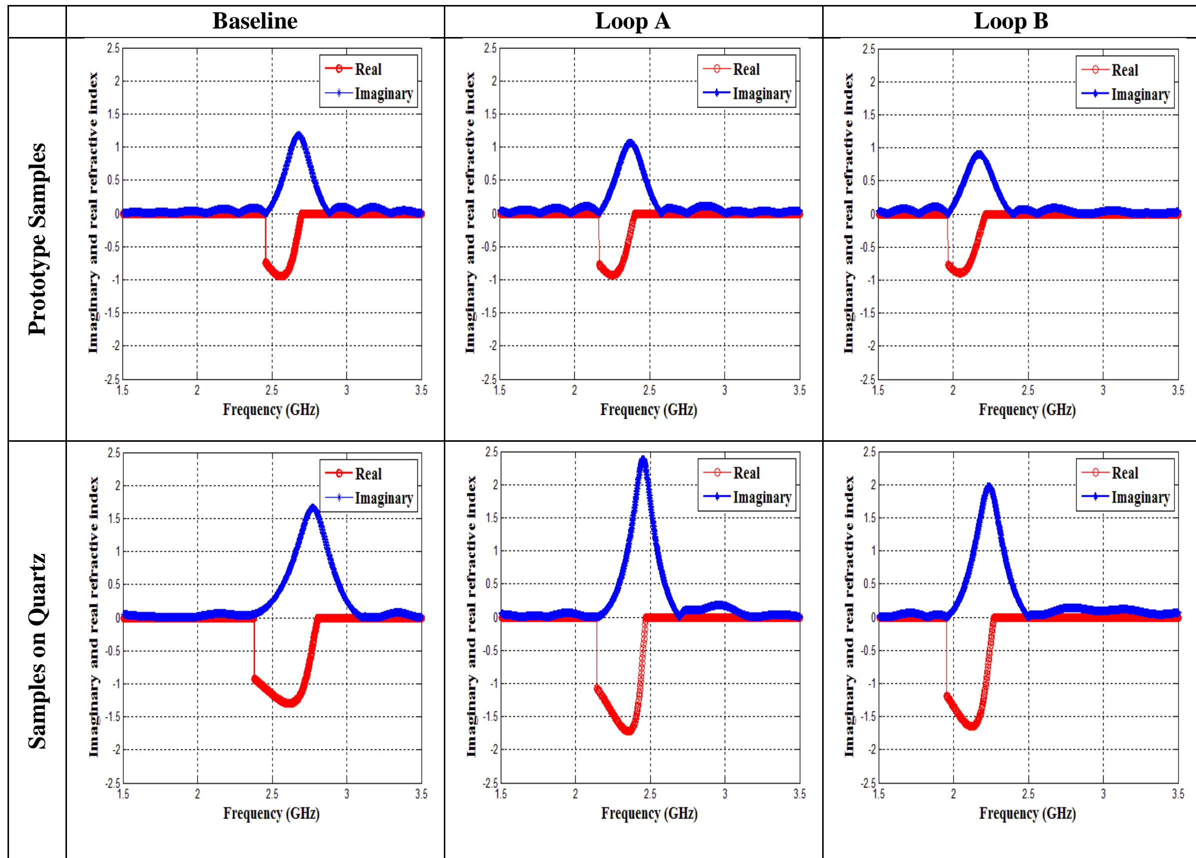

Figure 57. The effective refractive index (n) for each design calculated from transmission data collected between 1.5 – 3.5 GHz.

5.4. 1 – 4 GHz Active Element based Meta-atom Design

Two samples of the 1×4 array of the meta-atom design integrated with low noise amplifiers were placed between the inner and outer conductor of a 4 GHz RF strip-line as shown in Figure 58. The meta-atom arrays are inserted into the strip-line oriented normal to the transverse electromagnetic mode for RF testing. An Agilent Technologies E8362B programmable network analyzer stimulates and measures the RF signal. S-parameters within the 10 MHz to 4 GHz range incident on the meta-atom arrays are collected for analysis.

المنارة للاستشارات
www.manaraa.com

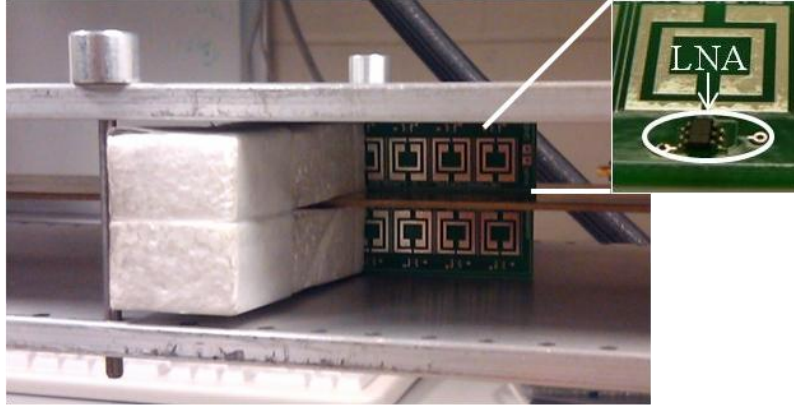

Figure 58. 1 – 4 GHz meta-atoms integrated with LNAs placed in 4 GHz RF strip-line.

The resonance frequency appears at 3.85 GHz slightly higher than the simulated values. The meta-atom with the LNA shows a stronger null at the resonant frequency. Integrating the LNA into the split ring resonator increased the resonant null for the meta-atom, but is based on the amount of biasing voltage applied. For comparison, a 1 – 4 GHz Baseline sample without a gain medium is tested to see how the resonance null compares to the meta-atom integrated with the LNA. The resonant frequency for the Baseline sample appears at 2.69 GHz and reduced to -5.51 dB. As another comparison, samples were made with a gap in the Baseline outer split ring resonator. Test results for this sample shows a resonance at 3.86 GHz with a -2.61 dB null. These experimental results match the simulation results for the resonant frequency location. With the amplifier turned off (0 VDC), the resonant frequency appears at 3.75 GHz with a reduction in the transmission to -11.82 dB. As the biasing voltage increases, the resonant frequency shifts to as much as 3.95 GHz with transmission reduced to -23.21 dB when biased at 7.0 VDC. Figure 59 (a) and (b) show the transmission data plotted for the meta-atoms over the 10 MHz to 4.2 GHz range. Measurements above 4 GHz are not viable for our RF strip-line which starts to multimode.

المنارة للاستشارات
www.manaraa.com

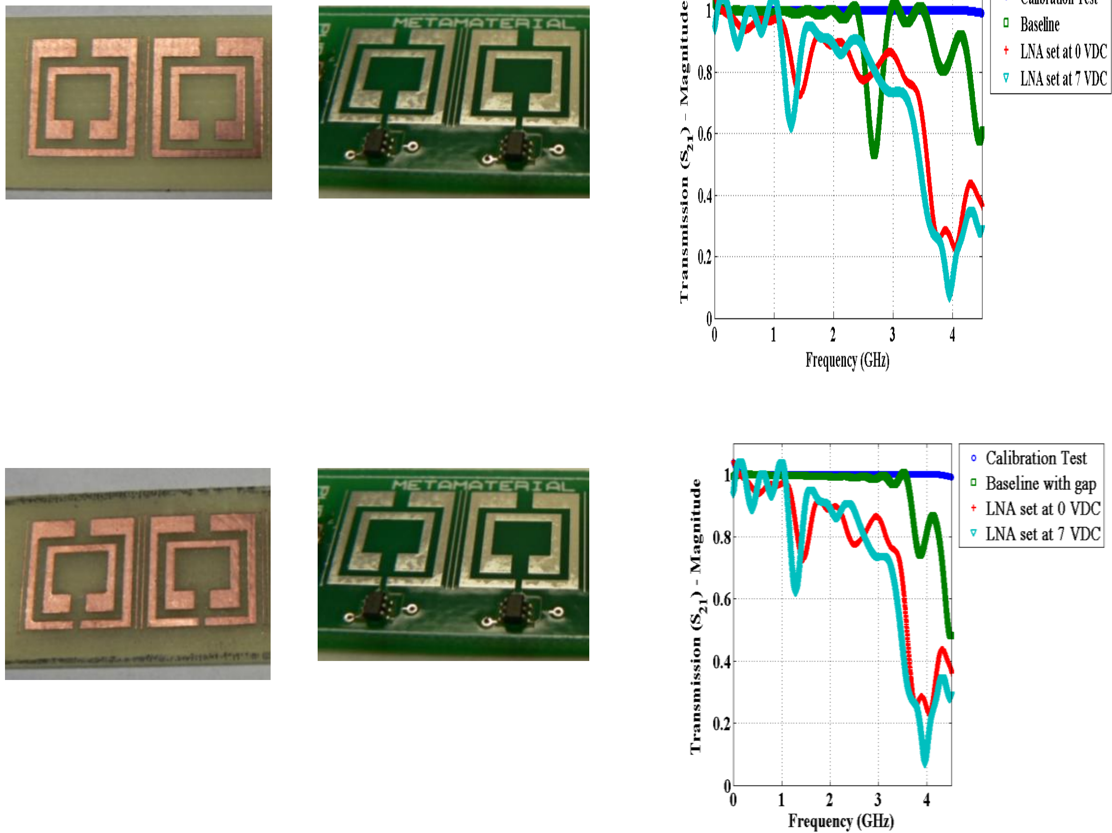

Figure 59. a) Transmission response for the meta-atoms in the RF strip-line. The Baseline, Baseline with a 0.4 mm gap in the outer split ring resonator and meta-atom integrated with the low noise amplifier were tested using a programmable network analyzer. The data is collected over 10 MHz to 4 GHz. In the plot, the frequency range is 10 MHz to 4.2 GHz to show the location of the resonant frequency. Samples are taken at biasing steps from 0 to 7 VDC at one volt intervals. The transmission response plots show the resonant response at 0 and 7 VDC.

5.5. Summary

Experimental testing was completed on several design iterations. The Baseline, Tunable Capacitive, Inductive Static and Active element designs provided valuable insight into the way RF signals are affected by the meta-atom structures. The deepest resonant null occurred for static and active element integrated structures at fixed frequencies. While the capacitive tuning meta-atom designs provided valuable insight

المنارة للاستشارات
www.manaraa.com

into the best location to place elements that shift the resonant frequency. The research conducted on the different meta-atom designs help understand the theory, modeling, fabrication and testing of tunable RF meta-atoms.

المنارة للاستشارات

www.manaraa.com

VI. Conclusion

6.1 Research and Contributions Summary

The modeling, design, fabrication and testing of various tunable RF meta-atoms is carried out in order to understand the effects of changing the structure, integrating tunable components and inserting active elements in the meta-atom. Metamaterials are formed with arrays of meta-atoms, and based on structural changes for tuning meta-atom shown in this research more insight is provided into the behavior of propagating signals effected by these structural modifications.

Using electrostatically actuated MEMS varactors, tunable RF meta-atoms were demonstrated which shifts the resonant frequency using capacitance as a varying factor. Designs were made at two different frequency ranges (1 – 4 GHz and 10 – 15 GHz). The baseline double split ring resonator was modified to integrate the electrostatically MEMS varactors at different positions on the structure. The level of tuning for various designs varied based on the locations of the MEMS varactors. The design with MEMS varactors inserted at the split ring resonator gap provided the best tuning method and shifted the resonant frequency based on the amount of capacitance change. Designs with the MEMS varactors situated between the inner and outer split ring resonator showed no significant change in the resonant frequency location.

As a novel approach, the self-inductance of the meta-atom design was a focus to shift the resonant frequency. Based on the 1 – 4 GHz baseline design, structural modifications were designed, modeled, fabricated and experimentally tested to demonstrate how inductance can be used as a parameter to shift the resonant frequency.

المنارة للاستشارات
www.manaraa.com

Using the baseline and two design modifications, the overall self-inductance of the meta-atom was incrementally increased using loops on the outer split ring resonator and provided a shift in the resonant frequency for the RF meta-atom. Through the change in self-inductance, the resonant frequency shifted 0.60 GHz (2.78 GHz to 2.18 GHz) based on the amount of inductance variation. Based on the shifting resonant frequency, the self-inductance parameter is a viable method to build tunable RF meta-atoms.

The third contribution from this research into tunable RF meta-atoms comes from the investigation into active elements compensating for loss at the resonant frequency. To compensate for the loss, the active elements help by providing a gain element within the structure. Accomplishing the design, modeling, and fabrication, a LNA was integrated into the structure which operates using low DC bias (0 to 7 VDC) to provide RF gain. Based on experimental results, as the biasing voltage increased, the active element meta-atom produced a response that improved the resonant null demonstrating that loss can be compensated with gain. The lowest transmission level (-23.21 dB) occurs while the LNA is fully biased (7 VDC). Using the active element within a meta-atom has proven to be a viable method to compensate for loss and stands as a significant contribution

Base on these three contributions, the research conducted during this effort will provide understanding into tunable RF meta-atoms. The experimental results confirm the design and simulation results for the RF meta-atoms. Based on the results, new areas of design, simulation and experimental testing of meta-atoms can be further investigated leading to applications with metamaterials.

المنارة للاستشارات
www.manaraa.com

6.2 Recommendations for Future Research

6.2.1. Tunable Inductance Meta-atom Design

In order to make meta-atoms that change the resonant frequency based on inductance changes, a new method is to be developed where the structural dimensions of the meta-atom remain constant but the inductance shifts based on either an electrical, thermal or chemical response of an Metal Insulator Transition (MIT) phase change material. One of the alternatives is based on using a thermal response to alter the inductance. Based on background research, the phase-change material is a viable material option to carry out this experiment [68], [69], [70]. The concept behind using this material is that a thermal stimulation to the material causes the material to change from a resistive to a more conductive state. This leads to a change in the inductance based on the opposition to current flowing through the material. As the level of current changes, the inductance will shift the resonant frequency.

6.2.2. Meta-atoms combined into Metamaterials for 2-D Focus Beam System

The metamaterial composed of a large area array of meta-atom is required to test with a 2-D Focused Beam System. Building up to the large area metamaterial array has been a long term focus for the tunable meta-atom research. Combining the experience gained from the research on meta-atoms and the ability to mass produce the metamaterial array using microelectronic fabrication techniques will provide valuable insight into what is required for the overall design. As a lead-in to future developments, an explanation into the 2-D Focused Beam System and initial design consideration are discussed to help understand the reasons for implementing a 6 – 8 GHz metamaterial design for the system.

www.manaraa.com

The 2-D Focused Beam System simulates plane-wave illumination of targets in a compact area using lenses to focus radiation in the form of a Gaussian beam [71]. The 2-D Focused Beam System performs measurements on larger samples that can't be measured in the stripline using a Gaussian beam. Samples need to be one unit cell high and the "hall of mirrors" effect creates the infinite periodicity in that direction. At the waist of a Gaussian beam, the phase is planar while the amplitude is tapered to eliminate edge diffraction effects of a finite sized sample [71]. For material samples that are planar and homogeneous, such as metamaterial, a Gaussian beam illumination successfully simulates plane-wave illumination. Also, many inhomogeneous and anisotropic samples such as honeycomb can be successfully modeled assuming homogeneity by using an effective dielectric constant. A word of caution must be taken into consideration for these measurements. That is, homogeneity assumptions for material samples using structures of periodic elements, either metallic or dielectric, are sometimes inaccurate [71]. Figure 60 shows a schematic diagram of a focused beam system with the transmission and receive antennas, two focusing lenses and a sample centered at the focal point of the lenses. The dash line extending from the antennas in Figure 60 represents the propagating signal which the width is based on the frequency of the transmitted signal. For instance, higher frequencies will have a smaller spot size focused toward the center of each lens.

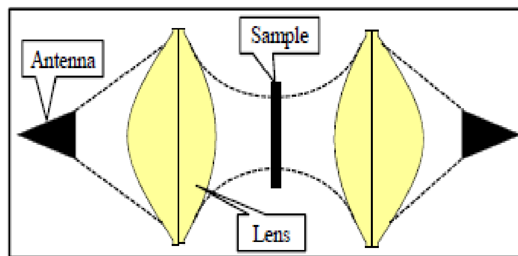

Figure 60. Schematic of a focused beam system [71].

المنارة للاستشارات
www.manaraa.com

The meta-atom required for a resonant response at 6 – 8 GHz is on the size of several millimeters in length and width. The analytical modeling completed on the baseline designs at 1 – 4 and 10 – 15 GHz continues to apply for this meta-atom arrayed into a metamaterial structure based on the effective permeability and permittivity parameters. To begin the design, a baseline design was constructed using L-Edit for the photolithography mask designs. In order to build the metamaterial, the design has to cover an area 729.66 cm^2 to reduce edge illumination to negligible levels on the Gaussian beam when the sample size is too small. To build up the metamaterial for the area, the design which covers an area less than 26.2 cm^2 is duplicated using several substrates and placed side by side to cover the focus area in the 2-D Focused Beam System at the desired resonant frequency. A baseline design at 7 GHz should be constructed to help test the microelectronic fabrication process and test the meta-atom design within the 2-D Focused Beam System. Figure 61 shows a prototype of the meta-atom used as the baseline design for the metamaterial.

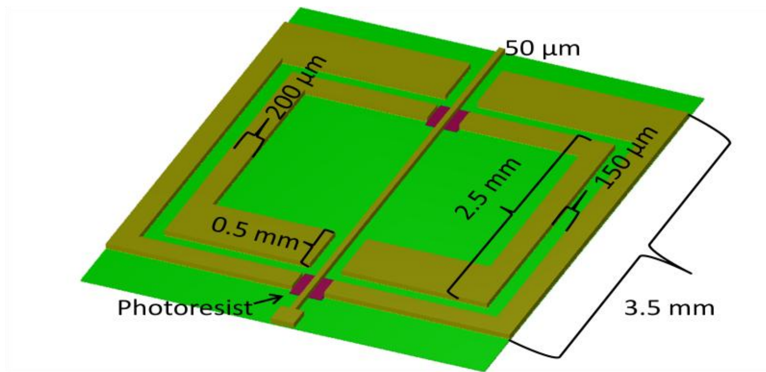

Figure 61. 6 – 8 GHz Meta-atom for testing in the 2-D Focused Beam System. Based on modeling and simulation, the meta-atom will resonate at 7 GHz.

www.manaraa.com

6.2.3. Future Work Summary

Based on the simulations and experimental results, areas of new research could definitely come out of this dissertation. The first area involves research into tunable designs based on changing inductance in the split ring resonator. Material that can change the induction parameter yet remain unaffected will be an avenue to investigate this tunable approach. The second area involves further research into active elements to compensate for loss at the resonant frequency. The initial look into the compensation of loss shows great potential for this research.

Finally, further work can be done for each step of the design process. Modeling different designs can contribute to building unique meta-atoms based on MEMS-based toolbox, capacitive and inductive elements, or active elements. Work in the fabrication of meta-atoms needs to continue in order to produce structures with wider tunable properties and deeper resonant nulls. Generating large area metamaterials to test in the 2-D Focused Beam will allow a broader range of testing not possible with the RF strip-line.

www.manaraa.com

Init.	Process Step: SRR Base Metal	Notes	Date Time
	INSPECT WAFER: ☐ Note any defects	**Start Date** **Start Time**	
	SOLVENT CLEAN WAFER: ☐ 20 sec acetone rinse at 500 rpm ☐ 20 sec methanol rinse at 500 rpm ☐ 20 sec isopropyl alcohol rinse at 500 rpm ☐ 20 sec deionized water rinse at 500 rpm ☐ Dry with nitrogen at 500 rpm ☐ Dry wafer with nitrogen on clean texwipes		
	DEHYDRATION BAKE: ☐ 2 min 110°C hot plate bake		
	SF-11 COAT: ☐ Flood wafer with SF-11 ☐ 4 sec spread at 500 rpm ☐ 30 sec spin at 4,000 rpm ☐ 2 min 200°C hot plate bake		
	1818 COAT: ☐ Flood wafer with 1818 ☐ 4 sec spread at 500 rpm ☐ 30 sec spin at 3,000 rpm ☐ 2 min 110°C hot plate bake ☐ Use acetone to remove 1818 on backside		
	EXPOSE 1818 WITH SRR MASK: ☐ No alignment for first level mask needed, however mask should be straight ☐ 8.0 sec exposure using EVG 620		
	1818 DEVELOP: ☐ 45 sec develop with 351:DI (1:5), flood wafer first, then use a spin/stop/spin/stop method at 500 rpm ☐ 30 sec DI water rinse at 500 rpm ☐ Dry with nitrogen at 500 rpm ☐ Dry wafer with nitrogen on clean texwipes		
	INSPECT RESIST: ☐ Inspect photoresist under microscope		
	EXPOSE SF-11 WITH DUV: ☐ Align to bottom metal alignment marks 200 sec exposure using DUV system		
	SF-11 DEVELOP: ☐ 2 min develop with nano-101 developer ☐ 30 sec DI water rinse at 500 rpm ☐ Dry with nitrogen at 500 rpm Dry wafer with nitrogen on clean texwipes		
	INSPECT RESIST: ☐ Inspect photoresist under microscope		
	ASHER DESCUM: ☐ 4 min, 75 W, O2 Barrel Asher		
	TENCOR MEASUREMENT: ☐ Measure photoresist step height T _______________ C _______________ B _______________		
	BOTTOM METAL DEPOSITION: ☐ Evaporate 200 Å Ti / 5500 Å Au with Figure 8 pattern at 4.8 kV, 30 mA		

المنارة للاستشارات
www.manaraa.com

	LIFT-OFF METAL: ☐ Heat 1165 remover to 90°C (set hot plate to 110°C) ☐ Tape liftoff or 30 min soak in acetone ☐ 5 – 10 min vibrobath in acetone ☐ 20 sec acetone rinse at 500 rpm ☐ 20 sec isopropyl alchol rinse at 500 rpm ☐ 20 sec DI water rinse at 500 rpm ☐ Dry with nitrogen at 500 rpm ☐ 5 min soak in 1165 at 90°C ☐ 20 sec DI rinse at 500 rpm ☐ Dry with nitrogen at 500 rpm ☐ Dry wafer with nitrogen on clean texwipes		
	INSPECT METAL: ☐ Inspect metal under microscope		
	ASHER DESCUM: ☐ 5 min, 75 W, O2 Barrel Asher		
	TENCOR MEASUREMENT: ☐ Measure metal step height T _______________ C _______________ B _______________		

المنارة للاستشارات
www.manaraa.com

Init.	Process Step: Electrode Base Metal	Notes	Date Time
	DEHYDRATION BAKE: ☐ 2 min 110°C hot plate bake	**Start Date** **Start Time**	
	SF-11 COAT: ☐ Flood wafer with SF-11 ☐ 4 sec spread at 500 rpm ☐ 30 sec spin at 4,000 rpm ☐ 2 min 200°C hot plate bake		
	1818 COAT: ☐ Flood wafer with 1818 ☐ 4 sec spread at 500 rpm ☐ 30 sec spin at 3,000 rpm ☐ 2 min 110°C hot plate bake ☐ Use acetone to remove 1818 on backside		
	EXPOSE 1818 WITH ELECTRODE MASK: ☐ Align to bottom metal alignment marks ☐ 8.0 sec exposure using EVG 620		
	1818 DEVELOP: ☐ 45 sec develop with 351:DI (1:5), flood wafer first, then use a spin/stop/spin/stop method at 500 rpm ☐ 30 sec DI water rinse at 500 rpm ☐ Dry with nitrogen at 500 rpm ☐ Dry wafer with nitrogen on clean texwipes		
	INSPECT RESIST: ☐ Inspect photoresist under microscope		
	EXPOSE SF-11 WITH DUV: ☐ 200 sec exposure using DUV system		
	SF-11 DEVELOP: ☐ 2 min develop with nano-101 developer ☐ 30 sec DI water rinse at 500 rpm ☐ Dry with nitrogen at 500 rpm Dry wafer with nitrogen on clean texwipes		
	INSPECT RESIST: ☐ Inspect photoresist under microscope		
	ASHER DESCUM: ☐ 5 min, 75 W, O2 Barrel Asher		
	TENCOR MEASUREMENT: ☐ Measure photoresist step height T _______________ C _______________ B _______________		
	BOTTOM METAL DEPOSITION: ☐ Evaporate 200 Å Ti / 4500 Å Au with Figure 8 pattern at 4.8 kV, 30 mA		
	LIFT-OFF METAL: ☐ Heat 1165 remover to 90°C (set hot plate to 110°C) ☐ Tape liftoff or 30 min soak in acetone ☐ 5 – 10 min vibrobath in acetone ☐ 20 sec acetone rinse at 500 rpm ☐ 20 sec isopropyl alcohol rinse at 500 rpm ☐ 20 sec DI water rinse at 500 rpm ☐ Dry with nitrogen at 500 rpm ☐ 5 min soak in 1165 at 90°C ☐ 20 sec DI rinse at 500 rpm ☐ Dry with nitrogen at 500 rpm ☐ Dry wafer with nitrogen on clean texwipes		
	INSPECT METAL: ☐ Inspect metal under microscope		

المنارة للاستشارات
www.manaraa.com

	ASHER DESCUM: ☐ 5 min, 75 W, O2 Barrel Asher		
	TENCOR MEASUREMENT: ☐ Measure metal step height T ________________ C ________________ B ________________		

المنارة للاستشارات

www.manaraa.com

Init.	Process Step: Dielectric Deposition	Notes	Date Time
	DIELECTRIC DEPOSITION: ☐ Deposit 3000 Å Si_3N_4 ☐ PECVD BLAH min, 167 sccm 5% Silane in N_2, 200 sccm N_2, 2.0 sccm NH_4, 60W, 800 mTorr, 600 sccm He, 300 °C	**Start Date** **Start Time**	
	INSPECT DIELECTRIC: ☐ Inspect dielectric under microscope and look for ○ Uniform color ○ Pin holes ○ Cracks around metal ○ Flaking		
	5214 COAT: ☐ Flood wafer with 5214 ☐ 4 sec spread at 500 rpm ☐ 30 sec spin at 4,000 rpm ☐ 1 min 110°C hot plate bake ☐ Use acetone to remove 5214 on backside		
	EXPOSE 5214 WITH DIELECTRIC MASK: ☐ Align to bottom metal alignment marks ☐ 1.5 sec exposure using EVG 620 ☐ 2 min 110°C hot plate bake ☐ 60 sec Flood Exposure to reverse image		
	5214 DEVELOP: ☐ 45 sec develop with 351:DI (1:5), flood wafer first, then use a spin/stop/spin/stop method at 500 rpm ☐ 30 sec DI water rinse at 500 rpm ☐ Dry with nitrogen at 500 rpm ☐ Dry wafer with nitrogen on clean texwipes		
	INSPECT RESIST: ☐ Inspect photoresist under microscope		
	ASHER DESCUM: ☐ 5 min, 75 W, LFE Barrel Asher		
	TENCOR MEASUREMENT: ☐ Measure photoresist step height T ________________ C ________________ B ________________		
	RIE DIELECTRIC: ☐ 4:40 min Plasma Therm 790 RIE Etch, 40-sccm CF_4, 3-sccm 10% O_2, at 50 mTorr, 100 W		
	INSPECT DIELECTRIC: ☐ Inspect dielectric removal under microscope		
	REMOVE 5214: ☐ 30 sec acetone rinse at 500 rpm ☐ 20 sec methanol rinse at 500 rpm ☐ 20 sec isopropyl alcohol rinse at 500 rpm ☐ Dry with nitrogen at 500 rpm ☐ Dry wafer with nitrogen on clean texwipes		
	INSPECT RESIST: ☐ Inspect under microscope for resist removal		
	ASHER DESCUM: ☐ 5 min, 75 W, LFE Barrel Asher		
	TENCOR MEASUREMENT: ☐ Measure metal step height T ________________ C ________________ B ________________		

www.manaraa.com

Init.	Process Step: Sacrificial Layer and Post	Notes	Date Time
	DEHYDRATION BAKE: ☐ 1 min 110°C hot plate bake	**Start Date** **Start Time**	
	FIRST SF-11 (PMGI) COAT: ☐ Flood wafer with SF-11 ☐ 4 sec spread at 500 rpm ☐ 30 sec spin at 3,000 rpm ☐ 5 min 270°C hot plate bake		
	SECOND SF-11 (PMGI) COAT: ☐ Flood wafer with SF-11 ☐ 4 sec spread at 500 rpm ☐ 30 sec spin at 3,000 rpm ☐ 5 min 270°C hot plate bake		
	1813 COAT: ☐ Flood wafer with 1813 ☐ 4 sec spread at 500 rpm ☐ 30 sec spin at 4,000 rpm ☐ 2 min 110°C hot plate bake ☐ Use acetone to remove 1813 on backside		
	EXPOSE 1813 WITH POST MASK: ☐ Align to bottom metal alignment marks ☐ 8.0 sec exposure using EVG 620		
	1813 DEVELOP: ☐ 40 sec develop with 351 (1:5), flood wafer first using *two* bottles, then use a spin/stop/spin/stop method at 500 rpm ☐ 30 sec DI water rinse at 500 rpm ☐ Dry with nitrogen at 500 rpm ☐ Dry wafer with nitrogen on clean texwipes		
	INSPECT RESIST: ☐ Inspect photoresist under microscope		
	TENCOR MEASUREMENT: ☐ Measure photoresist step height T _______________ C _______________ B _______________		
	FIRST DUV CYCLE (~1.5 µm / cycle): ☐ 200 sec DUV exposure @ 35 mW/cm^2, 254 nm		
	SF-11 DEVELOP: ☐ 60 sec bucket develop with SAL 101 ☐ 4x DI bucket rinse ☐ Dry wafer with nitrogen on clean texwipes		
	INSPECT RESIST: ☐ Inspect SF-11 under microscope, check for fringe patterns indicating residual SF-11		
	SECOND DUV CYCLE (~1.5 µm / cycle): ☐ 200 sec DUV exposure @ 35 mW/cm^2, 254 nm		
	SF-11 DEVELOP: ☐ 60 sec bucket develop with SAL 101 ☐ 4x DI bucket rinse ☐ Dry wafer with nitrogen on clean texwipes		
	INSPECT RESIST: ☐ Inspect SF-11 under microscope, check for fringe patterns indicating residual SF-11		

المنارة للاستشارات
www.manaraa.com

	TENCOR MEASUREMENT: ☐ Measure resist step height T _______________ C _______________ B _______________		
	REMOVE 1813: ☐ 30 sec acetone rinse at 500 rpm *Do not allow acetone to dry on SF-11 ☐ 30 sec methanol rinse at 500 rpm ☐ 30 sec isopropyl alcohol rinse at 500 rpm ☐ 10 sec DI rinse at 500 rpm ☐ Dry with nitrogen at 500 rpm ☐ Dry wafer with nitrogen on clean texwipes		
	INSPECT RESIST: ☐ Inspect photoresist for 1813 removal		
	ASHER DESCUM: ☐ 4 min, 150 W, LFE Barrel Asher		
	TENCOR MEASUREMENT: ☐ Measure SF-11 step height T _______________ C _______________ B _______________		
	POST REFLOW & INSPECT WAFER: ☐ 90 sec 250°C hot air oven bake **OR** ☐ 50 sec 270°C hot plate bake ☐ Inspect for resist reflow.		
	TENCOR MEASUREMENT: ☐ Measure SF-11 step height T _______________ C _______________ B _______________		
	HARD BAKE: ☐ Place in 90°C hot air oven 30 min before seed layer deposition ☐ Skip if reflow just completed and seed layer deposition immediately follows		

المنارة للاستشارات
www.manaraa.com

Init.	Process Step: Electroplate Beam and Release	Notes	Date Time
	SPUTTER SEED LAYER: ☐ Sputter 1000 Å Au using Discovery-18	**Start Date** **Start Time**	
	AZ 4620 COAT: ☐ Flood wafer with AZ 4620 ☐ 4 sec spread at 300 rpm ☐ 60 sec spin at 2,000 rpm ☐ 5 min 110°C hot plate bake		
	EXPOSE AZ 4620 WITH CANTILEVER MASK: ☐ Align to bottom metal alignment marks ☐ 50 sec exposure using EVG 620 (1000 mJ/cm^2 constant dose)		
	CLEAR PLATING CLIP AREAS: ☐ Use foil-mask clip template for 50 sec exposure		
	AZ 4620 DEVELOP: ☐ 3 min develop with AZ400K:DI (1:4) ○ Bucket develop using a beaker, agitate, but do not make liquid swirl, create waves parallel with beam ☐ 30 sec DI water rinse using one quick spin at 500 rpm (2 sec) then stop ☐ Dry with nitrogen at 500 rpm ☐ Dry wafer with nitrogen on clean texwipes		
	INSPECT RESIST: ☐ Inspect photoresist under microscope		
	WAFER EDGE PROTECT: ☐ Coat wafer edge with 1400-27 resist using swab ☐ Air dry with nitrogen ☐ Bake in 90°C oven for 30 min		
	ASHER DESCUM: ☐ 4 min, 150 W, LFE Barrel Asher		
	TENCOR MEASUREMENT: ☐ Measure photoresist step height T _______________ C _______________ B _______________		
	ELECTROPLATE CANTILEVER BEAMS: ☐ Plating conditions* : ○ Bath temp 58.5°C ○ Duty cycle 40-on/60-off (4 ms/6 ms) ○ Current density at 2.0 mA/cm^2 (0.02A, 1.0VDC) ○ Average current 12 mA ☐ Electroplate for 1.2 A-min		
	TENCOR MEASUREMENT: ☐ Measure electroplated step height Posts: T _______________ C _______________ B _______________ Beam End: T _______________ C _______________ B _______________ ☐ Repeat electroplating step if needed		

المنارة للاستشارات
www.manaraa.com

	REMOVE AZ 4620: ☐ 30 sec acetone rinse at 500 rpm ☐ 30 sec methanol rinse at 500 rpm ☐ 30 sec isopropyl alcohol rinse at 500 rpm ☐ 30 sec DI rinse at 500 rpm ☐ Dry with nitrogen at 500 rpm ☐ Dry wafer with nitrogen on clean texwipes		
	ASHER DESCUM: ☐ 5 min, 75 W, LFE Barrel Asher		
	SEED LAYER ETCH: ☐ 30 sec KI etch ☐ 4x DI bucket rinse ☐ Dry with nitrogen on clean texwipes		
	INSPECT RESIST: ☐ Make sure seed layer is completely removed		
	TENCOR MEASUREMENT: ☐ Measure electroplated step height Posts: T _______________ C _______________ B _______________ Beam End: T _______________ C _______________ B _______________ ☐ Update plating database		
	AZ 4620 RE-COAT FOR DICING: ☐ Flood wafer with AZ 4620 ☐ 4 sec spread at 300 rpm ☐ 60 sec spin at 3,000 rpm ☐ 5 min 110°C hot plate bake		
	WAFER DICING: ☐ Dice wafer at AFRL/RYD ☐ Create a cutting map in L-edit for dicing technician ☐ Sections must fit in CO_2 Dryer		
	REMOVE AZ 4620: ☐ 30 sec acetone rinse at 500 rpm ☐ 30 sec methanol rinse at 500 rpm ☐ 30 sec isopropyl alcohol rinse at 500 rpm ☐ 30 sec DI rinse at 500 rpm ☐ Dry with nitrogen at 500 rpm ☐ Dry wafer with nitrogen on clean texwipes		
	ASHER DESCUM: ☐ 10 min, 75 W, LFE Barrel Asher		
	STRIP SF-11 SACRIFICIAL LAYER (RELEASE PROCESS): ☐ Do NOT vibrobath devices ☐ Heat 1165 remover to 90°C (set hot plate to 110°C) ☐ 30 min soak in 1165 at 90°C ☐ Wet transfer from 1165 beaker to 1st IPA in petri dish, 30 sec soak ☐ Wet transfer to 2nd IPA in petri dish, 30 sec soak ☐ Wet transfer to 3rd IPA in petri dish, 30 sec soak ☐ Wet transfer to 4th IPA in petri dish, 30 sec soak ☐ Wet transfer to 1st methanol in petri dish, 30 sec soak ☐ Wet transfer to 2nd methanol in petri dish, 30 sec soak ☐ Wet transfer to 3rd methanol in petri dish, 30 sec soak ☐ Wet transfer to 4th methanol in petri dish, 30 sec soak ☐ Fill CO^2 dryer chamber with enough methanol to cover the wafer. ☐ Remove wafer from 4th methanol dish and place in CO^2 dryer chamber. ☐ Immediately cover CO^2 dryer and start process		
	ASHER DESCUM: ☐ 30 min, 75 W, LFE Barrel Asher		

المنارة للاستشارات
www.manaraa.com

```
% MATLAB m-file used to plot the transmission magnitude for the Intra-ring
% Capacitance on Meta-atom designs.
% Measurements were performed on 2 June 2011.


function Output = AFITSRRStripline02Jun2011__DL(varargin)
%% Setup
tic
CurrentDir = cd;

if nargin < 1
   P = 1;
   close all
   clc
else
   P = 0;
end


%% Sample 00: RF Stripline, Calibration and Gating
if exist('E:\AFIT PhD Program\MetaMaterials','dir') == 7
   cd('E:\AFIT PhD Program\MetaMaterials\RF Metamaterial\LORE_Lab_PNA_data\02
Jun2011\Sample00')
else
   disp('Data is missing for Measurements.')
end

filename_sample00 = ...
   ['Calibration_Gated.cti'];

for ii = 1:size(filename_sample00,1)
   [~, S21_sample00(ii,:),~, ~, Freq] = ...
      citi2s(filename_sample00(ii,:), 2);
end

Output.S21_Sample00 = S21_sample00;
Output.Freq_Sample00 = Freq*10^6;

MagS21_sample00 = abs(S21_sample00);

% Plotting for sample 00
if P == 1
   figure (1)
   plot(Output.Freq_Sample00*10^-9, MagS21_sample00);%([1, 11],:)use to select voltage trace
   ylabel('Transmission (S_{21}) - Magnitude ', 'fontsize', 14, 'FontName','Times New Roman',...
      'FontWeight','demi')
   xlabel('Frequency (GHz) ', 'fontsize', 14, 'FontName','Times New Roman',...
      'FontWeight','demi')
   %axis([1 2.0 0.80 1.1])
   grid on
%     title('Transmision (S21) - Capacitor Layout A', 'fontsize', 16)
   legend(filename_sample00(:,1:11), 'location', 'NorthWest');%[1, 11]use to select voltage trace
```


www.manaraa.com

```
    %saveas(gcf, 'LayoutD.png')
    %saveas(gcf, 'LayoutD.fig')
    %axis([0.5 3.5 0.7 1])
    %legend(filename_sample02(:,1:3), 'location', 'SouthEast')
    %saveas(gcf, 'LayoutD_zoom.png')
    %saveas(gcf, 'LayoutD_zoom.fig')
end

%% Sample 02: Capacitor Layout D
if exist('E:\AFIT PhD Program\MetaMaterials','dir') == 7
    cd('E:\AFIT PhD Program\MetaMaterials\RF Metamaterial\LORE_Lab_PNA_data\02
Jun2011\Sample02')
else
    disp('Data is missing for Measurements.')
end

filename_sample02 = ...
    ['LayoutD_1_00VDC.cti';'LayoutD_1_05VDC.cti';'LayoutD_1_10VDC.cti';...
    'LayoutD_1_15VDC.cti';'LayoutD_1_20VDC.cti';'LayoutD_1_30VDC.cti';'LayoutD_1_40VDC.cti';...
    'LayoutD_1_50VDC.cti';'LayoutD_1_60VDC.cti';'LayoutD_1_70VDC.cti';...
    'LayoutD_1_80VDC.cti'];

for ii = 1:size(filename_sample02,1)
    [~, S21_sample02(ii,:),~, ~, Freq] = ...
        citi2s(filename_sample02(ii,:), 2);
end

Output.S21_Sample02 = S21_sample02;
Output.Freq_Sample02 = Freq*10^6;

MagS21_sample02 = abs(S21_sample02);

% Plotting for sample 02
if P == 1
    figure2 = figure(2);

% Create axes
axes2 = axes('Parent',figure2,...
    'XTickLabel',{'0.2','0.4','0.6','0.8','1','1.2','1.4','1.52','1.8','2'},...
    'XTick',[0.2 0.4 0.6 0.8 1 1.2 1.4 1.52 1.8 2],...
    'Position',[0.106194690265487 0.166666666666667 0.744346116027532 0.758333333333333]);
    grid(axes2,'on');
    hold(axes2,'all');

    plot(Output.Freq_Sample02*10^-9, MagS21_sample02([1, 5, 7, 9, 11],:), 'Marker','+');%use to select
voltage trace
    plot(Output.Freq_Sample00*10^-9, MagS21_sample00,'b-');
    ylabel('Transmission (S_{21}) - Magnitude ', 'fontsize', 14, 'FontName','Times New Roman',...
        'FontWeight','demi')
    xlabel('Frequency (GHz) ', 'fontsize', 14, 'FontName','Times New Roman',...
        'FontWeight','demi')

    axis([.1 2 0.84 1.06])
    %grid on
```


المنارة للاستشارات
www.manaraa.com

```
%     title('Transmision (S21) - Capacitor Layout A', 'fontsize', 16)
    legend(filename_sample02([1, 5, 7, 9, 11],11:15), 'location', 'NorthEastOutside');%[1, 11]use to select
voltage trace
    hold off
    %saveas(gcf, 'LayoutD.png')
    %saveas(gcf, 'LayoutD.fig')
    %axis([0.5 3.5 0.7 1])
    %legend(filename_sample02(:,1:3), 'location', 'SouthEast')
    %saveas(gcf, 'LayoutD_zoom.png')
    %saveas(gcf, 'LayoutD_zoom.fig')
end


%% Sample 04: Capacitor Layout C with one array
if exist('E:\AFIT PhD Program\MetaMaterials','dir') == 7
    cd('E:\AFIT PhD Program\MetaMaterials\RF Metamaterial\LORE_Lab_PNA_data\02
Jun2011\Sample04')
else
    disp('Data is missing for Measurements.')
end

filename_sample04 = ...
    ['LayoutC_1_00VDC.cti';'LayoutC_1_10VDC.cti';...
    'LayoutC_1_20VDC.cti';'LayoutC_1_30VDC.cti';'LayoutC_1_40VDC.cti';...
    'LayoutC_1_50VDC.cti';'LayoutC_1_55VDC.cti';'LayoutC_1_60VDC.cti';...
    'LayoutC_1_65VDC.cti';'LayoutC_1_70VDC.cti'];

for ii = 1:size(filename_sample04,1)
    [~, S21_sample04(ii,:),~, ~, Freq] = ...
        citi2s(filename_sample04(ii,:), 2);
end

Output.S21_Sample04 = S21_sample04;
Output.Freq_Sample04 = Freq*10^6;

MagS21_sample04 = abs(S21_sample04);

% Plotting for sample 04
if P == 1
    figure4 = figure(4);

% Create axes
axes4 = axes('Parent',figure4,...
    'XTickLabel',{'0.2','0.4','0.6','0.8','1','1.2','1.4','1.6','1.76','2'},...
    'XTick',[0.2 0.4 0.6 0.8 1 1.2 1.4 1.6 1.76 2],...
    'Position',[0.106194690265487 0.166666666666667 0.744346116027532 0.758333333333333]);
    grid(axes4,'on');
    hold(axes4,'all');

    plot(Output.Freq_Sample04*10^-9, MagS21_sample04([1, 6, 8, 9, 10],:), 'Marker','+');%use to select
voltage trace
    plot(Output.Freq_Sample00*10^-9, MagS21_sample00,'b-');
    ylabel('Transmission (S_{21}) - Magnitude ', 'fontsize', 14, 'FontName','Times New Roman',...
        'FontWeight','demi')
```


المنارة للاستشارات
www.manaraa.com

```
    xlabel('Frequency (GHz) ', 'fontsize', 14, 'FontName','Times New Roman',...
        'FontWeight','demi')
    axis([.1 2.0 0.84 1.06])

%     title('Transmision (S21) - Capacitor Layout A', 'fontsize', 16)
    legend(filename_sample04([1, 6, 8, 9, 10],11:15), 'location', 'NorthEastOutside');%[1, 11]use to select
voltage trace
    hold off
    %saveas(gcf, 'LayoutD.png')
    %saveas(gcf, 'LayoutD.fig')
    %axis([0.5 3.5 0.7 1])
    %legend(filename_sample02(:,1:3), 'location', 'SouthEast')
    %saveas(gcf, 'LayoutD_zoom.png')
    %saveas(gcf, 'LayoutD_zoom.fig')
end
```


www.manaraa.com

```
% Output (struct) = AFITSRRStriplineInductor__DL_Dissertation_File_24Oct11(varargin)
% This function plots S parameters measured during
% stripline measurements made on 17 Dec 10. The measurements were of
% the AFIT SRR with with addtional metal in the outer SRR. The resonance
% frequencies are expected around 2.5 GHz.
% This file saves the output pictures and figures to the appropriate
% progress report folder.
% Optional: To not plot anything and only return the S-paramaters and Freq,
% supply an argument.

function Output = AFITSRRStriplineInductor__DL_Dissertation_File_24Oct11(varargin)
%% Setup
tic
CurrentDir = cd;

if nargin < 1
    P = 1;
    close all
    clc
else
    P = 0;
end

if exist('E:\AFIT PhD Program\MetaMaterials','dir') == 7
    cd('E:\AFIT PhD Program\MetaMaterials\RF Metamaterial\LORE_Lab_PNA_data')
else
    disp('Data is missing for Measurements.')
end
%% Input Data
StartDir = cd;
DirectoryInfo= dir('*Inductor_data*'); %[1 5:12 2:4]

%label = [{'Coil B-Trans'},{'Coil B-Reflection'}];

for ii = 1:size(DirectoryInfo,1)
    cd(['./' DirectoryInfo(ii).name])

    info = dir('*.cti');

    for jj = 1:size(info,1)
        [Output.S11(ii,jj,:),Output.S12(ii,jj,:),Output.S21(ii,jj,:),Output.S22(ii,jj,:), Freq] = ...
            citi2s(info(jj).name, 2);
    end

    Output.Freq = transpose(Freq*10^6);

   cd(StartDir)
end

%ImpedanceDL = (((1 + Output.S11).^2) - (Output.S21).^2)./(((1 - Output.S11).^2) - (Output.S21).^2);

Output.S11 = squeeze(Output.S11);
Output.S12 = squeeze(Output.S12);
Output.S21 = squeeze(Output.S21);
```


المنارة للاستشارات
www.manaraa.com

```
Output.S22 = squeeze(Output.S22);

%% S-parameter measurements for the samples
%
if P == 1

    figure(1)
    hold on
    subplot(221)
    plot(Output.Freq*10^-9, real(Output.S11), '-o', 'linewidth', 1.0)%([1:4],:)
    legend('Re(S_{11})','location', 'northeast')
    grid on
    %axis([0 4 1 -1])
    subplot(222)
    plot(Output.Freq*10^-9, imag(Output.S11), '-*', 'linewidth',1.0)%([1:4],:)
    legend('Im(S_{11})','location', 'northeast')
    grid on
    subplot(223)
    plot(Output.Freq*10^-9, real(Output.S21), '-.', 'linewidth', 2.0)%([1:4],:)
    legend('Re(S_{21})','location', 'northeast')
    grid on
    subplot(224)
    plot(Output.Freq*10^-9, imag(Output.S21), '--', 'linewidth',2.0)%([1:4],:)
    legend('Im(S_{21})','location', 'northeast')
    grid on

end

%% Calculating Impedance at each Frequency
% Obtained from Physics and applications of negative refractive index
% materials
Impedance = (+1)*sqrt((((1 + Output.S11).^2) - (Output.S21).^2)./(((1 - Output.S11).^2) -
(Output.S21).^2));%page 46

figure(2)
hold on
plot(Output.Freq*10^-9, imag(Impedance), '-o', 'linewidth', 1.0);
plot(Output.Freq*10^-9, real(Impedance), '-*', 'linewidth', 1.0);
hold off
%Change Impedance to match a passive medium for the SRR based on Jason
%Paul, Xudong Chen and D. R. Smith
for mmm = 1 : size(Impedance)
    for mm = 1 : length(Impedance)
        if real(Impedance(mmm,mm)) < 0 && imag(Impedance(mmm,mm)) > 0
            Impedance_prime(mmm,mm,1) = -real(Impedance(mmm,mm)) - 1i*imag(Impedance(mmm,mm));
        elseif  real(Impedance(mmm,mm)) > 0 && imag(Impedance(mmm,mm)) > 0
                Impedance_prime(mmm,mm,1) = real(Impedance(mmm,mm)) -
1i*imag(Impedance(mmm,mm));
        elseif  real(Impedance(mmm,mm)) < 0 && imag(Impedance(mmm,mm)) < 0
            Impedance_prime(mmm,mm) = -real(Impedance(mmm,mm)) - 1i*imag(Impedance(mmm,mm));
        else
            Impedance_prime(mmm,mm) = Impedance(mmm,mm);
        end
    end
```


المنارة للاستشارات
www.manaraa.com

```
end
figure(3)
hold on
subplot(2,1,1)
%plot(Output.Freq*10^-9, real(Impedance_negative), '-r', 'linewidth', 1.0);
plot(Output.Freq*10^-9, imag(Impedance_prime), '-o', 'linewidth', 1.0);
xlabel('Frequency (GHz)', 'fontsize',14)
ylabel('Imaginary Impedance', 'fontsize', 14)
legend([{'Imaginary'}],'location', 'southeast', 'fontsize', 14)
subplot(2,1,2)
%plot(Output.Freq*10^-9, real(Impedance_positive), '-rp', 'linewidth', 1.0);
plot(Output.Freq*10^-9, real(Impedance_prime), '-*', 'linewidth', 1.0);
grid on
%plot(Output.Freq*10^-9, real(Impedance_prime), '-r', 'linewidth', 1.0);
%plot(Output.Freq*10^-9, imag(Impedance_prime), '-o', 'linewidth', 1.0);
xlabel('Frequency (GHz)', 'fontsize',14, 'FontName','Times New Roman',...
'FontWeight','demi')
ylabel('Real Impedance', 'fontsize', 14,'FontName','Times New Roman',...
'FontWeight','demi')
legend([{'Real'}],'location', 'southeast', 'fontsize', 14,'FontName','Times New Roman',...
'FontWeight','demi')
hold off%Calculating the half-space reflection coefficient
Reflection_01 = (Impedance_prime - 1)./(Impedance_prime + 1); %page 46
% figure(4)
% plot(Output.Freq*10^-9, abs(transpose(Reflection_01)), 'p', 'linewidth', 1.0);
%X = (1 - ((Output.S22).^2) + ((Output.S21).^2))./(2.*Output.S21); %page46
%X = 1./((2.*Output.S21).*(1 - ((Output.S11).^2) + ((Output.S21).^2)));
%Robust method_Chen Phy Rev E 70, 016608(2004)
%step1_exp = X + 1i*(1 - X.^2).^0.5;
%step2_exp = X - 1i*(1 - X.^2).^0.5;
m = 0; %page47
uo = 4*pi*10^(-7);
eo = 8.854*10^(-12);
k0 = transpose((2*pi*Output.Freq)*sqrt(uo*eo)); %find
d_length = 0.012;%0.045; %4*0.016962; %length of SRR array stripline (meters)

for mnn = 1 : size(Output.S21)
   index_n(mnn,:) = (-1)*(1./(k0.*d_length)).*(acos((1./(2.*Output.S21(mnn,:))).*(1-
(((Output.S11(mnn,:)).^2)-((Output.S21(mnn,:)).^2)))));
   %the index must be inspected to have positive imaginary values; + or - must be added to index
end

figure(11)
hold on
plot(Output.Freq*10^-9, imag(index_n(1,:)), '-o', 'linewidth', 1.0);
plot(Output.Freq*10^-9, real(index_n(1,:)), '-r*', 'linewidth', 1.0);
axis([1.5 3.5 -1.8 1.8])
grid on
hold off

for mnnn = 1 : size(Output.S21)
   for mn = 1 : length(index_n)
      if imag(index_n(mnnn,mn)) < 0
         index_n_prime1(mnnn,mn) = real(index_n(mnnn,mn))*0 - 1i*imag(index_n(mnnn,mn));
```


www.manaraa.com

```
        else
            index_n_prime1(mnnn,mn) = index_n(mnnn,mn);
        end
        if imag(index_n_prime1(mnnn,mn)) < 0.1486 && real(index_n_prime1(mnnn,mn)) > -0.52
            index_n_prime(mnnn,mn) = real(index_n_prime1(mnnn,mn))*0 +
1i*imag(index_n_prime1(mnnn,mn));
        else
            index_n_prime(mnnn,mn) = index_n_prime1(mnnn,mn);
        end
    end
end
%

figure (5)
    for mo = 1%:size(index_n_prime)
        hold on
        plot(Output.Freq*10^-9, imag(index_n_prime(mo,:)), '-o','Color', [.5 .25*mo .25*mo], 'linewidth',
1.0)%
        plot(Output.Freq*10^-9, real(index_n_prime(mo,:)), '-*', 'Color', [.5 .25*mo .25*mo],'linewidth', 1.5)
%

        hold off
    end
    %axis([3 4.5 -.1 2])
    grid on
    box on
    xlabel('Frequency (GHz)', 'fontsize',14,'FontName','Times New Roman',...
'FontWeight','demi')
    ylabel('Imaginary and real refractive index', 'fontsize', 14,'FontName','Times New Roman',...
'FontWeight','demi')
    legend([{'Imaginary'},{'Real'}],'location', 'northeast', 'fontsize', 14,'FontName','Times New Roman',...
'FontWeight','demi')
    %saveas(gcf,'Refractive_Index_Baseline_Ex.png')
    %saveas(gcf,'RefractiveIndex_Baseline_Ex.fig')
    %saveas(gcf,'Refractive_Index_Baseline_Ex.bmp')
permeability_relative = index_n_prime.*Impedance_prime;
permittivity_relative = index_n_prime./Impedance_prime;

figure (6)
    for mo = 1:size(index_n_prime)
    hold on
    plot(Output.Freq*10^-9, real(permeability_relative(mo,:)), '-co','Color', [.75 .25*mo .25*mo], 'linewidth',
1.0)%(1,:)
    hold off
    end
    grid on
    box on
    xlabel('Frequency (GHz)', 'fontsize',14,'FontName','Times New Roman',...
'FontWeight','demi')
    ylabel('Imaginary and Real Permeability', 'fontsize', 14,'FontName','Times New Roman',...
'FontWeight','demi')
    %legend([{'Baseline Re(\mu)'},{'Coil A Re(\mu)'},{'Coil B Re(\mu)'},{'Coil C Re(\mu)'}],'location',
'southeast')
    legend([{'Baseline Re(\mu)'},{'Baseline Im(\mu)'}],'location', 'southeast', 'fontsize', 14)
```


المنارة للاستشارات
www.manaraa.com

```
   %saveas(gcf,'Permeability_Baseline_Ex.png')
   %saveas(gcf,'Permeability_Baseline_Ex.fig')
   %saveas(gcf,'Permeability_Baseline_Ex.bmp')


figure (7)
   for mo = 1:size(index_n_prime)
   hold on
   %plot(Output.Freq*10^-9, permeability, 'gp', 'linewidth', 1.0)
   plot(Output.Freq*10^-9, real(permittivity_relative(mo,:)), '-co','Color', [.75 .25*mo .25*mo], 'linewidth',
1.0)%
   hold off
   end
   grid on
   box on
   xlabel('Frequency (GHz)', 'fontsize',14,'FontName','Times New Roman',...
'FontWeight','demi')
   ylabel('Imaginary and Real Permittivity', 'fontsize', 14,'FontName','Times New Roman',...
'FontWeight','demi')
   legend([{'Baseline Re(\epsilon)'},{'Baseline Im(\epsilon)'}],'location',...
      'southeast', 'fontsize', 14,'FontName','Times New Roman',...
'FontWeight','demi')

   %saveas(gcf,'permittivity_Baseline_Ex.png')
   %saveas(gcf,'permittivity_Baseline_Ex.fig')
   %saveas(gcf,'permittivity_Baseline_Ex.bmp')

figure (10)
   for mo = 1:size(index_n_prime)
      hold on
      plot(Output.Freq*10^-9, imag(index_n_prime(mo,:)), '-o', 'Color', ...
         [.75 .25*mo .25*mo], 'linewidth', 1.0)%'Color', [.5 .25*mo .25*mo],
      plot(Output.Freq*10^-9, real(index_n_prime(mo,:)), '-r*', 'Color', ...
         [.5 .25*mo .25*mo], 'linewidth', 1.5) %'Color', [.5 .25*mo .25*mo]

      hold off
   end
   %axis([3 4.5 -.1 2])
   grid on
   box on
   xlabel('Frequency (GHz)', 'fontsize',14,'FontName','Times New Roman',...
'FontWeight','demi')
   ylabel('Imaginary and real refractive index', 'fontsize', 14,'FontName','Times New Roman',...
'FontWeight','demi')
   legend([{'Imaginary'},{'Real'}],'location', 'southeast', 'fontsize', 14,'FontName','Times New Roman',...
'FontWeight','demi')
   %saveas(gcf,'Refractive_Index_Loop_A_Ex.png')
   %saveas(gcf,'RefractiveIndex_Loop_A_Ex.fig')
   %saveas(gcf,'Refractive_Index_Loop_A_Ex.bmp')

figure (12)
   for mo = 1
      hold on
```


المنارة للاستشارات
www.manaraa.com

```
        plot(Output.Freq*10^-9, real(index_n_prime(mo,:)), '-ro', 'linewidth', 1.5) %'Color', [.5 .25*mo
.25*mo]
        plot(Output.Freq*10^-9, imag(index_n_prime(mo,:)), '-*', 'linewidth', 1.0)%'Color', [.5 .25*mo
.25*mo],
        hold off
    end
    axis([1.5 3.5 -2.5 2.5])
    grid on
    box on
    xlabel('Frequency (GHz)', 'fontsize',14, 'fontname', 'times new roman', 'FontWeight','bold')
    ylabel('Imaginary and real refractive index', 'fontsize', 14, 'fontname', 'times new roman',
'FontWeight','bold')
    legend([{'Real'},{'Imaginary'}],'location', 'northeast', 'fontsize', 14, 'fontname', 'times new roman',
'FontWeight','bold')
    %saveas(gcf,'Refractive_Index_Baseline_Ex.png')
    %saveas(gcf,'RefractiveIndex_Baseline_Ex.fig')
    %saveas(gcf,'Refractive_Index_Baseline_Ex.bmp')

    figure (13)
    for mo = [2]%:size(index_n_prime)
        hold on
        plot(Output.Freq*10^-9, real(index_n_prime(mo,:)), '-ro', 'linewidth', 1.0)%'Color', [.5 .25*mo
.25*mo],
        plot(Output.Freq*10^-9, imag(index_n_prime(mo,:)), '-*', 'linewidth', 1.5) %'Color', [.5 .25*mo
.25*mo]

        hold off
    end
    axis([1.5 3.5 -2.5 2.5])%[1.5 3.5 -.1 .48]
    grid on
    box on
    xlabel('Frequency (GHz)', 'fontsize',14, 'fontname', 'times new roman', 'FontWeight','bold')
    ylabel('Imaginary and real refractive index', 'fontsize', 14, 'fontname', 'times new roman',
'FontWeight','bold')
    legend([{'Real'}, {'Imaginary'}],'location', 'northeast', 'fontsize', 14, 'fontname', 'times new roman',
'FontWeight','bold')
    %saveas(gcf,'Refractive_Index_Loop_A_Ex.png')
    %saveas(gcf,'RefractiveIndex_Loop_A_Ex.fig')
    %saveas(gcf,'Refractive_Index_Loop_A_Ex.bmp')

    figure (14)
    for mo = [3]%:size(index_n_prime)
        hold on
        plot(Output.Freq*10^-9, real(index_n_prime(mo,:)), '-ro', 'linewidth', 1.0)%'Color', [.5 .25*mo
.25*mo],
        plot(Output.Freq*10^-9, imag(index_n_prime(mo,:)), '-*', 'linewidth', 1.5) %'Color', [.5 .25*mo
.25*mo]

        hold off
    end
    axis([1.5 3.5 -2.5 2.5])%[1.5 3.5 -.1 .48]
    grid on
    box on
    xlabel('Frequency (GHz)', 'fontsize',14, 'fontname', 'times new roman', 'FontWeight','bold')
```


المنارة للاستشارات
www.manaraa.com

```
    ylabel('Imaginary and real refractive index', 'fontsize', 14, 'fontname', 'times new roman',
'FontWeight','bold')
    legend([{'Real'}, {'Imaginary'}],'location', 'northeast', 'fontsize', 14, 'fontname', 'times new roman',
'FontWeight','bold')
    %saveas(gcf,'Refractive_Index_Loop_B_Ex.png')
    %saveas(gcf,'RefractiveIndex_Loop_B_Ex.fig')
    %saveas(gcf,'Refractive_Index_Loop_B_Ex.bmp')
%% Wrap-up
cd(CurrentDir)
toc
```


المنارة للاستشارات
www.manaraa.com

Appendix C. Investigation of Terahertz Metamaterials

RF meta-atoms are the main focus of my dissertation. The theory and concept that are used in designing the RF meta-atom can also be used at higher frequencies. In this section, a brief investigation into terahertz metamaterials is reported based on the additional work completed on metamaterials.

Terahertz includes the 50 GHz to 10 THz frequency range. Research in the terahertz range concentrates on communication, inspections, medical imaging, security, scientific imaging. Metamaterials can help in all these research areas by tailoring the refractive index. An intital investigation conducted on terahertz is discussed in the following subsections which covers background information, simulation and testing for a polyMUMPS ® terahertz metamaterial design.

Appendix C.1. PolyMUMPS ® Terahertz Metamaterial Structure Background

Terahertz metamaterial consists of split ring resonators that interact with the electric and magnetic fields impinging on the structures. The initial scope of this research is to investigate a fabrication technique to produce an array of terahertz metamaterial that produces a resonance at a defined frequency [72], [73]. Using a foundry process set up for fabrication of microelectromechanical systems, a novel approach for the fabrication of terahertz metamaterials is produced utilizing polyMUMPS ®.

Through scaling of the resonators, metamaterials that function in the infrared and the radio frequency range of the electromagnetic spectrum have been demonstrated [74], [75]. Recently, strides have been made to develop metamaterials in the terahertz regime since most natural materials do not have a response to THz radiation. The lack of natural

المنارة للاستشارات
www.manaraa.com

materials has created what is known as the THz gap. Metamaterials tailored towards THz frequencies provide a means for developing THz devices. For THz generation, resonator structures need to be fabricated with dimensions on the order of 30 μm.

The aforementioned THz gap covers from 100 GHz to 4 THz of the electromagnetic spectrum, which lies just above microwaves and below infrared waves. Developing THz technology has been on the forefront of research as scientists try to close this gap. Thus far, development of THz sources and detectors has resulted in THz imagers, semiconductor characterization, and new methods for chemical and biological sensing [76]. Many THz applications (communications, security, imaging, and chemical and biological sensing) have been identified and are currently being researched [77]. However, there is still a great deal of advancement required to fully exploit this region of the electromagnetic spectrum. These applications would undoubtedly benefit from materials that enhance our ability to manipulate, control, and detect THz radiation.

Metamaterials have played an increasingly important role in the development of THz devices [9]. For instance, planar arrays fabricated on various semiconductor and insulator substrates have shown a response to THz radiation both electrically [76], [78] and magnetically [79], [80]. Based on current research, metamaterials are ideal candidates for THz devices because they can be scaled and show a resonant frequency response that can be tunable by the design. Metamaterial-based devices include filters, modulators, amplifiers, transistors, and resonators [81].

The design for the SRRs was initially laid out in L-Edit ©, a subset circuit layout editor program of the MEMS Pro software program suite, the design is based on MatLab® calculations to determine the resonant frequency considering the design

المنارة للاستشارات
www.manaraa.com

parameters. Once the design was complete it was transferred to polyMUMPS® foundry which then fabricated the devices given our design specifications.

The dimensions of the single split ring resonators were chosen to support a resonant frequency of approximately 5 THz. A layout of the SRR structures and its dimensions are shown in Figure 62. The SRRs have a square shape with a height and length of 40 µm. The width of the trace is 10 µm on all sides. The resonator gap opening is 17 µm, such that the length of the trace on either side of the gap is 11.5 µm.

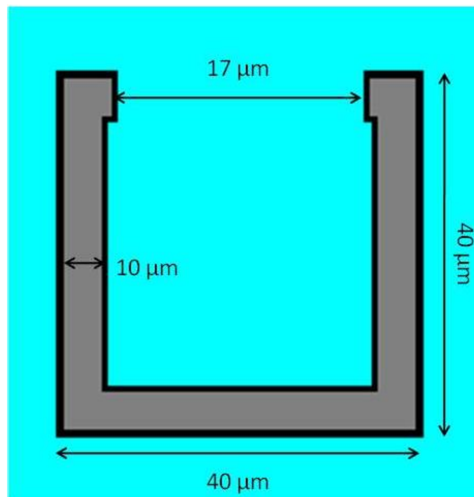

Figure 62. A schematic of a top down view of a single unit SRR with the dimensions indicated.

The SRR structures were laid out such that there were four to a unit cell as shown in Figure 63. The lattice period is 80 µm. The polyMUMPS ® structures were arrayed to cover a 1 cm^2 area.

www.manaraa.com

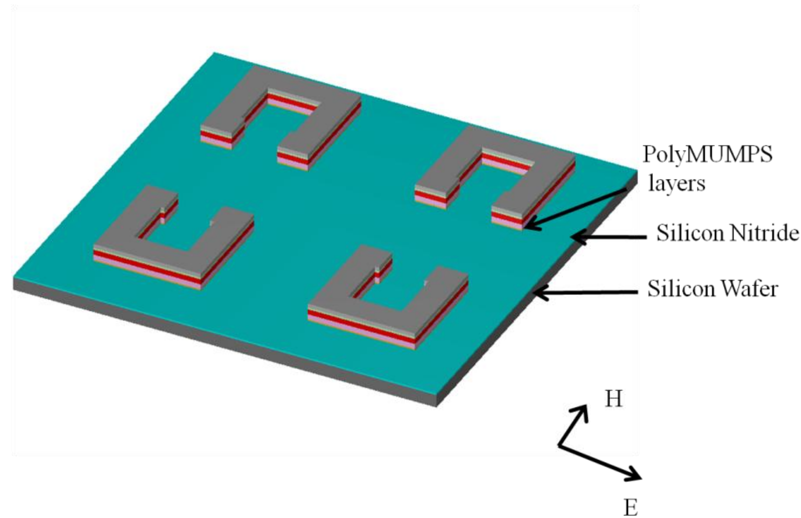

Figure 63. 3D Diagram of a unit cell of the patterned metamaterial shows the three polysilicon and two silicon dioxide alternating layers grown on a silicon wafer with a thin silicon nitride buffer layer.

MatLab® code was written to aid in selecting the SRR dimensions. The dimensions of the SRR are determined by first deciding on a target resonant frequency. The main two contributing factors to the resonance are the structure's inductance and capacitance, as shown in this resonant equation.

$$\omega_0 \approx \frac{1}{\sqrt{LC}} \tag{47}$$

where L in the inductance from the metal trace and C is the overall capacitance , however since the gap is the dominating source of capacitance only that capacitance is considered. The inductance of the trace and the gap capacitance are given by

$$L = \mu_0 \frac{l^2}{t} \tag{48}$$

$$C = \varepsilon_0 \varepsilon_r \frac{Area}{g} \tag{49}$$

المنارة للاستشارات
www.manaraa.com

where μ_0 is the vacuum permeability, l is the length of the side of the SRR, t is the thickness of the material, ε_0 is the permittivity of free space, ε_r is relative permittivity, A is the surface area of the trace, and g is the gap separation. Note the resonant frequency is not a function of the sample thickness. The parameter having the most effect on the resonant frequency will be the length of the SRR, which has a linear relationship with the resonant frequency. The resonance will be inversely proportional to the gap separation and proportional to the square root of the width of the trace and the relative dielectric constant. While these parameters still affect the resonant frequency, their contributions are not as strong as that of altering the size of the SRR.

The SRRs for this study are fabricated with the polyMUMPS ® process [17] which uses polysilicon and silicon dioxide in alternating layers. The polysilicon layers acts as a metallic structure and the silicon dioxide layers are used as a dielectric. These materials are chosen due to the high plasma frequency of the polysilicon and the dielectric constant of the silicon dioxide. The polyMUMPS® samples consist of alternating polysilicon and silicon dioxide layers grown on top of a single side polished crystalline silicon wafer with a small nitride buffer layer, as shown in Figure 64. At the foundry, the alternating layers are capped with a thin layer of chromium followed by a thin layer of gold. The layout of the material layers along with each layer's thickness is shown in Figure 64. The gold and chromium layers are removed with a wet etch prior to the metamaterial testing. A detailed review of the polyMUMPS ® fabrication process can be found on their website [49].

المنارة للاستشارات
www.manaraa.com

Figure 64. A schematic illustrating the layers and their corresponding dimensions used in the polyMUMPS ® process.

Appendix C.2. Simulation for polyMUMPS ® Terahertz Metamaterial Structures

Using the layout generated with L-Edit, simulations are performed on the SRR shown in Figure 62 to obtain the capacitance and inductance for the structure. CoventorWare ® provides the simulation tools necessary to obtain the values. The layout is imported into CoventorWare ® using the GDS-II 2-D layout format converted to CAT 2-D layout format and compiled into a finite element model. Using the finite element model, the simulation determines the capacitance using the electrostatic analysis, which simulates an electric field on the conductors and calculates the charge density. Using the charge density, the capacitance of the model for each component is calculated. Figure 65 shows the charge density for the SRR. The highest current density is measured on the Poly 2 structure at 1.2 x 10^{-6} pC/µm^2. Based on the charge density, the capacitance respective of each conductor is provided from the simulation. The capacitance for Poly 2, Poly 1 and Poly 0 are 0.102 pF, 0.14 pF and 0.0414 pF respectively.

www.manaraa.com

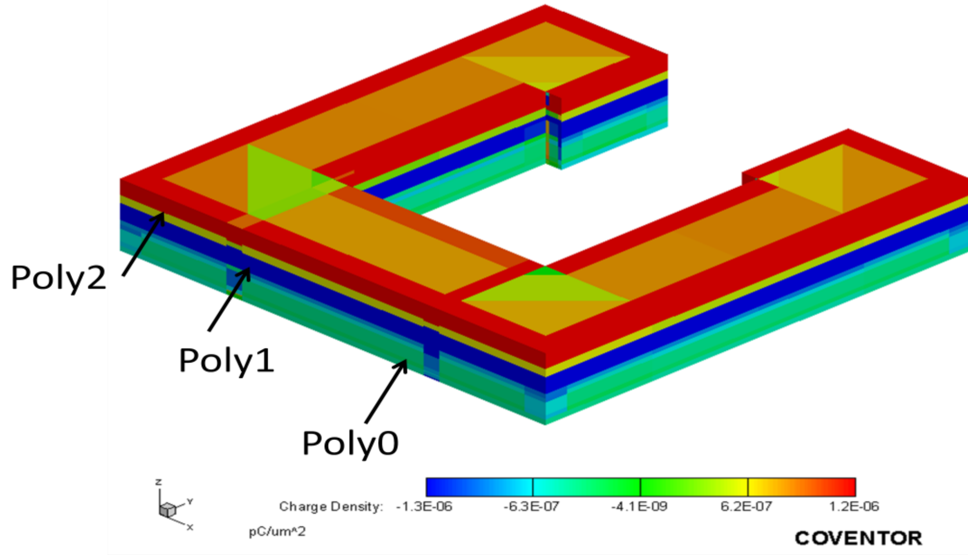

Figure 65. Charge density simulated on the THz SRR which is used to calculate the capacitance of the conductors with respect to the other conductors.

The MemHenry solver simulation tool for CoventorWare ® determines the electrical inductance and resistance for the conductors based on applying a simulated voltage on the conductors. The simulated voltage is an alternating current voltage with a frequency sweep from 0.01 to 100 THz. The simulated imaginary current density helps calculate the simulated inductance at each frequency. Figure 66 provides a detailed image of the response for each layer to the simulated alternating voltage and the magnitude of the imaginary current density. Using the simulated inductance at 1 THz, the resonant frequency for the SRR is calculated with inductance for three Polysilicon layers. The inductance for the Poly 2, Poly 1 and Poly 0 layers are 35.81 x 10^{-12}H (pH), 35.01 pH and 37.67 pH, respectively.

www.manaraa.com

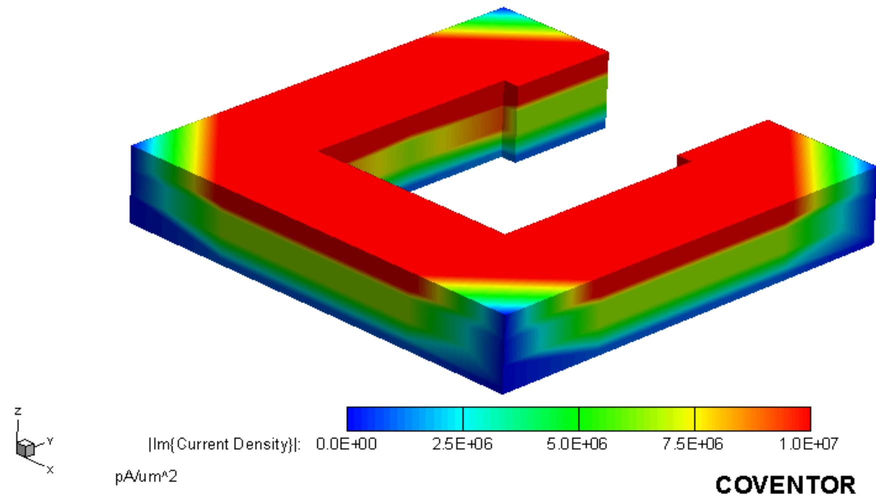

Figure 66. The imaginary current density magnitude simulated for the SRRs of the metamaterial structure.

Based on the simulation results and using the resonant frequency equation, the expected resonate frequency is 3.8 THz. The simulation values are lower than the analytical value of 5 THz which could attributable to the nitride layer under the meta-atoms. The experimental testing will help verify these results.

Appendix C.3. Testing for polyMUMPS ® Terahertz Metamaterial Structures

Experimental testing is conducted with Fourier transform spectroscopy (FTS) on three metamaterial samples and a sample with no SRR structures. The transmission response is captured by a Fourier transform spectrometer equipped with THz optics at a resolution of 4 cm^{-1}. The measurements are performed in a vacuum at room temperature. The transmission response is calculated from the ratio of the reference spectrum and the sample spectrum.

The three samples are measured all with identical structures but with varying degrees of surface quality. Sample 1 has the worst quality, while sample 3 has the best. Figure 67 shows the surface quality of the structures captured with using a scanning

المنارة للاستشارات
www.manaraa.com

electron microscope. The image shows a polysilion layer on top followed by the silicon dioxide layer. Figure 68 shows the structural layers for the polyMUMPS® process. A focused ion beam etched out the layers to help identify the layer thickness and insure the silicon dioxide layers separate the polysilicon layers. Each layer thickness is comparable to Figure 64, the schematic illustrating the expected layer thickness.

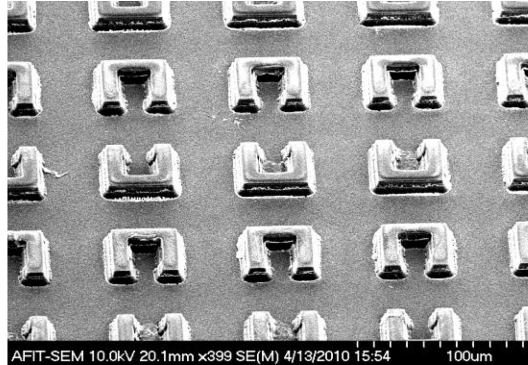

Figure 67. THz Metamaterial structures shown in an SEM image to show quality of SRRs and surrounding surface area. This image is a 0.06 mm^2 area taken out of a 1 cm^2 area.

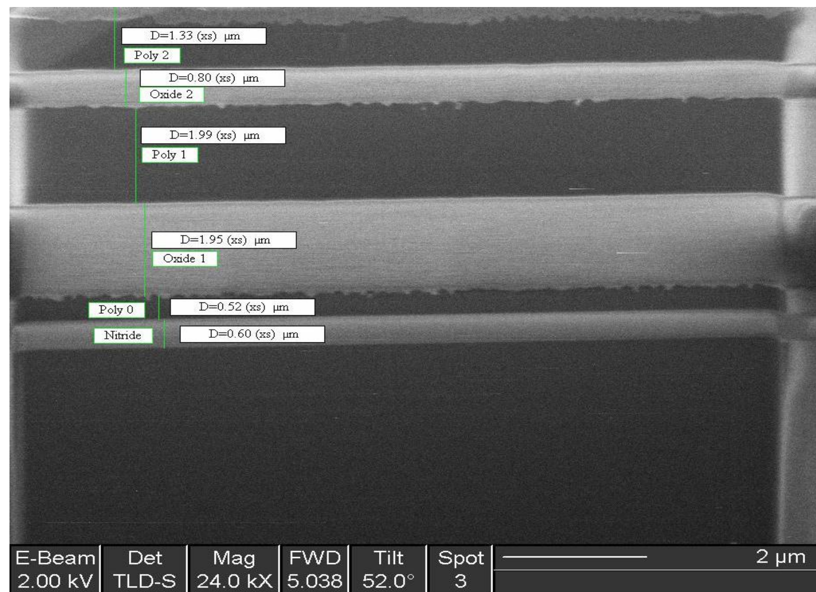

Figure 68. Layers of the polyMUMPS ® structures etched out using a focused ion beam to inspect the Polysilicon and silicon dioxide layers.

www.manaraa.com

The FTS transmission spectrum for the sample without SRRs, shown in Figure 69, has 0% transmission in the frequency range investigated. This is expected, considering silicon dioxide is not transparent in the far IR. The transmission spectra of all three structured samples shown in Figure 70, have an off resonance transmission of about 25 % which drops off at the resonant frequencies. The spectra for all three samples have a small resonance around 3.7 THz due to the LC response of the SRRs where the transmission drops to approximately 15%. Also present in all the spectra is a resonance at 18.4 THz where the transmission decreases to 5% to 10% depending on the sample surface quality. The resonance nulls deepen as the surface quality of the material improves.

The analytical calculation is performed with MatLab®, which determined the resonant frequency should be around 5 THz using the dielectric constant of 3.9 for silicon dioxide. The material stacks also contain a thin layer of silicon nitride which may affect the dielectric properties of the material. Calculating the resonance using a dielectric constant of 7.8 for silicon nitride yields a resonant frequency of 3.5 THz, which is much closer to that measured with the FTS [46].

The overall low transmission amplitude is most likely a result of the layered material. Layered materials are known to cause a decrease in the transmission and to broaden the resonance; however, the resonant frequency remains constant [82]. The low resonance response could be a result of the materials used to fabricate the structures. The samples are grown on single side polished crystalline silicon. The unpolished backside of the samples resulted in too much scatter for measurements to be obtained. The following transmission plots were only obtained after the backside of the samples was polished to a

www.manaraa.com

highly reflective surface. The off resonance transmission is around 30%. The resonance dip in the transmission spectrum is about 15% and 5% for the dipole resonance.

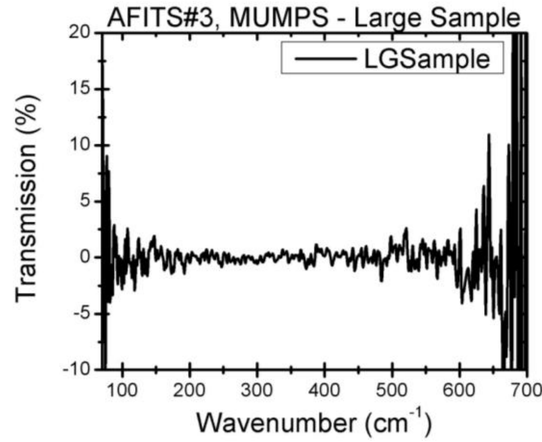

Figure 69. Transmission spectra of the polyMUMPS ® material without the SRRs showing zero transmission across the measured frequency range.

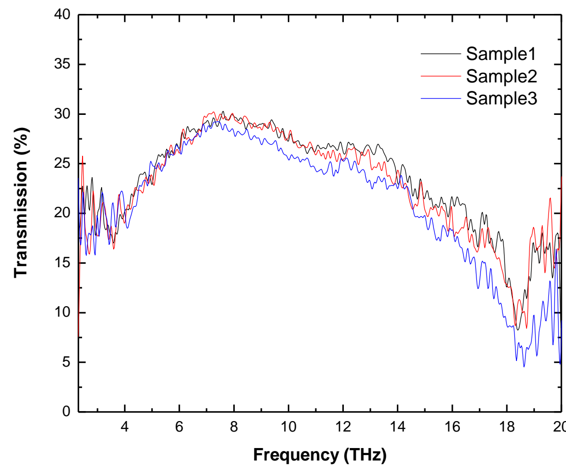

Figure 70. Transmission spectra of the polyMUMPS ® samples fabricated with SRRs showing a transmission of about 25% and a resonance at 3.7 and 18.4 THz

المنارة للاستشارات
www.manaraa.com

Appendix D. Investigation into Optical Metamaterials

Optical metamaterial structures concentrate on the visible and infrared spectrum for electromagnetic waves. The metamaterials at this level are not split ring resonators but take on forms of fishnet or nanorod designs. In the following subsections, the background, simulation and testing of optical metamaterials will be discussed.

Appendix D.1. Optical Metamaterial Structures Background

Optical metamaterials consists of layers of nonmagnetic metal and dielectric materials arranged in a periodic fashion to account for the electric and magnetic field interactions. Majority of optical metamaterials take on the form of fishnet structures which is different from split ring resonators at RF wavelengths. Figure 71 shows two fishnet structures forming an optical metamaterial design for a layout which separates the incident magnetic and electric fields [83].

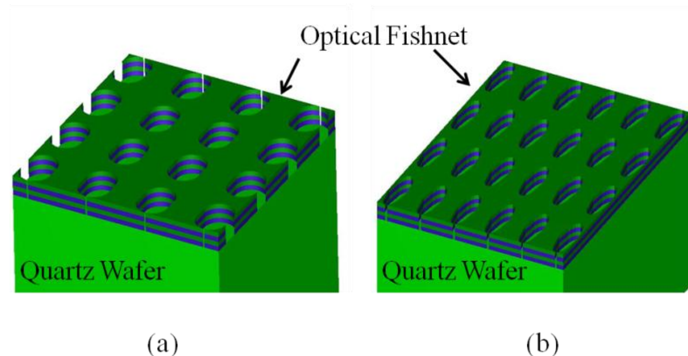

(a) (b)

Figure 71 Optical Metamaterial Designs

To date, researchers have achieved negative index on metamaterials at low wavelengths, publishing results at 1.8, 1.5, 1.4, 0.813, and 0.772 μm [84]. For example, an incident magnetic field would be polarized along the set of wide parallel strips while the incident electric field is aligned along the narrow parallel strips. The magnetic strips of the different layers are coupled at the magnetic resonance. For an optimized design,

www.manaraa.com

the magnetic resonance should be sufficiently strong resulting in negative values for the effective permeability. The electric field should not show signs of diffraction since the structure is sub-wavelength compared to the electric field. Another consideration for the metallic strips is the metal type used in the design. Consideration must be made for the plasma frequency of the metal. Plasma frequency is the natural frequency of oscillation in the metal at which free electrons and positive ions may be thought of as plasma. The plasma frequency serves as a critical value below which the index is complex and the penetrating waves drop off exponentially from the boundary [85]. The structural units of the optical fishnet must be smaller than the wavelength of the incident radiation. Looking at the metal's plasma frequency helps determine the metallic thin film to use in optical fishnets. For example, the structural units can range in sizes from λ, λ/5. λ/10, to λ/10000. Using the frequency of radiation for silver and photon absorption

$$\lambda = \frac{1.24}{E(eV)}(\mu\text{m}) \tag{50}$$

where E represents the photon energy, the photon absorption equation helps to determine metals to use in the optical fishnet structure. For example, silver has a frequency of radiation equal to 0.903 x 10^{15} Hz. Based on the photon absorption equation, the smallest wavelength at which silver will not absorb photons (0.332 μm). Taking into account the frequency of radiation and the structural unit size, the layout of the optical fishnet will have dimensions smaller than the incident light used for experimental testing. The frequency of radiation for metal helps to eliminate metals which are part of the overall structure and cannot respond at optical frequencies.

المنارة للاستشارات
www.manaraa.com

The thin dielectric film isolates the metallic layers and forms a capacitive gap that factors into the overall resonance. The dielectric film can be tailored based on the material used for this layer. A common dielectric material is aluminum oxide, commonly known as alumina, which has a dielectric constant of ~9.0 at DC [86].

A major consideration of optical metamaterial is to have a sub-wavelength response from the structure. The combination of the metallic strips and dielectric layers attribute to the response of the structure. Finding the correct material composition has to be based on the materials and specific frequency.

The optical structures were fabricated in-house at the Sensors Directorate, Air Force Research Laboratory, Wright-Patterson AFB Ohio. The initial designs were based on the double negative index metamaterial demonstrated by Chettiar *et al*. [83]. Having a fundamental design to initiate development of the metamaterial structure reduced research and developmental time and gave a milestone for the in-house efforts. The structures consist of layers of Alumina (Al_2O_3) and Silver (Ag). One layer of Gallium doped Zinc Oxide (Ga-ZnO) separates the metamaterial from the quartz wafer. The metamaterial structure is deposited on quartz wafers to reduce interference for optical transmission. Figure 71 (A) shows the L-Edit 3-dimensional layout of the metamaterial based on [83]. The stadium design is processed with e-beam lithography. The dimensions of the stadium are 100 nm x 150 nm. The periodicity of the structure is 300 nm. Figure 71 (B) is the modification made to initial designs based on research and investigations conducted by others developing metamaterial structures [83]. The initial Al_2O_3 and Ga-ZnO layers help with adhesion to the wafer. The final layer is a thin layer of Al_2O_3 to keep the silver layer from deteriorating. The Ga-ZnO layer is deposited by pulsed laser

المنارة للاستشارات
www.manaraa.com

deposition (PLD). With a PLD system, a laser ablates a target to create a plasma plume of the material. In this case, the laser ablates the gallium and zinc in an atmosphere of oxygen. The alumina and silver are sputtered on top of the Ga-ZnO by a Denton Discovery 22 Sputtering system. The system has the capability to deposit material using DC or RF electrodes. In the project, we used the RF electrodes to sputter material. Fused silica was used for initial wafers to complete etch studies for the metamaterial pattern. Quartz wafers were used for the final etch studies. The quartz wafers offer better reliability for the process used to deposit Ga-ZnO. Quartz wafers withstand the temperature change during the PLD process. Fused silica wafers have a tendency to crack or fracture because of the temperature shock during deposition.

To define the metamaterial structure, an etching process was developed to clear the alumina and silver in stadium and elliptical areas. The 3-D layout in Figure 71 for the optical metamaterial show graphically how the openings should look after the etching process. In order to etch the materials, a two-step process was developed to remove the alumina and then the silver. A Inductively Coupled Plasma (ICP) etcher was used to perform the dry etching. The main reason for using the ICP etcher is to have the ability to etch the profile and a have a low degree of undercutting in the structure. ICP etching also gives the ability to control the etching process with time, flow rates, and applied RF power. The first step involves clearing the top layer of alumina with boron trichloride ion coupled plasma etch. The second step consists of an argon gas ICP etch to clear away oxide and silver. The two steps are repeated to clear multiple layers of alumina and silver. Figure 72 shows the results of the etch process conducted on large open areas. Figure 72

المنارة للاستشارات
www.manaraa.com

(B) shows how aggressive the etch process is to the structure. In order to reduce the damage done to the sidewall profiles, reduced RF power during etching is recommended.

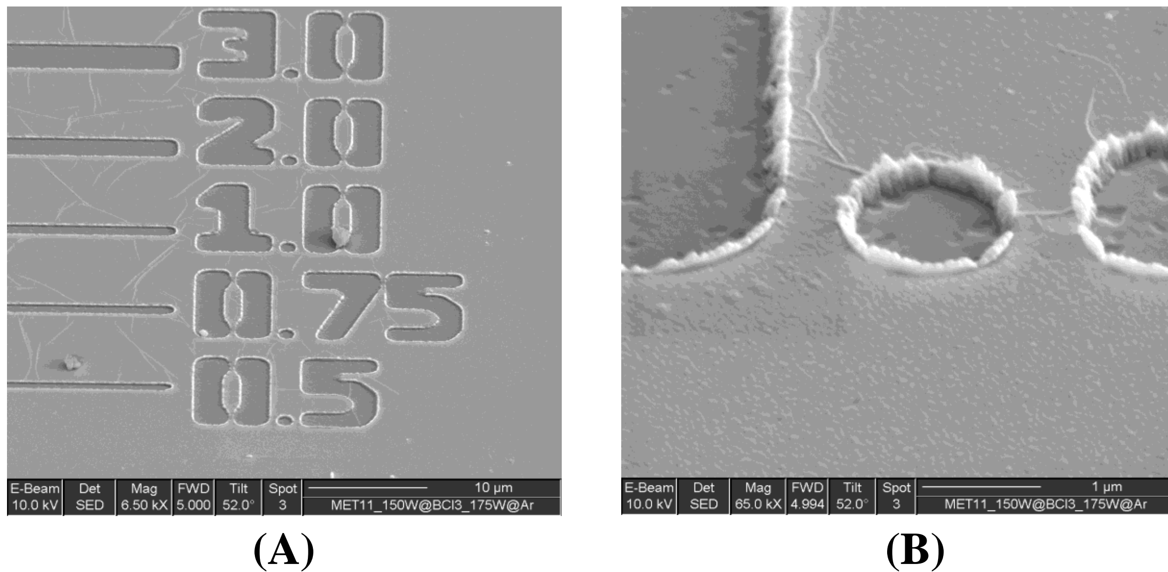

Figure 72 Metamaterial etching results

Figure 73 shows the initial results obtains of the optical fishnet. The SEM images show a optical fishnet covering a 100 μm^2 area. Figure 73 (B) shows a zoomed in view of the lower right hand corner area. The resist used in the processing of the wafer was not removed before capturing the images. The dislocations in the resist are due to rinsing off the wafers with deionized water immediately after etching. Deionized water removes any loose resist and helps to clear the etch areas after the etching process. By comparing the fabricated structure to Figure 71 (A), the E-beam system creates a good profile with high resolution for the stadium optical fishnet structure. The dimensions of the stadium are 100 nm x 150 nm (±20 nm). The periodicity of the structure is 300 nm (±20 nm). To make further improvement to the structure, we are investigating the ICP etching process by using a lower RF bias and shorter etching times for the two etch steps.

www.manaraa.com

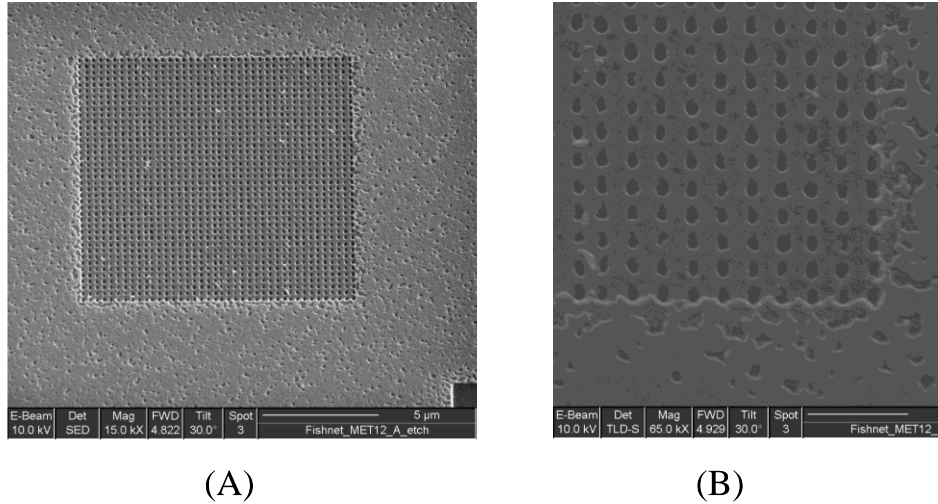

(A) (B)

Figure 73 SEM image of optical fishnet structure

The design and fabrication of the optical fishnet structure is an intricate process. The level of effort needed to make a contribution at optical wavelength has proved to require a great deal of time which goes beyond this initial research.

Appendix D.2. Simulation for Optical Metamaterial

The optical metamateial is based on initial research by [83] which performed simulation and analysis using COMSOL Multiphysics. The simulation consisted of using a unit cell of the stadium with a void similar to Figure 71 (A). The layers consisted of silver and alumina with the permittivity of silver taken from experimental data with the exception that the imaginary permittivity is assumed to be three times that of bulk silver [10]. The experimental and simulated spectra matched well over a broad range of measured wavelengths and included sharp resonant features [83].

Appendix D.3. Testing for Optical Metamaterial

The optical metamaterial structure was fabricated using E-beam lithography and two methods for interferometric lithography. The reason for using the three methods was

المنارة للاستشارات
www.manaraa.com

to determine which fabrication process provides a stable method to generate the sub-micron features over a broad area. Collaborations with the Air Force Research Laboratory, and University of Dayton were started to help with the fabrication processes. The E-beam lithography is a process that has advantages and disadvantages for generating optical metamaterial. An advantage for the E-beam lithography includes the ability to pattern small features as small as 100 nm. Another advantage is the defined lithography process for pattern generation. However, a major disadvantage is the long write time and small pattern area which takes hours to write a 1 cm^2 area. Figure 74 shows a 10 × 10 μm area exposed and developed out for the optical metamaterial fishnet patterning. The openings are on the order of 200 nm and the photoresist lines are 150 nm in width.

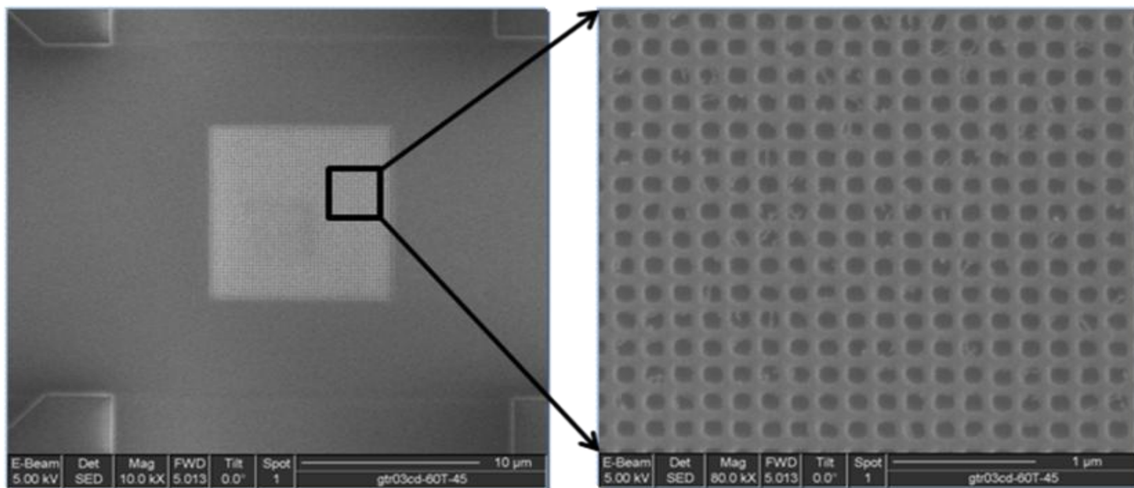

Figure 74. Optical metamaterial fishnet pattern generated by E-beam lithograpy

The interferometric lithography is a new pattern generation process [92], [93]. The reason for using this process is for the short time it takes to generate features in photoresist across a large area. A disadvantage is the wavelength dependent structural size for the fishnet pattern. Two interferometric lithography processes were used to

المنارة للاستشارات
www.manaraa.com

process samples at DUV (266 nm) and Visible (488 nm) wavelengths. The lithography system for the DUV wavelength was set up at the University of Dayton. It was able to produce features on the order of 100 nm with a periodicity of 150 nm over a $1mm^2$ area. Due to the small area, test was not performed on the samples. However, the sample patterns were inspected using a SEM. Figure 75 is a SEM image of the photoresist patterned using the interferometric lithography which generated the fishnet pattern.

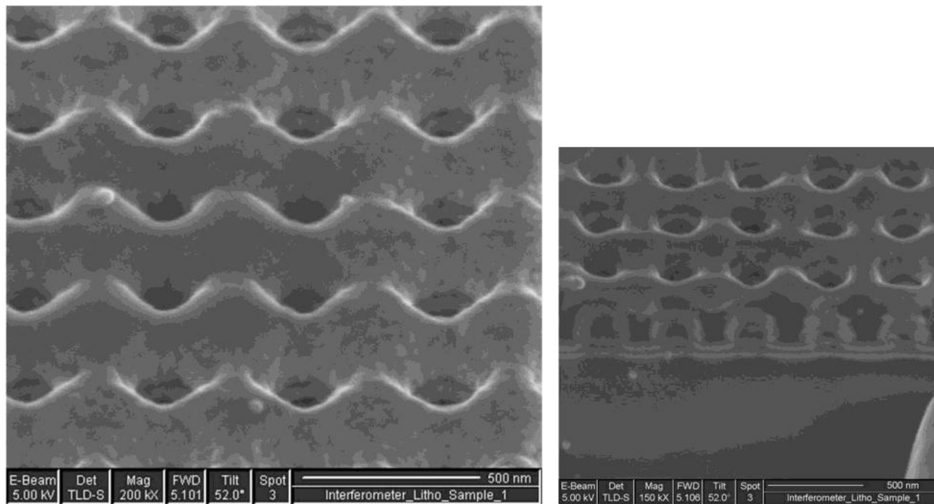

Figure 75. Interferometric Lithography sample completed at the University of Dayton.

At the Air Force Research Laboratory, an interferometric lithography system is set up to use a 488 nm wavelength diode laser. It has the capability to generate 1 cm^2 fishnet patterns using SU8-2025 blended with cyclopentanone and Cyclopentadienyl (fluorine) iron (II) hexafluorophosphate which absorbs at the 488 nm wavelength. It provided the best samples of the optical fishnet with features over a 0.5 cm × 0.5 cm area. Figure 76 shows two SEM images of the fishnet pattern. The first image shows the fishnet pattern with thin lines in one direction and thick line normal to the thin line which is necessary to define the electric and magnetic directions for the strips. The second

المنارة للاستشارات
www.manaraa.com

image shows a top down view of the pattern to see how well the stadium was patterned with the unexposed photoresist removed.

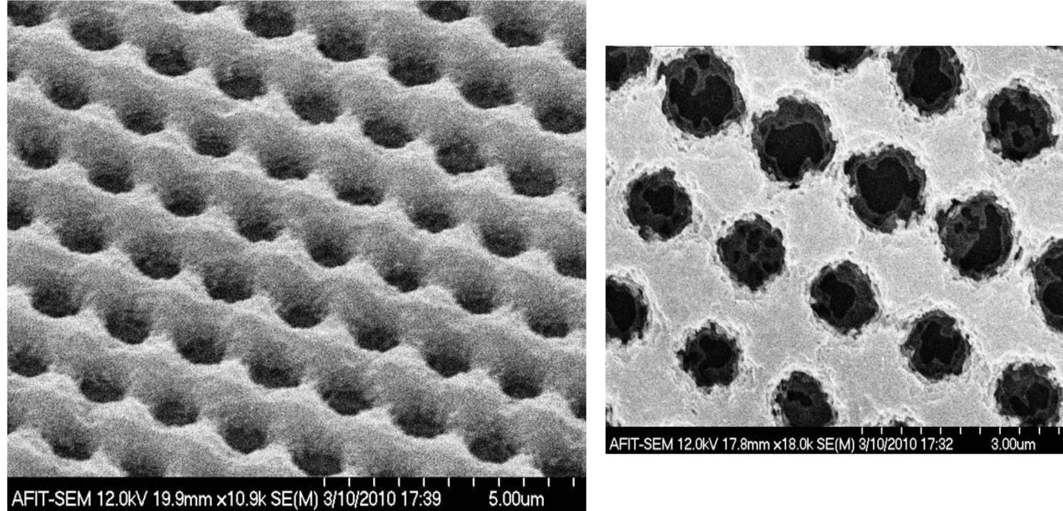

Figure 76. Interferometric Samples generated at Air Force Research Laboratory.

Testing was performed on samples from the Air Force Research Laboratory using AFIT's Complete Angle Scatter Instrument (CASI) to obtain the bi-directional reflectance distribution function of the optical metamaterial [94]. A calibrated laser illuminates the sample at different incident angles, and the resultant reflections from the sample (and/or the transmission through the sample) are measured and recorded by a sensor mounted on a movable arm. Figure 77 shows the CASI and the orientation directions from the sample. Both in-plane and out-of-plane measurements can be performed based on the geometry of the sample's orientation. Optical metamaterial testing was accomplished to collect data on the reflection generated by the fishnet which provides understanding for the fishnet structure's reflection and transmission properties. Figure 78 shows the reflection amplitude for the optical metamaterial at a range of different angles. The reflection peaks occur near -95, -40, -20 and 2 degrees. Due to the

المنارة للاستشارات
www.manaraa.com

number of reflection peaks, the structure shows indications of a diffraction grating at optical frequencies.

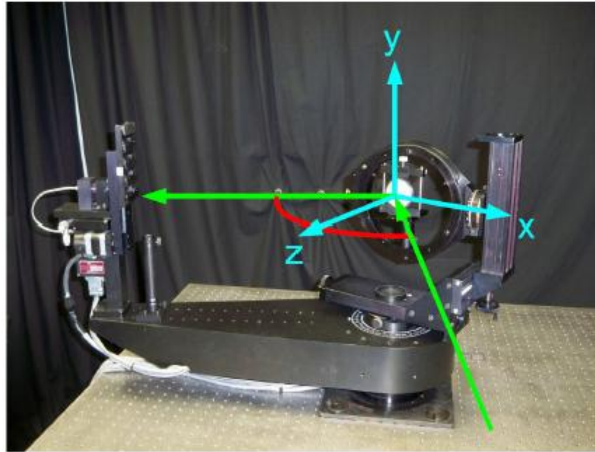

Figure 77. AFIT's complete angle scatter instrument used to measure bi-directional reflection distribution function for optical metamaterials.

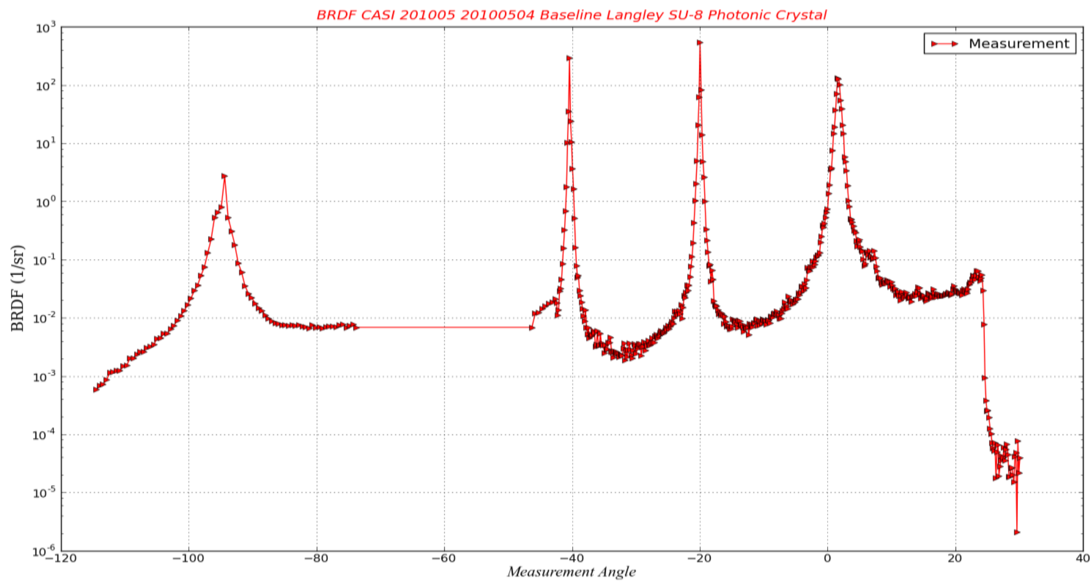

Figure 78. Bi-directional reflectance distribution function measurements for the optical metamaterial fishnet. Results show the structure is a diffraction grating at optical frequencies.

المنارة للاستشارات
www.manaraa.com

Appendix E. IR Meta-atom Incorporated with a Thin-Film Transistor

Focusing on the infrared (IR) region, the construction of metamaterial has a lot of potential. The IR region is commonly used in remote control of TVs, VCRs and CD players. IR technology is also being used and developed for medical monitoring systems as well as remote control of environmental control systems, personal computers, and talking signs [87]. Within wireless communication, IR has several advantages and disadvantages which are listed in Table 5.

Table 5. Advantages and disadvantages of IR wireless communication.

Advantages	Disadvantages
Low power requirements: therefore ideal for laptops, telephones, personal digital assistants	Line of sight: transmitters and receivers must be almost directly aligned (i.e. able to see each other) to communicate
Low circuitry costs: $2-$5 for the entire coding/decoding circuitry	Blocked by common materials: people, walls, plants, etc. can block transmission
Simple circuitry: no special or proprietary hardware is required, can be incorporated into the integrated circuit of a product	Short range: performance drops off with longer distances
Higher security: directionality of the beam helps ensure that data isn't leaked or spilled to nearby devices as it's transmitted	Light, weather sensitive: direct sunlight, rain, fog, dust, pollution can affect transmission
Portable	Speed: data rate transmission is lower than typical wired transmission
Few international regulatory constraints: IrDA (Infrared Data Association) functional devices will ideally be usable by international travelers, no matter where they may be	
High noise immunity: not as likely to have interference from signals from other devices	

Appendix E.1 IR Metamaterial Structure Background

Two areas of interest for military application are telecommunication structures and night vision. For telecommunications, the C-Band is the dominant band for long-distance networks. The C-Band covers the 1530 to 1565 nm wavelength of the spectrum. Telecommunication typically involves the use of electronic devices such as telephones,

المنارة للاستشارات
www.manaraa.com

television, radio or computers. Telecommunication is an important part of the world economy and the telecommunication industry's revenue was estimated to be $1.2 trillion in 2009 [88]. Night vision equipment is used when there is insufficient visible light to see. Night vision devices operate through a process involving the conversion of ambient light photons into electrons which are then amplified by a chemical and electrical process and then converted back into visible light via data processing. IR sources can be used to augment the available ambient light for conversion by night vision devices, increasing in-the-dark visibility without actually using a visible light source [89].

Focusing on the telecommunication industry, transmitters and receivers are used to transfer data over land, within buildings and over fiber optic links. The ability to generate these signals with small amounts of attenuation and dispersion have made IR a vital part of the telecommunications industry. Two benefits of introducing metamaterials into IR telecommunication systems would be for the improvement of the transmission signals or filtering out unwanted signals within the communication link.

Metamaterials composed of SRR meta-atoms can help with IR data transmission improvements for the telecommunication industry. The structures can enhance imaging systems by improving the refractive index. For example, a filter or flat lens created with SRR can control the propagation of the IR signals to enhance the directivity or divert the signal away from a detector. Figure 79 shows a diagram which gives an indication on how the flat lens can be used to control the propagation of the light. As the IR approaches the flat lens, the direction of propagation can be controlled by the refractive index of the metamaterial and the angle of incidence.

المنارة للاستشارات
www.manaraa.com

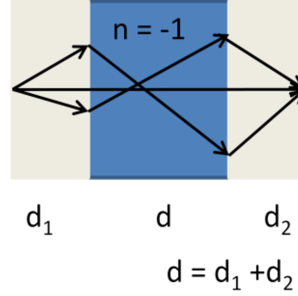

Figure 79. Cartoon showing the effect of negative refractive index.

Appendix E.2. Analytical Approach to IR Meta-atom

To explain how this is possible, an analytical approach is used analyze the behavior of the SRR meta-atom. Soukoulis, et al, conducted analytical studies of the SRR structure and compared the results to experimental data [90]. From his modeling studies, the SRR meta-atom can be set to a particular resonant frequency of interest which allows the control for the refractive index of the structure. Knowing the IR spectrum range (700 nm to 1 mm) is a key element in the design of SRR operating at this range. The SRR can be as large as 1/5 the wavelength size down to 1/10000 but depends on material parameters and fabrication capabilities. Basing the design on the requirement for the refractive index and wavelength of interest, the modeling procedures demonstrated by Soukoulis, *et al*. help to determine the structure of the SRR meta-atom [90].

Beginning with the index of refraction, the permeability (μ) and permittivity (ε) components which make up the index of refraction can be broken up into the polar (real and imaginary) forms to effectively change the overall index of refraction.

$$n = \sqrt{\varepsilon}\sqrt{\mu} = \sqrt{|\varepsilon||\mu|}e^{i\frac{1}{2}(\theta_\varepsilon + \theta_\mu)} \tag{51}$$

Based on the Equation (51), if you account for the real and imaginary parts of ε and μ, while including the expansion of these components for lossy media, the index of

المنارة للاستشارات
www.manaraa.com

refraction can be adjusted for a specific frequency. To achieve a negative index of refractive, the argument of the index of refraction which is given by $\theta_\varepsilon + \theta_\mu / 2 \in [0, \pi]$ has to reach a range of $[\pi/2, \pi]$ in the situation when $\varepsilon' < 0$ and $\mu' < 0$, so that the real part of the index of refraction is negative ($n' < 0$). In particular, the lossless limit is obtained as $\theta_\varepsilon \rightarrow \pi$ and $\theta_\mu \rightarrow \pi$ which produces: $n = \sqrt{|\varepsilon||\mu|}e^{i\pi} = -\sqrt{|\varepsilon||\mu|}$ [2]. Using the assumption of an isotropic medium, this index of refraction can be directly introduced into Snell's law and can be shown to change or reverse the refraction direction [2].

Further reducing ε and μ for defining the index of refraction will help analyze the response for the SRR structure. Knowing that capacitance is based on permittivity and the dimensions of the structure, the overall capacitance of the SRR is calculated by the following equation.

$$C = \varepsilon_0 \varepsilon_r \frac{wt}{g} \tag{52}$$

The components of the capacitance are: ε_0, is the permittivity of free space, ε_r, is the relative dielectric constant, w is the width, t is thickness and g is the gap of the capacitor spacing for the dielectric layer.

The inductance of the SRR is based on the geometric structure. For simplicity, an assumption must be made on the shape of the structure which is defined as a solenoid. By having a solenoid structure, the inductance of the design can be calculated and used to obtain the resonant frequency of the SRR. The equation for calculating the inductance of a solenoid is given by Equation (53), which can also be used to determine the resonant frequency of the SRR design.

المنارة للاستشارات
www.manaraa.com

$$L = \mu_0 \frac{l^2}{t} \tag{53}$$

where l is the length and t represents the thickness of the material.

Using the C and L values, the resonant frequency (ω_{LC}) is calculated by using Equation (54). Knowing the ω_{LC} allows the calculation for the corresponding free-space wavelength (λ_{LC}) which is given by Equation (55).

$$\omega_{LC} = \frac{1}{\sqrt{LC}} \tag{54}$$

$$\lambda_{LC} = \frac{2\pi c}{\omega_{LC}} \tag{55}$$

Having the λ_{LC} value helps to determine if the size SRR is reasonable enough to be considered as a metamaterial structure. Because the operational wavelength in metamaterial is much larger than the size of the unit cell, a, the metamaterial can be considered a homogenous effective medium and described using effective medium theories, which greatly simplify the description and facilitate the physical understanding of its main features.

Knowing that the SSR can be classified as an effective medium allows the use of analytical modeling for effective medium. The effective magnetic permeability expressed as a function of frequency, $\mu_{eff}(\omega)$, for a lattice of SRRs can be written as Equation (56) [90]. Assuming an incident electro-magnetic field propagates parallel to the plane of the SRRs with the magnetic field (H) perpendicular to the SRR plane and an electric field (E) parallel to the sides of the SRRs

www.manaraa.com

$$\mu(\omega) = 1 + \frac{F\omega^2}{\omega_{LC}^2 - \omega^2} \tag{56}$$

where F is the dimensionless quantity based on the lumped parameters.

$$F = \frac{l^2 t}{a_{xy}^2 a_z} \tag{57}$$

For the dimensionless quantity, a_{xy} is the lattice constant in the SRR plane, a_z is the lattice constant in the direction normal to SRRs [90].

Examining the effective permittivity as a function of frequency allows us to investigate the behavior of the permittivity based on plasma frequency of the metallic layer. Using a Drude-Lorentz form to describe the behavior of the permittivity requires three parameters: the plasma frequency, ω_p, the resonant frequency, ω_0, and the dissipation parameter, Γ (the damping factor). Equation (58) calculates the response of the effective permittivity as a function of frequency.

$$\varepsilon(\omega) = 1 - \frac{\omega_p^2}{\omega^2 - \omega_0^2 + i\Gamma\omega} \tag{58}$$

Combining the permittivity and permeability together into Equation (51) for the refractive index predicts the analytical behavior of the SSR. For the IR metamaterial, the analytical modeling can be used to determine structural dimensions, resonant frequency and index of refraction.

Appendix E.3. IR Application

Using the information acquired about the use of IR in communication and imaging systems, an array of SRRs can be made to alter the propagation of IR signals through a flat lens or film. As an example, the U.S. Naval Surface Warfare Center-Crane

المنارة للاستشارات
www.manaraa.com

in Crane, Ind., ordered Enhanced Targeting Sight (ETS) Infrared Imaging Systems from FLIR Systems in North Billerica, Mass. This order is the first production order under an indefinite delivery/indefinite quantity contract from the U.S. Navy valued at approximately $35 million. The systems are based on the company's rugged SeeSpot III high performance thermal imager that allows operators to identify targets and view laser designators simultaneously. Used in both day and night battlefield environments and in degraded weather conditions, the ETS increases the accuracy of laser designators by allowing operators to view the laser spot within the target scene. It uses a detector at 4.50-4.80 μm and 1.06 μm to create thermal images as shown in Figure 81 [95].

Figure 80. SeeSPOT III+ Imager uses IR to detect object at night [95].

Identifying Target

Laser Designator

Figure 81. IR Images obtained with the SeeSPOT III+ Imager.

المنارة للاستشارات
www.manaraa.com

Creating a flat lens out of metamaterial can help to improve the image quality by filtering out unwanted thermal signatures and enhancing/changing the propagation of IR signals at the wavelength detected by the detector. The metamaterial can also be used to stop or reduce detection of the signal if a transition material was installed that effects the SRR based on an applied bias. These two concepts are be analyzed in the following section.

Appendix E.4. IR Meta-atom Structure at 60 THz

Designing a metamaterial at the 4.50 – 4.80 μm range requires that the feature size be a maximum of 0.90 – 0.96 μm. To build features for these dimensions, calls for thin films and dielectric materials that can be used in fabrication methods commonly used to generate microelectronic circuits. Converting the wavelength to frequency allows the analytical equations to determine the size of the SRR. The frequency range is 62.5 – 66.7 THz. Using the medium frequency, the design will have a resonant effect slightly below 64.6 THz. Based on Equation (55), λ_{LC} will equal 29.2 μm which is higher than the SRR structural size.

The next step will be to determine the dimension necessary for the SRR meta-atom. Knowing that the maximum size can be no larger than 0.90 μm helps to set the maximum length for the SRR meta-atom. Setting the length to 0.9 μm helps to eliminate one of the structural parameters.

The next steps will be to define the dielectric constant, width and gap for the SRR meta-atom. The first process will be to examine the effect of changing the dielectric constant on the structure. By setting the width, thickness, and gap of the SRR to all equal

المنارة للاستشارات
www.manaraa.com

0.3 μm, the range of dielectric constant can be investigated to show which values of the dielectric constant can keep the free-space wavelength (λ_{LC}) higher than 29.2 μm. Figure 82 shows four plots to compare the free space wavelength against parameters. First, Plot (a) shows the range of dielectric constants needed to keep the value high. Using the dielectric constant of silicon dioxide, the SRR's λ_{LC} is examined as a function of width. Plot (b) shows the range of the λ_{LC} as the width is varied from 0.001 to 0.75 μm. Plot (c) is the range of the λ_{LC} at various gaps, while Plot (d) compares the change to various lengths.

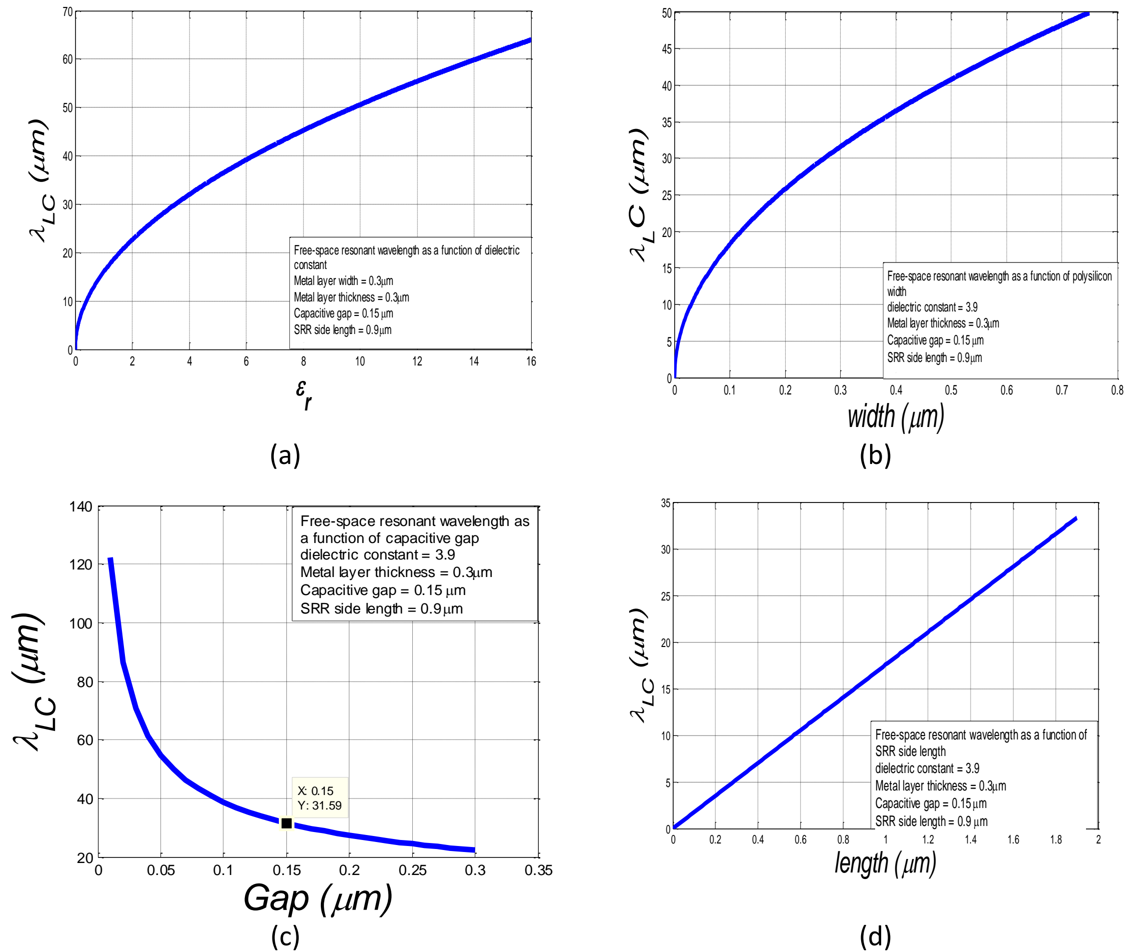

Figure 82. Free-space wavelength as a function of permittivity, width, gap and length.

المنارة للاستشارات
www.manaraa.com

The effective magnetic permeability expressed as a function of frequency, $\mu_{eff}(\omega)$, for a lattice of SRR meta-atoms are predicted using Equation (56). Assuming an incident electro-magnetic field propagates parallel to the plane of the SRR meta-atoms with the magnetic field (*H*) perpendicular to the SRR plane and an electric field (*E*) parallel to the sides of the SRRs. Figure 83 shows the effective magnetic permeability versus frequency.

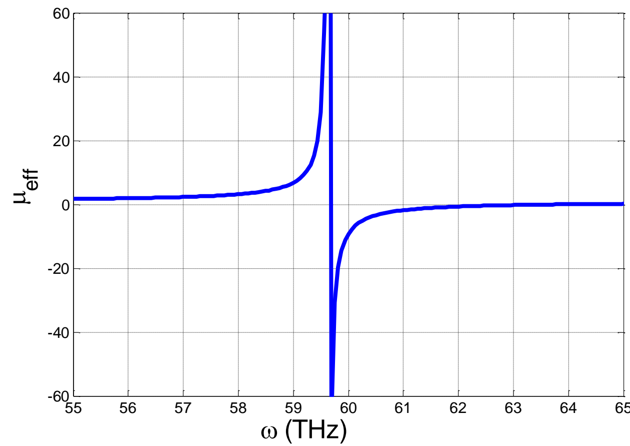

Figure 83. Effective permeability as a function of frequency.

Combining the effective permittivity and effective magnetic permeability into Equation (51) for the index for refraction produces the results shown in the follow figures. Notice the dramatic change in both the real and imaginary index of refraction based on the analytical calculations. From initial observations, the choice of gold for the metal layer has a big effect on the refractive index.

المنارة للاستشارات

www.manaraa.com

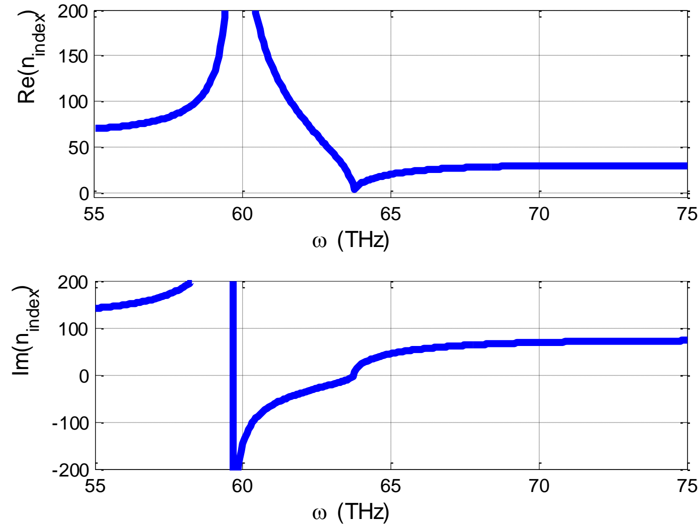

Figure 84. Index of refraction calculated using the effective permittivity and permeability.

To change the structure based on biasing a transition material is one method that would affect the overall response for the SRR meta-atom. By incorporating a thin film transistor into the structural pattern of the SRR meta-atom, the biasing that generates an electric field can alter the refractive index response. Thin film transistor (TFT) structure is similar to MOSFET built on silicon-on-insulator with the exception that the active film is a deposited thin film and the substrate can be any form [91]. In the case of the metamaterial structure, a transparent semiconducting material would be the ideal material because it will allow IR and visible light to penetrate the structure unaffected. The TFT could be biased to turn off and on by a gate separated from the channel by a thin oxide layer. A material that can make up the transistor region would be doped Zinc Oxide which is transparent and possesses semiconductor characteristics. The gate region can be made from Indium Tin Oxide, a transparent electrode. The drain and source regions would be the SRR structure. Figure 85 shows a diagram of the structure with the SRR as

المنارة للاستشارات
www.manaraa.com

the source and drain connected to the transparent transistor. The structure is created on a quartz wafer to help with isolation for the device and allow IR signals to propagate through the substrate.

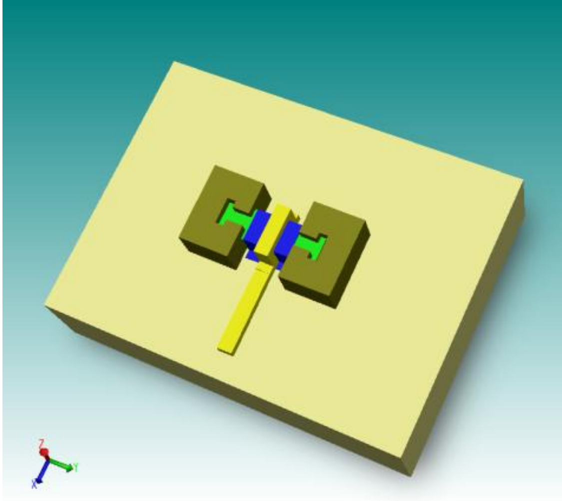

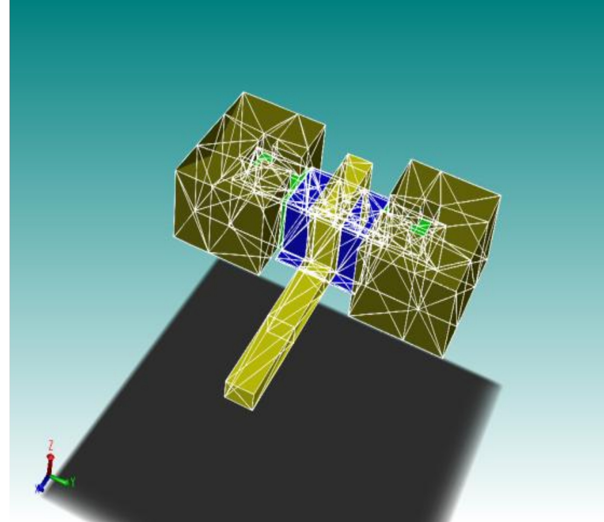

Meta-atom with transistor   Mesh model of meta-atom

Figure 85. Thin film transistor integrated into SRR meta-atom.

Fabrication of the device consists of 9 Steps. The following flow chart describes the process in a step-by-step sequence.

المنارة للاستشارات
www.manaraa.com

Process Flow

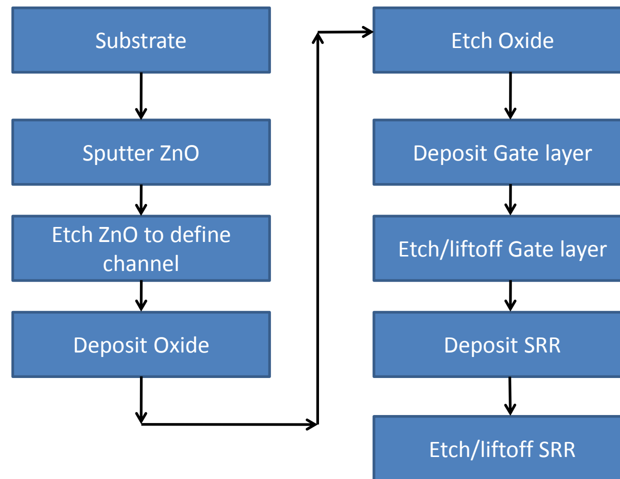

Using CoventorWare ®, simulations were conducted to investigate the capacitance and charge effects on the structure. The simulation compares the structure with the ZnO acting as a conductor and a dielectric. The following images give a view of the charge density of the structure with the ZnO acting as a conductor.

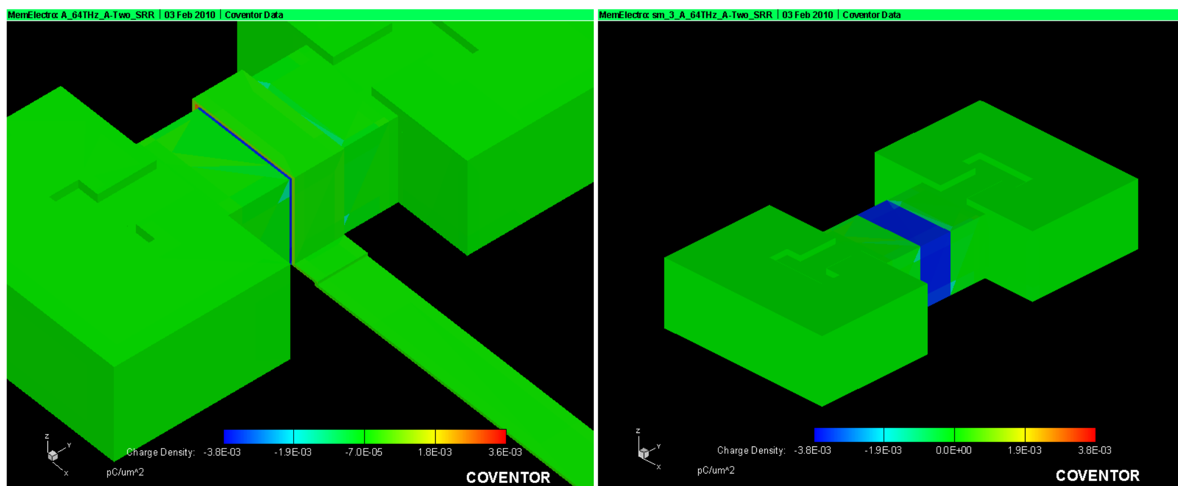

Figure 86. Images showing charge density of the gate when the doped ZnO act as a metal.

المنارة للاستشارات
www.manaraa.com

The simulated capacitance between the gate electrode and the doped-ZnO was determined by the simulation to be 6.8E-04 pF which is based on the thickness of the gate oxide and voltage of one volt applied between the two SRR structures.

The simulation was conduct by using the ZnO layers as a dielectric layer. The following plot shows the charge build up around the SRR region as a function of having opposite bias on the SRRs and a negative bias on the gate electrode. The charge is shown to build up around the gap of the SRR. The frequency of the signal was set to 64 THz which is close to the resonant frequency of the SRR.

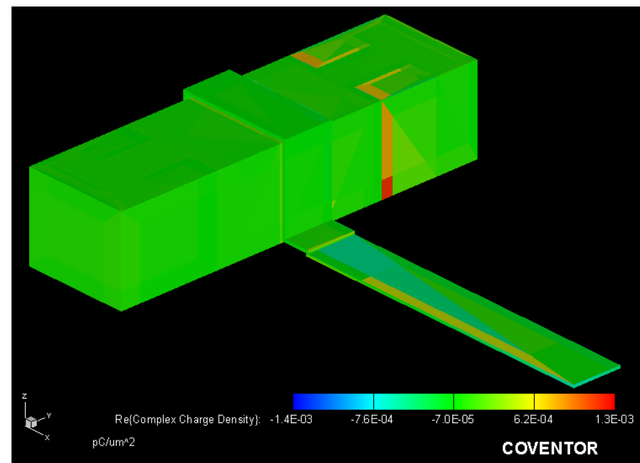

Figure 87. Charge density simulated on thin film transistor.
The SRRs are removed to show the charge density region.

www.manaraa.com

Bibliography

[1] Veselago, V.G. “The Electrodynamics of Substances with Simultaneously Negative Values of ε and μ,” *Uspekhi Fizicheskikh Nauk*, 10(4): 509-514 (January 1968).

[2] Ramakishna, S. A. and T. M. Grzegorczyk. *Physics and Application of Negative Refractive Index Materials*. Bellingham: CRC Press, 2009.

[3] Pendry, J. B., A. J. Holden, D. J. Robbins and Stewart, W. J. “Magnetism from Conductors and Enhanced Nonlinear Phenomena,” *IEEE Transactions on Microwave Theory & Techniques*, 47(11): 2075-2084 (November 1999).

[4] Driscoll, T., S. Palit, M. M. Qazilbash, M. Brehm, F. Keilmann, B-G. Chae, S-J. Yun, H-T. Kim, S. Y. Cho, N. M. Jokerst, D. R. Smith and D. N. Basov. “Dynamic Tuning of an Infrared Hybrid-metamaterial Resonance Using Vanadium Dioxide,” *Applied Physics Letters* 93(024101): 1-3 (July 2008).

[5] Zarifkar, A. and A. Rahmani. “Optical Bandpass Filter Design Using Split Ring Resonators, ” *Progress in Electromagnetics Research M*, 2: 93-103 (2008). http://www.jpier.org/PIERM/pierm02/06.08032801.pdf

[6] Strikwerda, A. C., K. Fan, H. Tao, D. V. Pilon, X. Zhang and R. D. Averitt. “Comparison of Birefringent Electric Split-Ring Resonator and Meanderline Structures as Quarter-wave Plates at Terahertz Frequencies,” *Optics Express*, 17(1): 136-149 (January 2009).

[7] Chettiar, U. K., S. Xiao, A. V. Kildishev, W. Cai, H-K. Yuan, V. P. Drachev, and V. M. Shalaev. “Optical Metamagnetism and Negative Index Metamaterials,” MRS Bulletin, *33*(10): 921-926 (October 2008).

[8] Veselago, V. G. “Remarks on Electrodynamics of Materials with Negative Refraction: Nonmagnetic Approach and Superlens as a Matching Device,” *Proceedings of the SPIE*, 5955: 1-8, (August 2005).

[9] Pendry, J.B. “Negative Refraction Makes a Perfect Lens,” *Physical Review Letters*, 85(18): 3966-3969 (October 2000).

[10] Schuring, D., J. J.Mock, B. J. Justice, S. A. Cummer, J. B. Pendry, A. F. Starr and D. R. Smith. “Metamaterial Electromagnetic Cloak at Microwave Frequencies,” *Science*, 314(5801): 977-980 (October 2006).

[11] Smith, D. R., W. J. Padilla, D. C. Vier, S. C. Nemat-Nasser and S. Schultz. “Composite Medium with Simultaneously Negative Permeability and Permittivity,” *Physical Review Letters*, 84(11): 4184-4187 (May 2000).

المنارة للاستشارات
www.manaraa.com

[12] Shelby, R. A. D. R. Smith, S. C. Nemat-Nasser, and S. Schultz. "Microwave Transmission Through a Two-dimensional, Isotropic, Left-handed Metamaterial," *Applied Physics Letters*, 78(4): 489-491 (January 2001).

[13] Shelby, R. A. D. R. Smith, and S. Schultz. "Experimental Verification of a Negative Index of Refraction," *Science*, 292(5514): 77-79 (April 2001).

[14] Hand, T. H., and S. A. Cummer, "Frequency Tunable Electromagnetic Metamaterial Using Ferroelectric Loaded Split Rings," *Journal of Applied Physics*, 103(066105): 1-3 (March 2008).

[15] Khan M. F. and M. J. Mughal. "Tunable Metamaterials by Varying the Inductance and Capacitance of S-shaped Resonator," *IEEE 2009 Int. Symp. on Microwave, Antenna, Propagation and EMC Technologies for Wireless Communications*, pp 140-143 (December 2009).

[16] Jin P. and R. W. Ziolkowski, "Broadband, Efficient, Electrically Small Metamaterial-inspired Antennas Facilitated by Active Near-field Resonant Parasitic Elements," *IEEE Transactions on Antennas and Propagation*, 58(2): 318-327 (February 2010).

[17] Ramo, S., J. R. Whinnery, T. Van Duzer, *Fields and Waves in Communication Electronics*. New York: John Wiley & Sons, 1984.

[18] Hayt, Jr., W. H., J. A. Buck, *Engineering Electromagnetics Sixth Edition*. New York: McGraw-Hill, 2001.

[19] Ward, A. J., and J. B. Pendry. "Refraction and Geometry in Maxwell's Equations," *Journal of Modern Optics*, 43(4): 773-793 (April 1996).

[20] Pendry, J. B., D. Schurig, and D. R. Smith. "Controlling Electromagnetic Fields," *Science*, 312(5781): 1780-1782 (June 2006).

[21] McGurik, J. S. *Electromagnetic Field Control and Optimization Using Metamaterials*, PhD Dissertation, AFIT/DEE/ENG/09-13. School of Engineering, Air Force Institute of Technology (AU), Wright-Patterson AFB OH, December 2009.

[22] Ramakrishna S. A., and J. B. Pendry. "Removal of Absorption and Increase in Resolution in a Near-field Lens via Optical Gain," *Physical Review B*, 67(201101(R)): 1-4 (May 2003).

[23] Podolskiy, V. A., L. V. Alekseyev and E. E. Narimanov. "Strongly Anisotropic Media: the THz Perspectives of Left-handed Materials," Journal of Modern Optics, 52(16): 2343-2349 (November 2005).

المنارة للاستشارات

www.manaraa.com

[24] Linden, S., C. Enkrich, M. Wegener, J. Zhou, T. Koschny, C. M. Soukoulis. "Magnetic Response of Metamaterials at 100 Terahertz," *Science*, 306: 1351-1353 (November 2004).

[25] Pendry, J. B., A. J. Holden, W. J. Stewart and I. Youngs. "Extremely Low Frequency Plasmons in Metallic Mesostructures," *Physical Review Letters*, 76(25): 4773-4776 (June 1996).

[26] Ruehli, E. A. "Inductance Calculations in a Complex Integrated Circuit Environment," *IBM Journal Research and Development*, 16(5): 470-481 (September 1972).

[27] CoventorWare Website: www.coventor.com/coventorware.html

[28] Kamon M., F. Wang and J. White. "Recent Improvements to Fast Inductance Extraction and Simulation," *Proc. of the 7th Topical Meeting on Electrical Performance of Electronic Packaging*, pp. 281-284 (October 1998).

[29] Leus, V. and D. Elata, "Fringing Field Effect on Electrostatic Actuators," *Technical Report ETR-2004-2*: 1-15 (May 2004).

[30] Osterberg, P. M. and S. D. Senturia, "M-test: A Test Chip for MEMS Material Property Measurement Using Electrostatically Actuated Test Structures," *IEEE Journal of Microelectromechanical Systems*, 6(2): 107-118 (June 1997).

[31] Coutu, Jr, R. A. *Electrostatic Radio Frequency (RF) Microelectromechanical Systems (MEMS) Switches with Metal Alloy Electric Contacts*, PhD Dissertation, AFIT/DS/ENG/04-05. School of Engineering and Management, Air Force Institute of Technology (AU), Wright-Patterson AFB OH, September 2004.

[32] Engheta, N., A. Salandrino and A. Alù, "Circuit Elements at Optical Frequencies: Nanoinductors, Nanocapacitors, and Nanoresistors," *Physical Review Letters*, 95(095504): 1-4 (August 2005).

[33] Engheta, N., "Circuits with Light at Nanoscales: Optical Nanocircuits Inspired by Metamaterials," *Science*, 317: 1698-1702 (September 2007).

[34] Alù, A., A. Salandrino and N. Engheta, "Parallel, Series, and Intermediate Interconnections of Optical Nanocircuits Elements. 2. Nanocircuit and Physical Interpretation," *Journal of Optical Society of America B*, 24(12): 3014-3022 (December 2007).

[35] Staffaroni, M., J. Conway, S. Vedantam, J. Tang and E. Yablonovitch. "Circuit Analysis in Metal-optics," Photonics and Nanostructures – Fundamentals and Applications, 10(1): 166-176 (January 2012).

المنارة للاستشارات

www.manaraa.com

[36] Smith, D. R., S. Schultz, P. Markos and C. M. Soukoulis. "Determination of Effective Permittivity and Permeability of Metamaterials from Reflection and Transmission Coefficients," *Physical Review B*, 64(195104): 1-5 (April 2002).

[37] Chen, X., T. M. Grzegorczyk, B. Wu, J. Pacheco and J. A. Kong. "Robust Method to Retrieve the Constitutive Effective Parameters of Metamaterials," *Physical Review Letters E*, 70(016608): 1-7 (July 2004).

[38] Yuan, Y., B-I, Popa and S. A. Cummer. "Zero Loss Magnetic Metamaterials Using Powered Active Unit Cells," *Optics Express*, 17(18): 16135-16143 (August 2009).

[39] Xiao, S., V. P. Drachev, A. V. Kildishev, X. Ni, U. K. Chettiar, H-K. Yuan and V. M. Shalaev. "Loss-free and Active Optical Negative-index Metamaterials," *Nature*, 466: 735-740 (August 2010).

[40] Casares-Miranda, F. P., C. Camacho-Peñalosa, and C. Caloz. "High-gain Active Composite Right/Left-Handed Leaky-Wave Antenna," *IEEE Transactions on Antennas and Propagation*, 54(8): 2292-2300 (August 2006).

[41] Popov, A. K. and V. M. Shalaev. "Compensating Losses in Negative-index Metamaterials by Optical Parametric Amplification," *Optics Letters*, 31(14): 2169-2171 (July 2006).

[42] Jiang, T., K. Chang, L-M. Si, L. Ran and H. Xin. "Active Microwave Negative-index Metamaterial Transmission Line with Gain," *Physical Review Letters*, 107(205503): 1-5 (November 2011).

[43] Kozyrev, A. B., H. Kim and D. W. van der Weide. "Parametric Amplification in Left-handed Transmission Line Media," *Applied Physics Letters*, 88(264101): 1-3 (June 2006).

[44] Liu, C. *Foundations of MEMS*. New Jersey: Pearson Education, Inc., 2006.

[45] Field, L. A. and R. S. Muller. "Fusing Silicon Wafers with Low Melting Temperature Glass," *Sensors and Actuators A: Physical*, 23(1-3): 27- 33 (April 1990).

[46] Madou M. *Fundamentals of microfabrication*, New York: CRC Press, 1997.

[47] Matsuzuka, N., Y. Hirai and O. Tabata. "A Novel Fabrication Process of 3D Microstructures by Double Exposure in Deep X-ray Lithography (D^2XRL)," *Journal of Micromechanics and Microengineering*, 15: 2056-2062 (September 2005).

[48] Jaeger, R. C., *Introduction to Microelectronic Fabrication Volume V*, New Jersey :Prentice Hall, 2002.

المنارة للاستشارات

www.manaraa.com

[49] polyMUMPS ® Process Website: http://www.memscap.com/en_mumps.html

[50] SUMMiT V ™ Overview, Sandia National Laboratories Website: www.mems.sandia.gov/tech-info/summit-v.html

[51] Mink, S. S. *Microelectromechanical Systems (MEMS) Interrupter for Safe and Arm Devices*, MS thesis, AFIT/GE/ENG/06-43. School of Engineering, Air Force Institute of Technology (AU), Wright-Patterson AFB OH, March 2006 (ADA451337).

[52] Platteborze, R. C. *Microelectromechanical Systems (MEMS) Safe and Arm Barrier for Low-energy Exploding Foil Initiators (LEEFI)*, MS thesis, AFIT/GEO/ENP/08-01. School of Engineering, Air Force Institute of Technology (AU), Wright-Patterson AFB OH, March 2008 .

[53] Que, L, P. Jae-Sung and Y.B. Gianchandani. "Bent-beam Electrothermal Actuators – Part I: Single Beam and Cascaded Devices," *Journal of Microelectromechanical Systems*, 10(2): 247-254 (June 2001).

[54] Sinclair, M. J. "A High Force Low Area MEMS Thermal Actuator," *2000 Inter Society Conference on Thermal Phenomena*, pp. 127-132 (May 2000).

[55] Kolesar, E. S., M. D. Ruff, W. E. Odom, J. A. Jayachadran, J. B. McAllister, S. Y. Ko, J. T. Howard, P. B. Allen, J. M. Wilken, N. C. Boydston, J. E. Bosch and R. J. Wilks. "Single- and Double-hot Arm Asymmetrical Polysilicon Surface Micromachined Electrothermal Microactuators Applied to Realize a Microengine," *Thin Solid Films*, 420-421: 530-538 (December 2002).

[56] Soukoulis, C. M., S. Linden and M. Wegener, "Negative Refractive Index at Optical Wavelengths," *Science*, 315(5808): 43-49 (January 2007).

[57] Rederus, L. A. *A MEMS Multi-cantilever Variable Capacitor on Metamaterial*, MS thesis, AFIT/GE/ENG/09-35. School of Engineering and Management, Air Force Institute of Technology (AU), Wright-Patterson AFB OH, March 2009 (ADA497157).

[58] Moore, E. A., D. Langley, M. E. Jussaume, L. A. Rederus, C. A. Lundell, R. A. Coutu Jr., P. J. Collins, L. A. Starman. "SRRs Embedded with MEMS Cantilevers to Enable Electrostatic Tuning of the Resonant Frequency," *Experimental Mechanics*, DOI: 10.1007/s11340-011-9498-8: 1-9 (April 2011).

[59] Coutu, R. A., P. J. Collins, E. A. Moore, D. Langley, M. E. Jussaume and L. A. Starman. "Electrostatically Tunable Meta-atoms Integrated with In-situ Fabricated MEMS Cantilever Beam Arrays," *IEEE/ASME Journal of Microelectromechanical Systems*, 99: 1-6 (October 2011).

المنارة للاستشارات
www.manaraa.com

[60] Langley, D, R. A. Coutu, S. A. LaVern and P. J.Collins. “MEMS Integrated Metamaterial Structure Having Variable Resonance for RF Applications,” *Proceedings of the 2010 SEM Annual Conference and Exposition on Experimental and Applied Mechanics*, 313: 1-6 (June 2010).

[61] Langley, D., E. A. Moore, R. A. Coutu, Jr., P. J. Collins. “MEMS Integrated Metamaterials with Variable Resonance Operating at RF Frequencies,” *Proceedings of the 2011 SEM Annual Conference and Exposition on Experimental and Applied Mechanics*, 328: 1-8 (June 2011).

[62] “0.5 – 6 GHz Low Noise GaAs MMIC Amplifier,” *Avago Technologies Datasheet AV02-2514EN* (2010).

[63] Advanced Circuits website: http://www.4pcb.com

[64] CoventorWare ® Website: www.coventor.com/coventorware.html.

[65] Grover F. W. *Inductance Calculations, Working Formula and Tables*, New York: Dover Publications, 1946.

[66] CST Microwave Studio® Website: www.cst.com/Content/Products/MWS/Overview.aspx

[67] Jussaume, M. E. *Electromagnetic Modeling and Measurement of Adaptive Metamaterial Sturctural Elements*, MS thesis, AFIT/GE/ENG/11-20. School of Engineering and Management, Air Force Institute of Technology (AU), Wright-Patterson AFB OH, March 2011 (ADA540076).

[68] Qamhieh, N., H. Ghamlouche, S. T. Mahmoud, H. Al-Shamisi and S. Ahmad. “DC and AC Conductivity Measurements on Ge2Sb2Te5 Films,” *Journal of Ovonic Research*, 3(2): 51-55 (June 2007).

[69] Morales-Sanchez, E., J. Gonzales-Hernandez and E. Prokhorov. “Glassy Transformation and Structural Change in $Ge_2Sb_2Te_5$ Studied by Impedance Measurements,” *Journal of Optoelectronics and Advanced Materials*, 3(2): 333-336 (June 2001).

[70] Kozyukhin, S. A., A. A. Sherchenkov, E. V. Gorshkova, V. Kh. Kudoyarova, A. I. and Vargunin. “Structural Transformations in Thin Ge2Sb2Te5 Films,” *Inorganic Materials*, 45(4): 361-365 (2009).

[71] Hopkins, E. J., G. D. Hopkins and C. D. Bailey. “Mechanism of Apparent Gain Observed in Focused Beam Measurements of a Planar FSS,” *2010 IEEE International Symposium on Antennas and Propagation and CNC-USNC/URSI Radio Science Meeting - Leading the Wave*, pp.1-4 (July 2010).

المنارة للاستشارات
www.manaraa.com

[72] Langley, D., R. A. Coutu, Jr. L. A. Starman, and M. A. Marciniak. “Investigation into Metamaterial Structures Operating at Terahertz Wavelength,” *Proceedings of SPIE*, 7592: 75920X (January 2010)

[73] Moore, E. A., D. Langley and R. A. Coutu, Jr. “Terahertz Metamaterial Structures Fabricated by polyMUMPS,” *Proceedings of the 2011 SEM Annual Conference and Exposition on Experimental and Applied Mechanics*, 284: 1-6 (June 2011).

[74] Shen, N., M. Kafesaki, T. Koschny, L. Zhang, E. N. Economou and C. M. Soukoulis. “Broadband Blueshift Tunable Metamaterials and Dual-band Switches,” *Physical Review B* 779(161102): 1-4 (April 2009).

[75] Chiam, S., R. Singh, W. Zhang and A. A. Bettiol, “Controlling Metamaterial Resonances via Dielectric and Aspect Ratio Effects,” *Applied Physics Letters* 97(191906): 1-3 (November 2010).

[76] Chen, H-T., J. F. O’Hara, A. J. Taylor and R. D. Averitt, “Complementary Planar Terahertz Metamaterials,” *Optics Express* 15(3): 1084-1095 (February 2007).

[77] Peralta, X. G., E. I. Smirnova, A. K. Azad, H-T. Chen, A. J. Taylor, I. Brener and J. F. O’Hara, “Metamaterials for THz Polarimetric Devices,” *Optics Express* 17(2): 773-783, (January 2009).

[78] Azad, A.K., J. Dai and W. L. Zhang. “Transmission Properties of Terahertz Pulses Through Subwavelength Double Split Ring Resonators,” *Optics Letters* 31(5): 634-636 (March 2006).

[79] Yen, T. J., W. J. Padilla, N. Fang, D. C. Vier, D. R. Smith, J. B. Pendry, D. N. Basov and X. Zhnag. “Terahertz Magnetic Response from Artificial Materials,” *Science* 303(5663): 1494-1496 (March 2004).

[80] Driscoll, T., G.O. Andreev, D.N. Basov, S.Palit, T. Ren, J. Mock, S.Y. Cho N.M. Jockerst and D.R. Smith. “Quantiative Investigation of a Terzhertz Artificial Magnetic Resonance Using Oblique Angle Spectroscopy.” *Applied Physics Letters* 90(092508): 1-3 (February 2007).

[81] Han, J., A. Lakhtakia and C-W. Qui. “Terahertz Metamaterials with Semiconductor Split-ring Resonators for Magnetic Tunability,” *Optics Express* 16(19): 14390-14396 (September 2008).

[82] Azad, A. K., H.T. Chen, X. Lu, J. Gu, N.R. Weisse-Bernstein, E. Akhodov, A. Taylor, W. Zhang and J.F. O’Hara, “Flexible Quasi-three-dimensional Terahertz Electric Metamaterials,” *Terahertz Science and Technology* 2(1): 15-22, (March 2009).

المنارة للاستشارات

www.manaraa.com

[83] Langley, D., R. A. Coutu, Jr., L. A. Starman and S. Rogers. "Optical Metamaterials for Photonic Applications," *Proceedings of SPIE*, 7468: 74680H (August 2009).

[84] Chettiar, U. K., A. V. Kildishev, H. –K. Yuan, W. Cai, S. Xiao, V. P. Drachev and V. M. Shalaev. "Dual-band Negative Index Metamaterial: Double-negative at 813 nm and Single-negative at 772 nm," *Optics Letters*, 32(12): 1671-1673 (2007).

[85] Hecht, E. *Optics* (4th Edition), San Francisco: Pearson Addison Wesley, 2002.

[86] Schaffer, J. P., A. Saxena, S. D. Antolovich, T. H. Sanders Jr., S. B. Warner. *The Science and Design of Engineering Materials*, Chicago: Irwin, 1995.

[87] Kaine-Krolak, M. and M. E. Novak. "An Introduction to Infrared Technology: Applications in the Home, Classroom, Workplace, and Beyond …," *Closing the Gap Conference*, pp. 1-16 (October 1995).

[88] "Plunkett's Telecommunications Industry Almanac 2011," Plunkett Research®, Limited, *Telecommunications Industry Overview* Website: www.plunkettresearch.com/telecommunications%20market%20research/industry%20statistics

[89] *How Night Vision Works*, American Technologies Network Corporation Website: www.atncorp.com/HowNightVisionWorks

[90] Soukoulis, C. M., M. Kafesaki and E. N. Economou. "Negative-index Materials: New Frontiers in Optics," *Advanced Materials*, 18(15): 1941-1952 (August 2006).

[91] Sze, S. M. and K. K. Ng, *Physics of Semiconductor Devices*, New Jersey: John Wiley & Sons, Inc Publications, 2007.

[92] Brueck, S. R. J., S. H. Zaidi, X. Chen and Z. Zhang. "Interferometric Lithography – From Periodic Arrays to Arbitrary Patterns," *Microelectronic Engineering*, 41/41, 145-148 (1998).

[93] Familia, A. M. and A. Sarangan. "Threshold Gain Analysis of Second Order Distributed Feedback Lasers Based on [2-methoxy-5-(2'-ethylhexyloxy)-1, 4-phenylenevinylene]," *Optics Communications*, 281, 310-318 (2008).

[94] *Complete Angle Scatter Instrument* (084-714-010). Portland: Schmitt Measurement Systems, Inc., 2010.

[95] *SeeSPOT III+*. Pamphlet. Wilsonville: FLIR Systems, Inc. [2006].

المنارة للاستشارات
www.manaraa.com

Vita

Captain Derrick Langley enlisted in the U. S. Air Force in 1987. He was accepted into the Professional Officer Course, Air Force Reserve Officer Training Corps, in 2002, and attended the University of Central Florida, Orlando. In 2003, he graduated with a Bachelor of Science degree in Electrical Engineering and a specialization in Microelectronics. After earning his commission, Captain Langley was assigned as a Electronic Device Engineer to the Sensors Directorate, Air Force Research Laboratory to develop wideband gap semiconductor devices for military applications. In 2008, he was assigned to the Air Force Institute of Technology to pursue a Doctor of Philosophy degree in Electrical Engineering with a focus on Microelectromechanical Systems. Upon graduation, Captain Langley will be assigned to the Department of Electrical and Computer Engineering at the Air Force Institute of Technology.

للاستشارات المنارة

www.manaraa.com

REPORT DOCUMENTATION PAGE			*Form Approved* *OMB No. 074-0188*

The public reporting burden for this collection of information is estimated to average 1 hour per response, including the time for reviewing instructions, searching existing data sources, gathering and maintaining the data needed, and completing and reviewing the collection of information. Send comments regarding this burden estimate or any other aspect of the collection of information, including suggestions for reducing this burden to Department of Defense, Washington Headquarters Services, Directorate for Information Operations and Reports (0704-0188), 1215 Jefferson Davis Highway, Suite 1204, Arlington, VA 22202-4302. Respondents should be aware that notwithstanding any other provision of law, no person shall be subject to an penalty for failing to comply with a collection of information if it does not display a currently valid OMB control number.
PLEASE DO NOT RETURN YOUR FORM TO THE ABOVE ADDRESS.

1. REPORT DATE *(DD-MM-YYYY)*	**2. REPORT TYPE**	**3. DATES COVERED** *(From – To)*
14-06-2012	Dissertation	16-08-2008 – 14-06-2012

4. TITLE AND SUBTITLE	**5a. CONTRACT NUMBER**
Design, Fabrication and Testing of Tunable RF Meta-atoms	**5b. GRANT NUMBER**
	5c. PROGRAM ELEMENT NUMBER
6. AUTHOR(S)	**5d. PROJECT NUMBER** 11G260
Langley, Derrick, Captain, USAF	**5e. TASK NUMBER**
	5f. WORK UNIT NUMBER

7. PERFORMING ORGANIZATION NAMES(S) AND ADDRESS(S)	**8. PERFORMING ORGANIZATION REPORT NUMBER**
Air Force Institute of Technology Graduate School of Engineering and Management (AFIT/EN) 2950 Hobson Way Wright-Patterson AFB OH 45433-7765	AFIT/DEE/ENG/12-04
9. SPONSORING/MONITORING AGENCY NAME(S) AND ADDRESS(ES)	**10. SPONSOR/MONITOR'S ACRONYM(S)** AFRL/RXBN AFRL/RXPJ
Air Force Research Laboratory, Materials Directorate Attn: Dr. Katie E. Thorp and Dr. Augustine M. Urbas 2941 Hobson Way Wright-Patterson AFB Ohio 45433 (937) 255-9145 (DSN: 785-9145) Katie.Thorp@wpafb.af.mil, (937) 255-9713 (DSN: 785-9713) Augustine.Urbas@wpafb.af.mil	**11. SPONSOR/MONITOR'S REPORT NUMBER(S)**

12. DISTRIBUTION/AVAILABILITY STATEMENT
APPROVED FOR PUBLIC RELEASE; DISTRIBUTION UNLIMITED.

13. SUPPLEMENTARY NOTES
This material is declared a work of the U.S. Government and is not subject to copyright protection in the United States

14. ABSTRACT
Metamaterials are engineered structures designed to alter the propagation of electromagnetic waves incident upon the structure. The focus of this research was the effect of metamaterials on electromagnetic signals at radio frequencies. RF meta-atoms were investigated to further develop the theory, modeling, design and fabrication of metamaterials. Comparing the analytic modeling and experimental testing, the results provide a deeper understanding into metamaterials which could lead to applications for beam steering, invisibility cloaking, negative refraction, super lenses, and hyper lenses. RF meta-atoms integrated with microelectromechanical systems produce tunable meta-atoms in the 10 – 15 GHz and 1 – 4 GHz frequency ranges. RF meta-atoms with structural design changes are developed to show how inductance changes based on structural modifications. RF meta-atoms integrated with gain medium are investigated showing that loss due to material characteristics can be compensated using active elements such as a Low Noise Amplifier. Integrating the amplifier into the split ring resonator causes a deeper null at the resonant frequency.

The research results show that the resonant frequency can be tuned using microelectromechanical systems, or by induction with structural designs and reduce loss associated with the material conductivity by compensating with an active gain medium. Proposals that offer future research activities are discussed for inductance and active element meta-atoms. In addition, terahertz (THz), infrared (IR), and optical structures are briefly investigated.

15. SUBJECT TERMS
Capacitance, Index of Refraction, Inductance, MEMS, Meta-atom, Metamaterials, Permeability, Permittivity, Split-ring Resonator

16. SECURITY CLASSIFICATION OF:			**17. LIMITATION OF ABSTRACT**	**18. NUMBER OF PAGES**	**19a. NAME OF RESPONSIBLE PERSON** Dr. Ronald A. Coutu Jr. (ENG)
REPORT	**ABSTRACT**	**c. THIS PAGE**			**19b. TELEPHONE NUMBER** *(Include area code)*
U	U	U	UU	198	(937) 255-3636 x7230 Ronald.Coutu@afit.edu

المنارة للاستشارات
www.manaraa.com